

This is to certify that the  
dissertation entitled  
The Effect of Substrate Bias  
on Sputtered Hydrogenated  
Amorphous Silicon  
presented by  
Nicol McGruer

has been accepted towards fulfillment  
of the requirements for  
Ph.D. degree in Electrical Engineering

Donnie K Reinhard  
Major professor

Date August 24, 1983



3 1293 00994 7312



RETURNING MATERIALS:  
Place in book drop to  
remove this checkout from  
your record. FINES will  
be charged if book is  
returned after the date  
stamped below.

JUL 8 1999 2

DO NOT RECALL

NO FINE CHARGE

THE EFFECT OF SUBSTRATE BIAS  
ON SPUTTERED HYROGENATED  
AMORPHOUS SILICON

By

Nicol McGruer

A DISSERTATION

Submitted to  
Michigan State University  
in partial fulfillment of the requirements  
for the degree of

DOCTOR OF PHILOSOPHY

Department of Electrical Engineering  
and Systems Science

1983

## ABSTRACT

### THE EFFECT OF SUBSTRATE BIAS ON SPUTTERED HYDROGENATED AMORPHOUS SILICON

By

Nicol McGruer

This dissertation describes an investigation of the effects of substrate bias on sputtered amorphous silicon. To a lesser extent, the effects of target voltage on the properties of the semiconductor film and the properties of Schottky barrier devices are also reported. Significant results include the identification of a mechanism by which bias sputtering degrades the film properties at high substrate bias and the observation that bombardment controlled by the target voltage is significant and can mask substrate bias effects.

Increasing substrate bias is seen to result in an increased conductivity activation energy and a decreased photoconductivity. The effect is strongest for samples sputtered at a low target voltage, where an increase in substrate bias from 31 to 106 volts results in a decrease in the photoconductivity by a factor of 1,000.

The electrical conductivity is modeled as

$$\sigma = \sigma_0 e^{-(E_c - E_F)/kT} + \sigma_h e^{-(E_T - E_F + W)/kT}.$$

The first term represents extended state conduction above the mobility edge at  $E_c$ , where  $\sigma_0$  is  $2000 (\Omega\text{-cm})^{-1}$ . The second term represents hopping among gap states at energy  $E_T$ , 0.38 eV below the mobility edge. The density of states at  $E_T$  is enhanced by overly energetic substrate bombardment.  $W$  is the activation energy of the hopping mobility and  $E_F$  is the Fermi energy. The optical properties of the amorphous silicon films do not change appreciably over the whole range of substrate biases, indicating that no gross changes in either the density of states in the gap or in structural properties affecting the index of refraction occur due to the increased level of bombardment.

Schottky barrier properties as a function of intrinsic layer thickness, along with measurements of the conversion efficiency suggest that recombination of carrier in the space charge layer and the limited diffusion length of minority carriers limit photovoltaic performance. The dark characteristics yield rectification ratios of up to  $8 \times 10^7$ . At forward biases of greater than  $\sim 0.5V$ , the bulk resistance of the intrinsic layer decreases due to injection effects from the back contact.

## ACKNOWLEDGMENTS

The author is grateful to his major professor, Donnie K. Reinhard, for guidance and encouragement through his entire graduate program. In addition thanks are due to other members of the guidance committee, Drs. D. P. Nyquist, S. A. Solin, J. Asmussen, J. Freeman, and B. Ho for their time and interest in this research.

This work was supported in part by fellowships from the General Telephone & Electronics Corporation and the Michigan State University Graduate Office and by the National Science Foundation Grant ENG 79-10896.

## TABLE OF CONTENTS

List of Figures . . . . .	v
I. INTRODUCTION . . . . .	1
II. BACKGROUND . . . . .	5
2.1 Hydrogenated Amorphous Silicon . . . . .	5
2.2 Bias Sputtering. . . . .	9
2.3 Sputtered Amorphous Silicon. . . . .	16
2.4 Schottky Barriers. . . . .	17
III. EXPERIMENTAL METHODS . . . . .	19
3.1 Introduction . . . . .	19
3.2 Film Deposition. . . . .	20
3.2.1 Deposition Systems . . . . .	20
3.2.2 System Purity. . . . .	27
3.2.3 Bias Sputtering. . . . .	32
3.2.4 Film Deposition. . . . .	41
3.3 Measurements . . . . .	43
3.3.1 Optical Measurements . . . . .	43
3.3.2 Index of Refraction and Thickness Measurement. . . . .	47
3.3.3 Optical Absorption Coefficient and Optical Energy Gap . . . . .	51
3.3.4 Gold Transmission Measurement. . . . .	58
3.3.5 Hydrogen Content . . . . .	59
3.3.6 Conductivity vs Temperature. . . . .	62
3.3.7 Photoconductivity, $\mu\tau$ Product. . . . .	66
3.3.8 Schottky Barrier Characteri- zation . . . . .	71
IV. MATERIAL PROPERTIES: SUBSTRATE BIAS EFFECTS	76
4.1 Introduction . . . . .	76
4.2 Preliminary Work and Results . . . . .	77
4.2.1 Initial Material Evaluation and Device Layout Testing. . . . .	77
4.2.2 Effects of Aluminum Contami- nation . . . . .	91
4.3 Substrate Bias Results . . . . .	92
4.3.1 Introduction . . . . .	92
4.3.2 Index of Refraction. . . . .	93
4.3.3 Optical Energy Gap . . . . .	94

4.3.4	Dark Conductivity as a Function of Temperature . . . . .	100
4.3.5	Photoconductivity: $\mu\tau$ product . . . . .	109
4.4	Discussion of Results. . . . .	113
4.4.1	Optical Measurements . . . . .	113
4.4.2	Electrical Measurements. . . . .	121
4.4.3	Comparison with Other Bias Results. . . . .	131
4.5	Conclusions. . . . .	135
V.	SCHOTTKY BARRIER RESULTS . . . . .	138
5.1	Introduction . . . . .	138
5.2	Substrate Bias for Schottky Barrier Diodes. . . . .	139
5.3	Schottky Barrier Data. . . . .	140
5.4	Device Photovoltaic Properties . . . . .	146
5.5	Dark I-V Characteristics . . . . .	153
5.6	Conclusions. . . . .	163
VI.	SUMMARY, CONCLUSIONS AND RECOMMENDATIONS . . . . .	166
APPENDIX A	DETAILS OF FILM DEPOSITION. . . . .	172
APPENDIX B	MEASUREMENT OF INDEX OF REFRACTION AND THICKNESS . . . . .	175
APPENDIX C	DETERMINATION OF THE OPTICAL ABSORPTION COEFFICIENT. . . . .	189
APPENDIX D	GOLD TRANSMISSION MEASUREMENTS. . . . .	199
	LIST OF REFERENCES. . . . .	204

## LIST OF FIGURES

2.1	Target voltage and current. . . . .	13
2.2(a)	rf diode sputtering . . . . .	15
2.2(b)	rf bias sputtering. . . . .	15
3.1	Sputtering system schematic . . . . .	22
3.2	Sputtering system electrical schematic. . .	23
3.3	Target voltages . . . . .	33
3.4(a)	Coplanar device structure . . . . .	44
3.4(b)	Schottky barrier structure. . . . .	44
3.5	Optical measurement schematics. . . . .	45
3.6	R,T and R/1-R vs wavelength (ND-7). . . . .	52
3.7	Optical absorption coefficient. . . . .	53
3.8	Optical energy gap for a crystalline semiconductor (a) Density of states (b) $(\alpha\hbar\omega)^{\frac{1}{2}}$ vs $\hbar\omega$ . . . . .	56
3.9	Optical energy gap for an amorphous semiconductor (a) Density of states (b) $(\alpha\hbar\omega)^{\frac{1}{2}}$ vs $\hbar\omega$ . . . . .	57
3.10	Hydrogen content vs depth . . . . .	61
3.11	Conductivity vs $10^3/T$ (ND-61) . . . . .	65
3.12	Photoconductivity measurement . . . . .	69
3.13	ND-11 Dark I-V characteristics. . . . .	72
3.14	Light I-V characteristics . . . . .	75
4.1	Thickness of bias sputtered Mo. . . . .	79
4.2	Non-uniform sputtering. . . . .	80

4.3	ND-6 and ND-7 I-V characteristics . . . . .	83
4.4	I-V characteristics showing improvement with an n <sup>+</sup> contact layer. . . . .	84
4.5	Original device layout. . . . .	86
4.6	n <sup>+</sup> -undoped-n <sup>+</sup> characteristics . . . . .	88
4.7	Curvature in 10 <sup>3</sup> /T for n <sup>+</sup> -undoped-n <sup>+</sup> sample	90
4.8	Measured index fit to Wemple-Di Donenico equation. . . . .	95
4.9	Deviation from fit vs bias. . . . .	95
4.10	E <sub>og</sub> vs bias . . . . .	97
4.11	(αħω) <sup>1/2</sup> vs ħω. . . . .	98
4.12	Optical absorption coefficient. . . . .	99
4.13	Conduction paths. . . . .	101
4.14	σ <sub>o</sub> vs bias. . . . .	104
4.15	E <sub>A</sub> vs bias. . . . .	105
4.16	Log σ vs 10 <sup>3</sup> /T for high and low substrate bias samples. . . . .	107
4.17	σ <sub>o</sub> vs E <sub>A</sub> , high substrate bias points indicated . . . . .	108
4.18	Photoconductivity vs substrate bias . . . . .	114
4.19	Photoconductivity vs E <sub>A</sub> , high bias points indicated . . . . .	115
4.20	Photoconductivity vs intensity. . . . .	116
4.21	Decrease in photoconductivity with light soaking in 200 mW/cm <sup>2</sup> , 650 nm light . . . . .	117
4.22	Annealing of light soaked sample ND-80. . . . .	118
4.23	Model fit for high and low substrate bias samples . . . . .	127

4.24	Band diagram for 2 conductivity paths (ND-67) . . . . .	128
4.25	Photoconductivity vs substrate bias. MSU and U. of Sheffield results . . . . .	133
5.1	Summary of Schottky barrier properties. . .	141
5.2	Barrier height: diffusion theory, thermionic emission theory. . . . .	144
5.3	Photovoltaic performance comparison . . . .	149
5.4	Band diagram derived from typical measure- ments of barrier height and bulk properties	150
5.5	I-V characteristics of 3 devices with different intrinsic layer thicknesses . . .	155
5.6	Bulk J-V characteristics. . . . .	156
5.7	Reverse characteristics, $\text{Log } J \text{ vs } V^{\frac{1}{2}}$ . . . .	161
5.8	J-V plots for ND-84 and ideal with the same saturation current . . . . .	162
B 1(a)	Monochrometer output vs wavelength. . . . .	177
B 1(b)	Optical sample. . . . .	177
B 2	R vs $\delta$ and incident light intensity vs $\delta$ . .	179
B 3	Back reflection diagram . . . . .	185
C 1	$\alpha$ measurement sample. . . . .	190
C 2	Functions for computing error in $\alpha$ . . . . .	195
C 3	Real and simple $O(\lambda)$ . . . . .	196
D 1	Gold transmission schematic . . . . .	200
D 2	Gold reflectance and transmittance. . . . .	202

## CHAPTER I

### INTRODUCTION

Interest in producing high quality hydrogenated amorphous silicon films has increased considerably over the last several years. This interest stems in large part from the probable utility of the material in applications such as photovoltaics,<sup>1,2</sup> drivers and controllers for large display arrays,<sup>3</sup> inexpensive moderate performance devices,<sup>4</sup> fast photodetectors,<sup>5,6</sup> and imaging devices.<sup>7,8</sup> Currently, low cost, moderate efficiency photovoltaics are by far the most widely investigated of the above.

Hydrogenated amorphous silicon typically contains 5-20 at.% hydrogen, which passivates dangling bonds, giving the silicon-hydrogen alloy an exceptionally low density of states in the gap for an amorphous material. As a consequence the alloy exhibits several desirable properties not usually associated with amorphous semiconductors including high photoconductivity, high dark resistivity and sensitivity to p and n type dopants. Schottky barriers, p-n junctions and field effect transistors may be constructed.

Amorphous silicon based solar cells may be

considerably less expensive than conventional crystalline cells for several reasons: the deposition process is relatively simple, the active layer of the cell is quite thin, typically 1 micron as compared to 250 microns for crystalline materials, and several of the proposed deposition processes used are well known and suitable for large area production. Although the efficiency of amorphous solar cells is not expected to approach that of the best crystalline devices, a number of groups have tested devices which show conversion efficiencies of 7-10% under AM-1 conditions.<sup>9,10,11</sup> The theoretical maximum solar cell efficiency for a semiconductor with the bandgap of amorphous silicon ( $\sim 1.7\text{eV}$ ) is 23%, leaving, in principle, considerable room for improvement as better material is made.<sup>104</sup> For primarily economic reasons 10% is considered a threshold efficiency for power generation system practicality. Amorphous silicon research is motivated by the nearness of this goal and the good potential of the material. Amorphous silicon field effect transistors are attractive in that they may be fabricated at relatively low temperatures over large areas on a wide variety of substrates.

It is well known that the properties of amorphous silicon films depend strongly on the deposition process as well as on various parameters specific to each

process.<sup>12,13</sup> A major hypothesis of this research is that certain plasma-film interactions are important in determining the properties of the deposited film. This thesis investigates a technique, rf bias sputtering, which modifies the plasma-film interaction via a variable substrate bias. The resultant effects on electrical and optical properties are investigated with regard to their effect on device performance. The principal contribution of this research is the identification of bombardment effects as important in controlling the properties of sputtered amorphous silicon. A sensitivity of the electrical properties to substrate bias is reported, which is masked under certain circumstances by substrate bombardment controlled by the target voltage. Thus the target voltage is also seen to affect the substrate bombardment and thereby the film properties. Schottky barrier diodes are used as another tool to investigate the properties of the material as well as to very directly evaluate its suitability for device applications.

Chapter II outlines the present understanding of the properties of amorphous silicon films as well as the deposition techniques used to produce these films with special emphasis on the technique of rf sputtering. Brief overviews of bias sputtering theory and Schottky barriers on amorphous silicon are given. In Chapter III the fabrication technique of rf bias sputtering used to

produce the films and the measurement techniques used to characterize the films are detailed. Chapter IV presents preliminary work on device structures and system purity as well as the bulk of the bias results. The results are discussed in terms of the theory and models explaining the observed behavior are presented. Chapter V reports the characteristics of Schottky barriers produced during the course of the research. Again the results are interpreted in terms of the theory and conclusions are drawn regarding the quality of our material. Finally, Chapter VI summarizes the results and suggests areas for further research.

## CHAPTER II

### BACKGROUND

#### 2.1 Hydrogenated Amorphous Silicon

Research interest in amorphous semiconductors, particularly in amorphous silicon, has increased rapidly since the report of wide-ranging control of the electronic properties of amorphous silicon by Spear and LeComber in 1975.<sup>14</sup> In addition, the theoretical understanding of non-crystalline materials has advanced considerably, although the correspondence between theory and experiment is not as close as it is for crystalline semiconductors. In fact Mott and Anderson shared the 1977 Nobel prize in physics in part for their theoretical investigations of the electronic structure in disordered solids.

Expanding on the work of Chittick, Alexander and Sterling,<sup>16</sup> Spear and LeComber demonstrated in 1975 the high sensitivity to doping of amorphous silicon produced by the glow discharge decomposition of silane as compared to films deposited by sputtering in an argon atmosphere or by evaporation.<sup>17</sup> They showed that this was due to a much lower density of states in the gap in

the glow discharge material. Both p and n type amorphous silicon films were achieved by adding boron ( $B_2H_6$ ) or phosphine ( $PH_3$ ), respectively, to the silane discharge. Subsequently it was shown that the glow discharge material contained 5-50 at. % hydrogen.<sup>17,18,19</sup> In 1976 Paul et al. showed that silicon films sputtered in the presence of hydrogen could also be doped by adding phosphine or diborane to the sputtering atmosphere. This indicated that the presence of hydrogen in the glow discharge material was more than incidental. Apparently the hydrogen in the deposition atmosphere was incorporated in the film, reducing the density of states in the gap,  $g(E)$ , to a level far below that of the unhydrogenated material, permitting sensitive boron and phosphorus doping.

One of the effects of hydrogen in amorphous silicon is to passivate dangling bonds, as evidenced by the difference in electron spin resonance signals between unhydrogenated sputtered and hydrogenated sputtered or glow discharge produced materials. The latter films have very weak ESR signals as contrasted with evaporated films in which ESR measures approximately  $10^{20}$  paramagnetic dangling bonds per  $cm^3$ .<sup>21,22,23</sup> At the same time hydrogenated amorphous silicon films show a much lower optical absorption at sub-bandgap photon energies.<sup>23</sup> Field effect measurements on the hydrogenated material

yield much lower values for the density of states<sup>16</sup> and the room temperature conductivity decreases by orders of magnitude and becomes activated.<sup>24</sup>

The above changes with hydrogenation are all consistent with the removal by hydrogen of dangling bonds which would otherwise appear as a large number of states in the gap. Sub-bandgap photon absorption is due to electrons excited to or from states in the gap and the high, unactivated conductivity is consistent with hopping among states of high density near the Fermi level. The FET measurements give a fairly direct measure of the density of states in the gap, although the effect of the states at the surface of the semiconductor is difficult to quantify and limits the accuracy.<sup>25</sup> More recent measures of the density of states in the gap by other methods including capacitance-voltage,<sup>26</sup> deep level transient spectroscopy,<sup>27</sup> analysis of space charge limited currents<sup>28</sup> and several others<sup>29,30,31</sup> confirm the low density of states at mid-gap in hydrogenated amorphous silicon ( $<10^{15}-10^{18} \text{ cm}^{-3} \text{ eV}^{-3}$ ) but do not agree on the shape of the  $g(E)$  curve nor on its absolute magnitude.

The amount of hydrogen incorporated in the films is, however, many times larger than the amount needed to simply tie up dangling bonds.<sup>17,32</sup> Optical absorption measurements on sputtered material show that the

optical bandgap increases with increasing hydrogen incorporation, even beyond the point where the density of gap states is minimized.<sup>12,23</sup> Studies of  $g(E)$  indicate that an erosion of the states at the top of the valence band occurs for the highest hydrogen concentrations.<sup>23</sup> This evidence suggests that the role of hydrogen is more complicated than simply passivating the dangling bonds and that the material should be considered to be a silicon-hydrogen alloy.

Hydrogenated amorphous silicon films have been produced by a variety of methods including glow-discharge decomposition of  $\text{SiH}_4$  and  $\text{Si}_2\text{H}_6$ ,<sup>16,32</sup> dc,rf and triode reactive sputtering,<sup>23,33</sup> chemical vapor deposition (CVD) of  $\text{SiH}_4$  and higher order silanes,<sup>33,34</sup> hydrogen plasma post-hydrogenation of CVD films,<sup>35</sup> and evaporation in the presence of atomic hydrogen.<sup>37</sup> Currently the method producing the best films, as measured by solar cell performance is the glow discharge technique<sup>9</sup> (10%) followed by sputtering<sup>38</sup> (4%) and CVD with post-hydrogenation<sup>39</sup> (2.7%). The disparity in the efficiencies is probably exaggerated since considerably more effort has gone into optimizing glow discharge cells. The structure of the 10% cell includes a window layer of wide band-gap Si:C:H material which passes short wavelength photons to the active region of the cell.

Doping of amorphous silicon is now a routine operation, used to control the conductivity, to ensure good metal-semiconductor contacts and to produce p-n junctions for rectification and photovoltaic conversion. Most commonly, either diborane or phosphine is mixed with the silane feed gas in the glow discharge and CVD methods, or with the argon-hydrogen atmosphere during reactive sputtering, to produce p or n type material.<sup>12,16,39</sup> Other techniques include ion implantation,<sup>40</sup> which appears to result in a somewhat smaller doping efficiency and co-sputtering from two targets simultaneously,<sup>41</sup> which results in a low doping efficiency.

It should be noted that hydrogen is not unique in its role as a terminating agent. Ovshinsky and Madan report films deposited from  $\text{SiF}_4\text{-H}_2$  mixtures which have a low density of states in the gap and exhibit efficient carrier generation.<sup>79,42,43</sup> High efficiency solar cells have been fabricated using the fluorinated material.<sup>44</sup>

## 2.2 Bias Sputtering

Sputtering is a technique in which material ejected from the target by energetic ions is deposited on a substrate. For rf diode sputtering this occurs when positive ions are accelerated out of the plasma

to the target which is at a large negative voltage. The surface of the deposited film is in constant contact with the plasma and is bombarded by numerous species in addition to the sputtered neutrals.

These include, in the argon-hydrogen plasma, argon and hydrogen ions, atoms and molecules, secondary electrons, ionized sputtered atoms, photons, and impurities in various charge states. At a typical sputtering rate of 200 Å/minute at 20 millitorr argon pressure the neutral argon particle flux is approximately  $10^4$  times the flux of sputtered particles. (The fluxes are on the order of  $10^{19}$  and  $10^{15}$  atoms/cm<sup>2</sup> sec. respectively.) The particle flux of an impurity at a partial pressure of  $10^{-6}$  torr (50 ppm)<sup>45</sup> is also about  $10^{15}$  atoms/cm<sup>2</sup> sec, suggesting that the degree of system purity may have marked effects on film properties. The ratio of the various particle fluxes as well as the energy distribution of the particles interacting with substrate may be varied by changing certain deposition parameters. The total pressure of the sputtering atmosphere may be varied, the relative partial pressures of the various gasses may be changed (including the impurity gasses!), the sputtering power is variable and adjustment of the target to substrate distance is possible. Other deposition variables include deposition angle, substrate material, discharge frequency, power

applied to the substrate, substrate temperature, target size, target voltage, deposition rate, and various plasma parameters.

The effects of most these parameters on amorphous silicon films have been studied to some extent.<sup>12,23</sup> The fact that many of these variables interact with each other and with the sputtering system in ways that are difficult to quantify, and the sheer number of deposition parameters preclude an all encompassing n-dimensional study of sputter deposition of amorphous silicon.

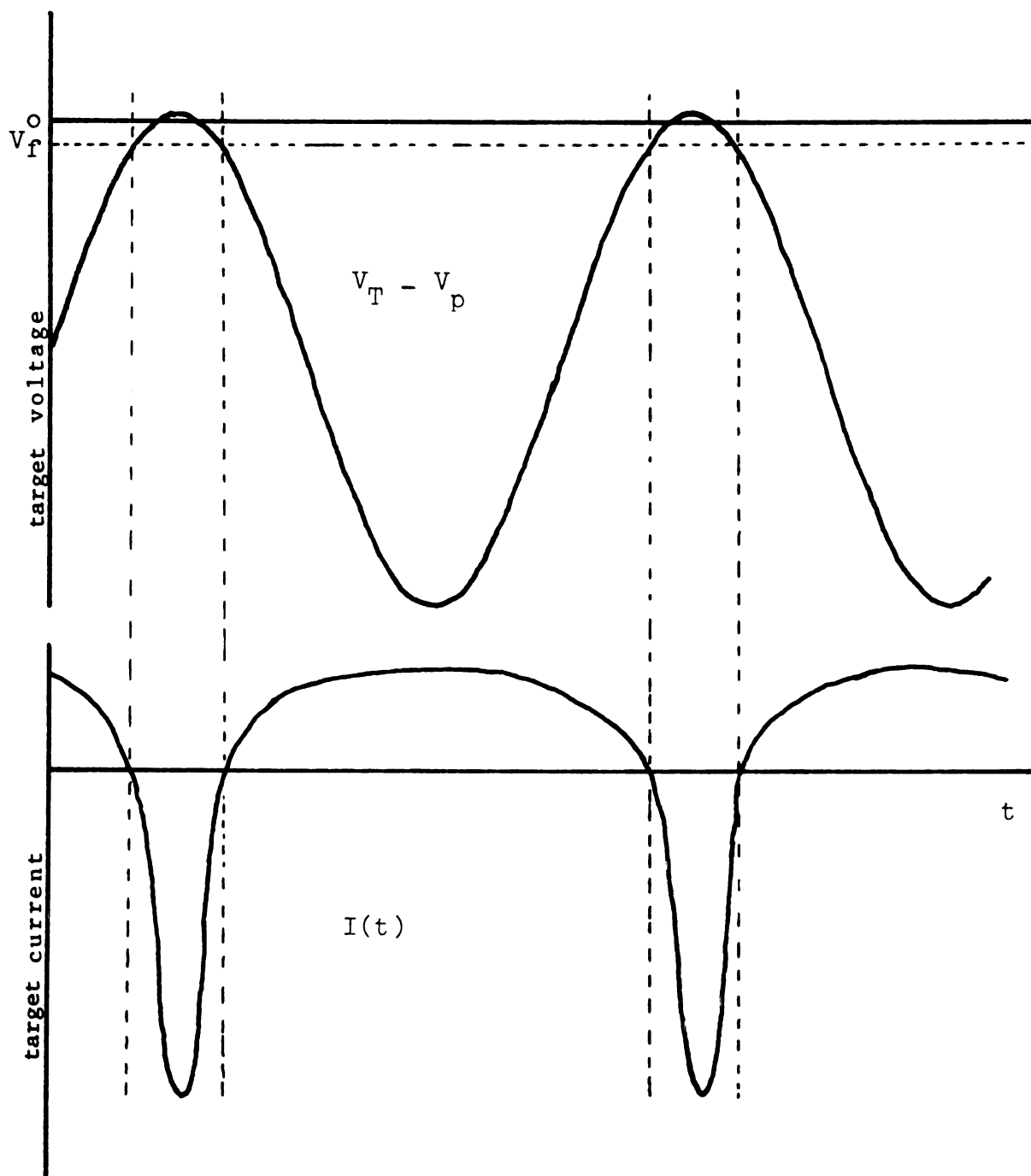
In one sense, however, the properties of the film can be viewed as being controlled by just three things, the substrate, the temperature and the bombardment of the film by the deposition environment. The first two are relatively easily controlled, and while control of the third is much more difficult and depends on many experimental variables, it is crucial in determining the properties of the film.

Biasing the substrate has a very direct effect on both the number and energy of charged particles bombarding the growing film from the plasma and it is reasonable to expect that this might have some effect on the properties of the resultant material. Indeed, in the extreme of very large negative bias the substrate becomes a second target and is sputtered itself.

At smaller bias the lower energy ions seem to selectively remove material from the film. Chapman<sup>45</sup> gives several examples in which the properties of certain films depend rather strongly on the substrate bias.

Practically it is only possible to bias the substrate negatively with respect to the plasma, for if a positive bias is applied, a large electron current flows from the plasma and the plasma potential rises, keeping the substrate slightly negative. The ion current to an electrode at a negative potential is considerably smaller and perturbs the plasma less.

In an rf bias sputtering system the negative dc potential on the target is usually induced by the interaction of the plasma with the target, to which a capacitively coupled rf voltage has been applied. A dc voltage is induced with respect to the plasma since the I-V characteristic of an electrode in a plasma is extremely non-linear. During the negative part of the voltage cycle a positive ion current flows. As the voltage becomes less negative and exceeds the floating potential (the voltage at which the electron and ion currents are equal), a very large negative electron current begins to flow. In the steady-state, for a capacitively coupled electrode, the current must average to zero and a dc bias equal to about half the peak to peak rf voltage is established. These voltages and currents are sketched in Figure 2.1.



- $V_T$  - target voltage
- $V_p$  - plasma potential
- $V_F$  - floating potential
- $I(t)$  - target current

Figure 2.1 Target voltage and current.

Sputtering occurs as positive ions are accelerated out of the plasma and bombard the target, ejecting target material.

The previous discussion applies to any electrode in contact with the plasma, and in a simple rf diode sputtering system both the target electrode and the electrode consisting of the rest of the sputtering chamber are connected to the rf power source. See Figure 2.2a. That the target is sputtered, rather than the walls of the sputtering chamber is due to the asymmetry in the sizes of the two electrodes, (the target and the rest of the system). The ratio of the voltages on the target and walls is expected to vary as

$$V_t/V_w = (A_w/A_t)^\alpha$$

where  $\alpha > 1$  and  $A_w$  and  $A_t$  are the areas of the walls and target.<sup>45</sup> The target voltage is typically in the range of 500-2,000 volts, depending on system geometry. For bias sputtering the dc voltage on the substrate electrode with respect to the plasma may be controlled in much the same way by applying to it a variable rf voltage. See Figure 2.2b. Of course the desired substrate voltages are much less than the target voltage.

A useful consequence of the lack of dc current flow in the rf sputtering circuit is the ability to sputter insulating targets or bias the surface of

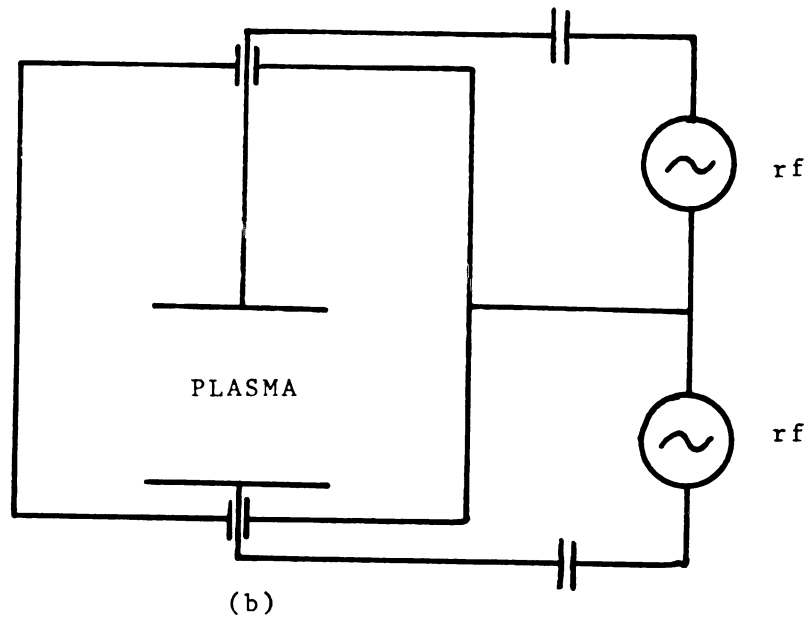
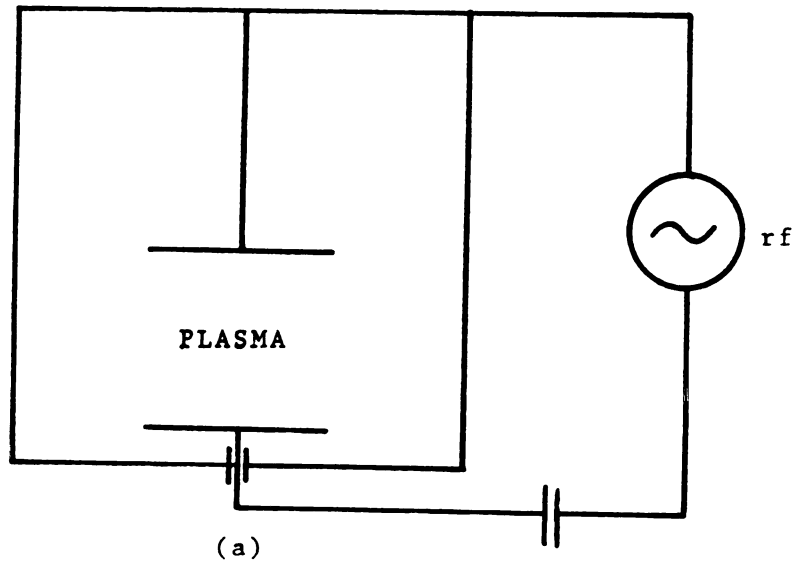


Figure 2.2 (a) rf diode sputtering.  
(b) rf bias sputtering.

insulating substrates. In this case the insulating material acts as a second capacitor in series with the blocking capacitor, and providing this second capacitance is large enough, the operation of the system is not changed.

### 2.3 Sputtered Amorphous Silicon

As implied earlier, sputtered and glow discharge produced amorphous silicon are very similar materials.<sup>12,23</sup> Currently, the sputtered material is somewhat inferior for the production of solar cells. Evidence suggests that hydrogen is less efficient in reducing defects when the material is deposited by sputtering, since for sputtered films a higher concentration of incorporated hydrogen is necessary to achieve the same density of states in the gap.<sup>46</sup> The additional hydrogen incorporated seems to have the effect of modifying the band structure somewhat, as evidenced by changes in the optical absorption and may even induce gap states.<sup>47,48</sup> As compared to the best glow-discharge material, sputtered amorphous silicon generally exhibits smaller drift mobilities that change more quickly with temperature,<sup>12</sup> as well as a lower radiative transition energy,<sup>46</sup> which are both consistent with a density of states that falls off more slowly away from the band edge.

Hydrogenation of sputtered amorphous silicon is believed to take place primarily at the surface of the growing film, as opposed to the case for the glow-discharge decomposition of silane, where evidence suggests that the film forms as  $\text{Si}_x\text{H}_y$  species condense on the surface.<sup>49</sup> Arguments against the importance of hydrogenation of the target or gas phase reactions include the fact that most of the sputtered material is atomic rather than molecular in nature<sup>50</sup> and that considerably less than one collision with hydrogen atoms or molecules is expected as a silicon atom traverses the distance from the target to the substrate in a typical low pressure rf sputtering system.<sup>51</sup>

#### 2.4 Schottky Barriers

Schottky barriers may be constructed on amorphous silicon with a variety of metals by evaporation, sputtering or by deposition of the amorphous silicon on a metallic substrate. Efficient solar cells have been fabricated employing Schottky barrier structures,<sup>44,52,53</sup> although long term stability is probably not as good as for p-n junction devices.<sup>54,55</sup> Schottky barriers are also used extensively as a diagnostic tool toward understanding the conduction mechanisms and gap states in the material.<sup>56,57,58,59</sup>

Schottky barrier devices have the advantage of simplicity of construction; one merely deposits the

appropriate metal on the semiconductor. Because of this simplicity the connection between material properties and device properties is less complex than for a more complicated multilayer device. At the same time, the Schottky barrier device performance is a useful indication of the suitability of the material for device applications in general. Comparison of Schottky barrier characteristics under illumination is certainly a very direct method for evaluating the suitability of amorphous silicon films produced under various conditions for production of photovoltaics.

## CHAPTER III

### EXPERIMENTAL METHODS

#### 3.1 Introduction

Hydrogenated amorphous silicon films are sensitive to a great number of deposition parameters. This study examines in detail the effects of one, substrate bias. The role of substrate bias in determining film properties is reported for two different target voltages.

In studying the effects of substrate bias, it is of course desirable to keep random variations in other deposition parameters such as gas pressures, substrate temperature, and deposition rate to a minimum to avoid scatter in the data. In addition the results are most meaningful if the films produced are "good" films, that is films with the properties desired for the fabrication of useful devices. With this in mind, the constant deposition parameters were monitored carefully, and the impurities in the sputtering atmosphere were kept to a minimum. The constant deposition parameters, while not optimized, were chosen from previous experience and the literature to give device quality films.

The various measurements were chosen to quantify the effects of substrate bias on the optical and

electrical properties of the films as well as to evaluate the suitability of the films for device construction. This chapter describes the equipment and procedures used to produce and characterize these films. The bias sputtering system is described in detail, along with the measurements used to ensure a reproducible deposition environment. System purity is examined and film deposition procedures are discussed. Finally, the various electrical and optical measurements used to evaluate changes in film properties are summarized.

## 3.2 Film Deposition

### 3.2.1 Deposition systems

The amorphous silicon films in this research were deposited by rf diode sputtering and the metal films either by evaporation or sputtering. Two evaporators are available in the Physical Electronics Laboratory, one used exclusively for evaporation of aluminum and the other for various other metals. The aluminum evaporator is a Cooke Vacuum Products model CV-300, pumped by a two inch air cooled diffusion pump, capable of a base pressure of about  $3 \times 10^{-6}$  torr without nitrogen in the cold trap, as measured by an integral cold cathode gauge. The second evaporator is made by Consolidated Vacuum Corporation and is pumped by a 4 inch water-cooled diffusion pump. The freon trapped system

achieves a base pressure of  $1 \times 10^{-6}$  torr measured with an ionization gauge and is used to evacuate both the evaporation bell jar and the sputtering system.

The rf diode sputtering system, used to deposit the amorphous silicon and molybdenum films in this study, is designed to be a flexible and easily maintained system. (Figures 3.1 and 3.2) The stainless steel sputtering chamber itself is 8 inches high and 6 inches in diameter, and is piped to the diffusion pump via several 4 to 5 cm diameter sections of stainless steel and copper tubing totaling about 1.4 meters in length. Access to the interior of the chamber is through a removable top sealed with a copper gasket. The top contains electrical and mechanical feed throughs and an observation window. In addition, it supports the substrate holder and associated shields. The chamber itself has ports for pumping, gas inlet, pressure measurement, optical observation, as well as an unused port. The target and its shield are located at the bottom of the chamber. Except for the top and the unused, pumping and optical ports, which are sealed with copper gaskets, all demountable parts are sealed with O-rings.

The target and substrate supports are electrically insulated to permit the application of rf or dc voltages for sputtering and substrate biasing. To prevent sputtering of the supports themselves, each

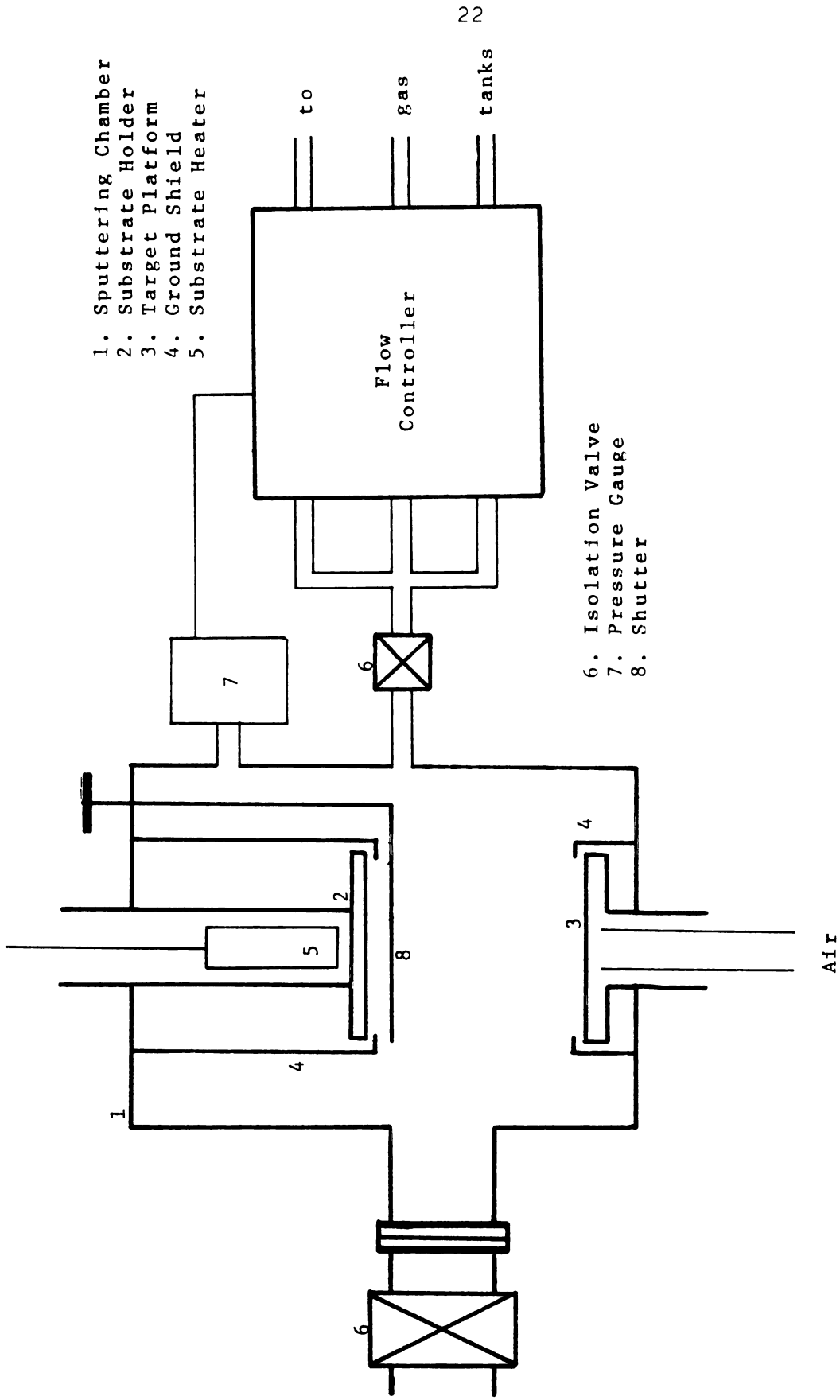


Figure 3.1 Sputtering system schematic.

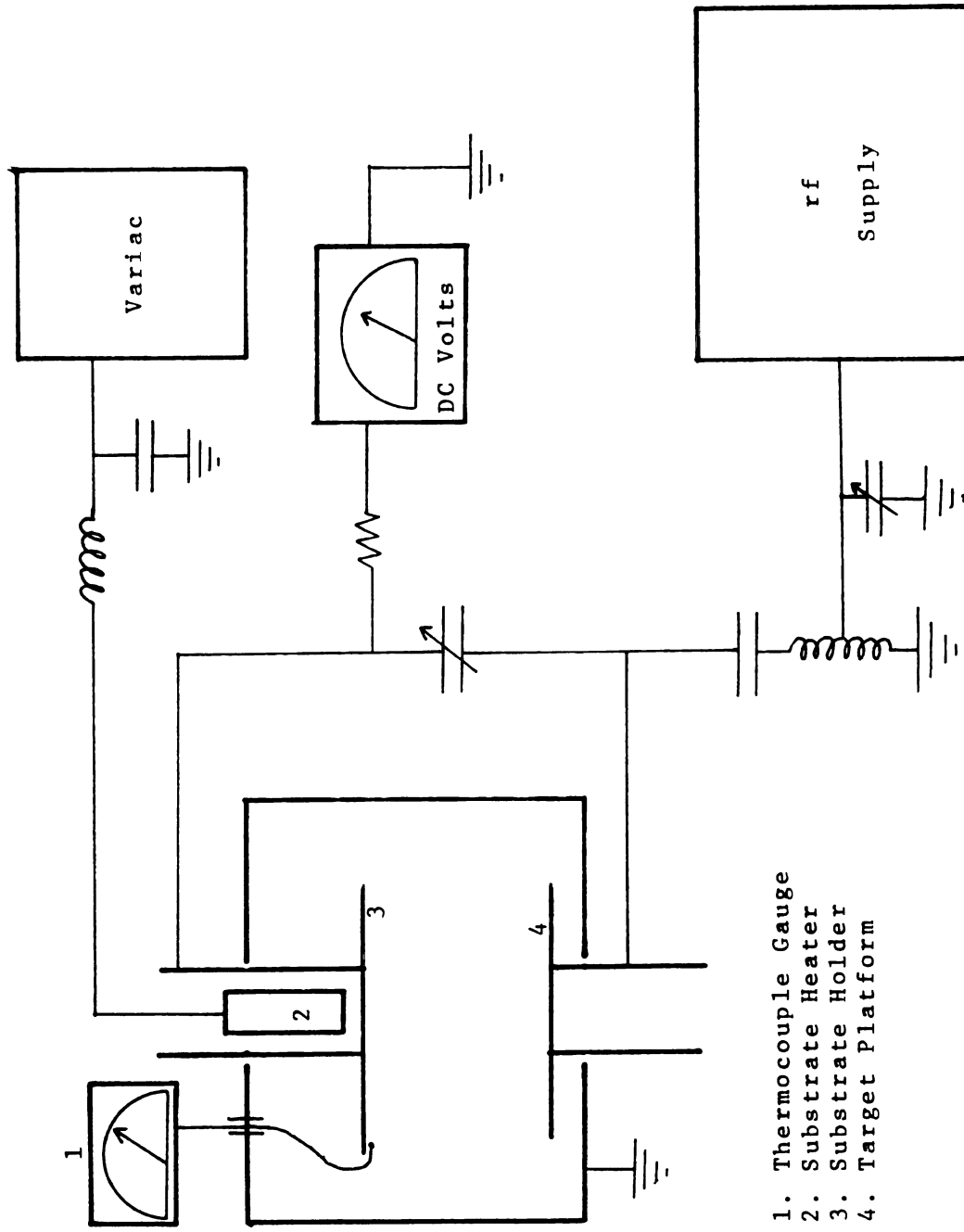


Figure 3.2 Sputtering system electrical schematic.

is provided with a grounded shield which exposes only the desired surface of the target or the substrate to the plasma. The spacing between the shield and the support (to which power is applied) is sufficiently small that a second plasma is not excited inside the shield.

The system can accommodate any size targets and substrates that will fit inside the 6-inch diameter chamber, though presently the heated substrate holder is 2 inches in diameter and target shields have been constructed only for 2 and 3 inch targets. The target is a disk of the material which is to be sputtered and is set on the target holder near the bottom of the chamber. The target holder is air cooled since sputtering is a rather inefficient process, at least in terms of amount of energy transferred to ejected particles,<sup>50</sup> and the target absorbs a considerable amount of power. On the other hand, for good quality amorphous silicon films the substrate should be held at an elevated temperature of about 250°C, which even at the largest negative substrate biases, requires heating.

The rf power is supplied through a matching and power splitting network to the target or the target and substrate as desired. Incident and reflected powers are measured by a Bird model 43

wattmeter in the feedline. Generally a match to less than 1% reflected power is achievable, but the exact amount of power absorbed in the sputtering chamber is uncertain to the amount of power lost in the matching network.

The substrate holder is hollow to accommodate a resistance heater. This heater is electrically isolated to dc voltages internally, and is connected to a variable voltage supply through an rf choking network. The substrate temperature is measured by an iron-constantin thermocouple held to the front surface of the substrate by a small stainless steel clip. The surface temperatures of substrates in sputtering systems are notoriously difficult to measure accurately, and this method may not give the absolute surface temperature with a high degree of accuracy, but we believe it allows reproducible control of substrate temperature from run to run.

Sputtering gasses are admitted to the system through a 3 channel MKS flow controller. The pressure in the sputtering chamber is monitored with an MKS Baratron capacitance manometer type vacuum gauge with a resolution of 0.1 millitorr. In addition thermocouple gauges measure the pressures at the throat of the diffusion pump and in the foreline. The gas flow system, from the regulators through the flow



meters and solenoid valves, to the sputtering system, is constructed of 1/4 inch stainless steel tubing connected with Swagelok or Gyrolok fittings.

During a typical sputtering run the argon flow rate is set at 1.25 sccm (standard cubic centimeters/minute) and the hydrogen flow rate at .76 sccm, resulting in argon and hydrogen partial pressures of 7.5 and 0.55 millitorr respectively. The pressure of each gas is measured by first establishing the flow for a sufficient period of time for the instrumentation to reach equilibrium, then suddenly interrupting the flow while monitoring the drop in pressure. The measured pressures typically vary less than 5% + gauge resolution from run to run. Each partial pressure is also relatively independent of the other, as would be expected with conductance in, or close to the molecular flow regime. The pumping speed of the unthrottled diffusion pump is sufficient that the pressure at the diffusion pump, at the end of the sputtering chamber's 1.4 meter pumping tube, is quite low. The result is that the pressures of the gasses in the sputtering chamber are determined solely by the gas flow rates and the conductance of the pumping tube.

$$\Delta P = \frac{Q}{C} = \frac{\text{Flow}}{\text{Conductance}}$$

For argon, the flow is 1.25 sccm for a typical sputtering run and the conductance is  $1.27 \times 10^5 \text{ cm}^3/\text{minute}$ .

$$\Delta P = \frac{1.25 \text{ sccm}}{1.27 \times 10^5 \text{ cm}^3/\text{min}} = 9.87 \times 10^{-6} \text{ Atm.}$$

$$= 7.5 \text{ m Torr.}$$

### 3.2.2 System Purity

Although the sputtering system is kept as clean as possible, impurities from several sources are present during the sputtering process. Leaks in the vacuum system, outgassing, impurities in the feed gases and unwanted sputtering from parts of the system other than the target may all contribute impurity atoms to the growing film. The following discussion quantifies the roles of these various sources of impurities.

First consider the effect of outgassing and system leaks on system purity. To minimize contamination due to outgassing and to avoid contamination of the feed gasses, the entire sputtering system including the flow system and regulators is evacuated overnight with the sputtering chamber heated to  $100^\circ\text{C}$  and the substrate heater on. In addition the gas lines are never exposed to the atmosphere beyond the isolation valve to prevent absorption of contaminants between runs. Before each run a pressure rise leak/outgassing rate test is performed. In order to carry out this

test, the system is isolated from the pumps and the pressure rise over a given time is noted. Typically the pressure rises about 1 millitorr/hour for the whole system and less than .3 millitorr/hour for the isolated can alone after overnight pumping, and still less for longer pumpdowns.

With the system's 4 liter volume, this corresponds to a leak/outgassing rate of  $8.75 \times 10^{-5}$  sccm. Assuming the conductance of the pumping tube is approximately the same for the leak/outgas gasses as for argon, the partial pressure of these gasses is  $5 \times 10^{-7}$  torr. The assumption of a similar conductance is necessary since the conductance of the section of tube which controls the pressure in the can varies considerably with the mass of the particle in question. (The conductance varies as the inverse of the square root of the mass in the limit of molecular conduction.) If for the moment, the above is considered to be the only source of contaminants, the gas purity is given by the ratio of the sputtering gas pressure to the pressure due to the measured leak/outgassing rate.

$$\frac{8.05 \times 10^{-3}}{8.05 \times 10^{-3} + 5 \times 10^{-7}} = 99.994\%$$

The pressure rise experiment indicates the summed contribution of leaks and outgassing. It is useful to determine whether this represents leaks

and outgassing of air or sources of sputtering gas (outgassing, and leaks from the gas cylinders).

The system has been thoroughly leak tested using a VEECO mass spectrometer helium leak detector. Sections of the system were immersed in a helium atmosphere and no leaks were found with a detection threshold of about  $2 \times 10^{-7}$  sccm. Helium diffusion through the teflon tape seals in the Matheson regulators was observed at a rate of  $3.8 \times 10^{-6}$  sccm after about 30 minutes immersion in helium, but an air leak is considered unlikely.

In addition a rather crude experiment was performed to determine the composition of the gas in the leak/outgassing test. After the system was isolated from the pumps, the pressure inside the sputtering chamber, due to leaks and outgassing, was allowed to build up to 5 millitorr over a period of several hours. A discharge was started and compared with discharges in air and in the normal argon-hydrogen atmosphere. The discharge was bluish, identical in appearance to the argon-hydrogen discharge. On the other hand, air bled into the evacuated chamber produced a pink discharge. In addition an air discharge is quickly extinguished as the atmosphere is gettered by the sputtering process. This was not observed in the outgas/leak test discharge. Our conclusion from these

tests is that the leak/outgassing rate is due primarily to argon and hydrogen gasses from the feedlines, and the true impurity level due to leaks and outgassing is considerably lower than the pressure rise test indicates.

The possibility exists that the plasma stimulates outgassing at the beginning of the run. For this reason and others the target is generally sputter cleaned for at least 10 minutes before deposition starts with the substrate shuttered.

The hydrogen and argon sputtering gasses are grade 5.5 and 5.8 respectively, meaning that the hydrogen is 99.9995% pure and the argon is 99.9998% pure. Assuming impurities of molecular weight similar to argon, the impurity partial pressure for a 1.25 sccm argon flow and a 0.76 sccm hydrogen flow would be  $3.8 \times 10^{-8}$  torr.

Sputtering of unwanted particles, another major contributor to film impurities, is more difficult to quantify. In the simplest scheme, power is applied to the target which becomes very negative with respect to the plasma. If the ratio of the ground electrode area (everything but the target) to the target area is large enough, the plasma will acquire only a small positive voltage with respect to ground. Since the ion temperature is low in a typical sputtering plasma (500 °K)<sup>51</sup> and sputtering is a threshold phenomenon

(20-30 eV) essentially no material will be sputtered from the walls by normal ions from the plasma under the above conditions. Unfortunately things are not always this simple. The potential of the plasma certainly can exceed threshold and small numbers of fast ions and neutrals bombard all exposed surfaces of the system, sputtering whatever coats the walls. Therefore the sputtering purity, and what the impurities are may depend on the past history of the chamber, and we and others see some evidence for this.<sup>60</sup>

Finally, it is noted that the base pressure achieved in the sputtering system is  $1 \times 10^{-6}$  torr. To the extent that the base pressure represents impurities introduced by the pumping system, for example diffusion pump oil compounds, this base pressure is an important factor in determining the purity of the sputtering atmosphere. In the worst case, if impurities at a pressure of  $1 \times 10^{-6}$  torr are introduced by the pumping system, the system purity due to this source alone is

$$\frac{8.05 \times 10^{-3}}{8.05 \times 10^{-3} + 1 \times 10^{-6}} = 99.988\%.$$

If the composition of the gas in the leak/out-gassing test is indeed mostly argon and hydrogen, it appears that the greatest contribution to impurities in the film is due to either the finite ultimate pressure

of our pumping system or to the sputtering unwanted particles, depending on the contribution of the latter. Gas purity and leak/outgas rates are probably relatively less important.

### 3.2.3 Bias sputtering

The dc target voltage measured during the silicon deposition runs was either 2,350 volts for the small (2 inch) target or 1,310 volts for the large (3 inch) target. In either case, this voltage is merely the average of the rf induced voltage, equal to about half the rf peak to peak voltage as described in Chapter II. The voltage output of the rf generator ripples at a 120 Hz rate due to poor filtering in the supply so the rf induced voltage also varies at this rate. In fact, as shown in Figure 3.3, for the high voltage target the induced target voltage is observed to vary by 980 volts from 1,860 to 2,840 volts, and the peak instantaneous voltage is about  $2 \times 2,840$  or 5,680 V. Similar results are seen for the substrate as it is biased, although the voltages are much smaller. These voltages are important since they represent the instantaneous voltages available for acceleration of charged particles in the system.

Most of the voltage in the sputtering system appears across an approximately 1 cm sheath adjacent to the target. Whether the energy of particles

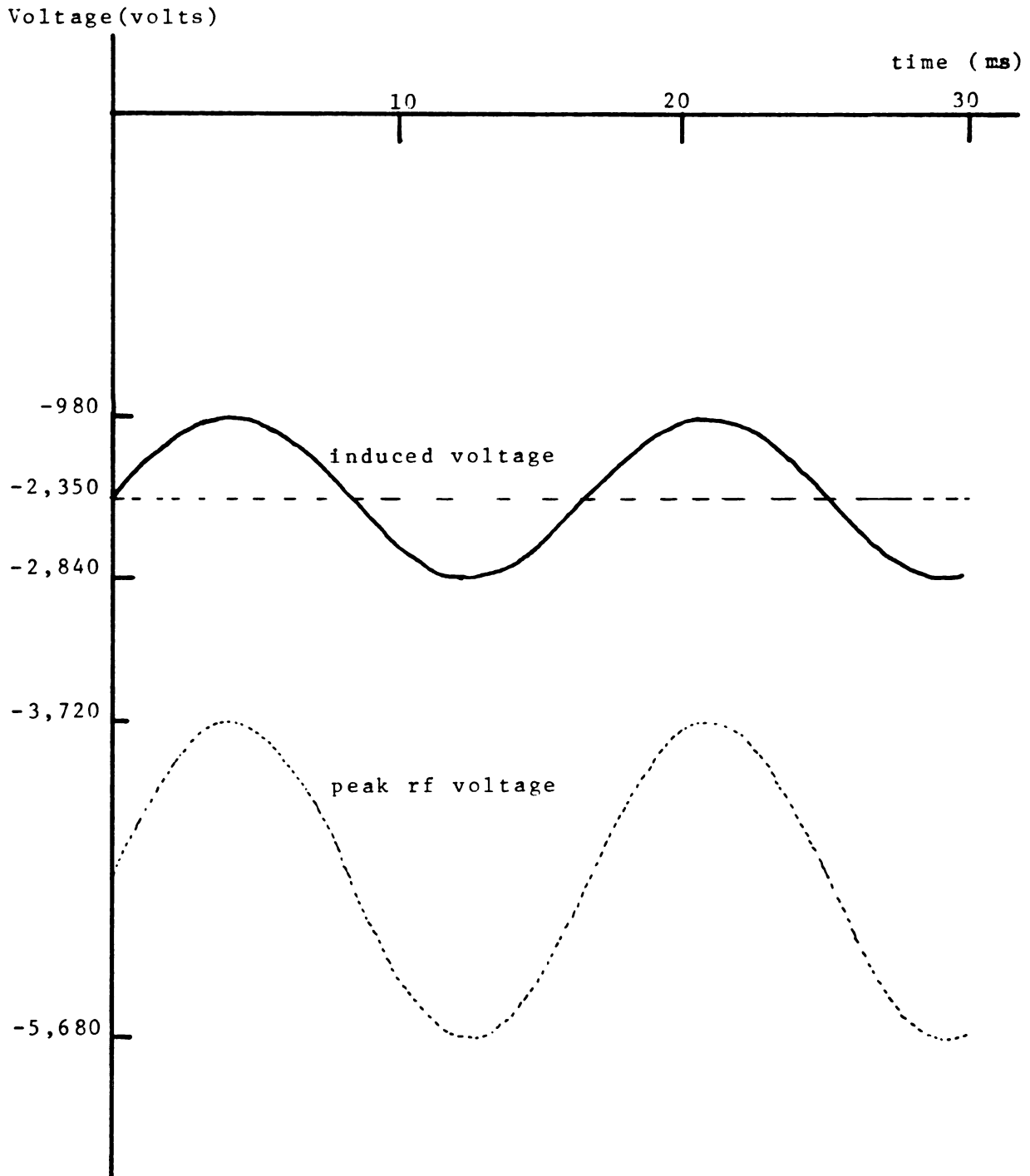


Figure 3.3 Target voltages.

accelerated across the sheath is controlled by the instantaneous or the average sheath voltage depends on the length of time required for the particle to traverse the high field region. The heavier, slower ions cross only after several oscillations of the rf field and so see the average potential. On the other hand, the lighter secondary electrons emitted by the target under bombardment move much more quickly and respond to the instantaneous field. Lighter ions have an intermediate energy spread. For example, a 500 eV electron travels at a velocity of  $1.3 \times 10^9$  cm/sec, traversing the sheath in  $7.5 \times 10^{-10}$  seconds while a 500 eV argon atom travels at  $4.9 \times 10^6$  cm/sec, travelling 1 cm in  $2 \times 10^{-7}$  sec. The period of the 13.56 MHz oscillation is  $7.4 \times 10^{-8}$  sec, intermediate between the two transit times.

From the above argument, for our small target, one would expect secondary electrons accelerated away from the target to have a variety of energies, ranging up to 5,680 V, while the argon ions arriving at the target would show a smaller energy spread centered around 2,350 V.

Particles accelerated in the vicinity of the target and bombarding the substrate with significant energy include the aforementioned electrons, argon and hydrogen ions neutralized at the target and

reflected to the substrate, negative ions formed in and accelerated out of the target sheath region, photons formed by bombardment of various surfaces by electrons and ions and the sputtered atoms themselves which are typically ejected at energies of 1-15 eV.<sup>50</sup> The maximum energies of all these particles except the neutral sputtered atoms depend strongly on the target voltage, and so if damage by bombardment is important, the target voltage may play an important role. A large part of the substrate heating is due to the energetic electrons<sup>50</sup> and the source of most of the argon impurity in the film is energetic argon atoms.<sup>61</sup> Sputtering due to high energy negative ions and damage from high energy photons have also been observed at the substrate.<sup>51</sup>

A much larger number of low energy neutral and charged particles also bombard the substrate. Control of the lower energy charged particles in the vicinity of the substrate is possible through substrate bias. Reported effects of bias sputtering include less incorporation of argon, variations in resistivity, structural changes, changes in dielectric strength and etch rates<sup>61</sup> and variations in surface smoothness.<sup>51</sup> These are briefly reviewed in the next paragraph, since such observations in the literature were a motivation for this investigation.

Various mechanisms have been proposed to account for these changes in properties. As the substrate is biased negatively, it becomes a second target and substrate material is sputtered. For silicon this re-emission of material approaches 50% for a 200 volt bias.<sup>50</sup> The dielectric strength of  $\text{SiO}_2$  correlates well with the re-emission coefficient and the quality of bias sputtered  $\text{SiO}_2$  films is attributed to resputtering of molecules in non-optimum positions.<sup>61</sup> Reduction of film contamination by oxygen or hydrogen occurs, at least in metals which react with these gasses, by preferential resputtering. Gold films become more nitrogen contaminated at negative substrate voltages due to implantation of nitrogen ions. Argon concentrations in nickel films decrease up to about -75 volts of substrate bias, then increase as implantation effects became significant at higher bias.<sup>51</sup>

When the substrate and substrate support are biased negatively, all parts exposed to the plasma will be sputtered. This problem is minimized in our sputtering system by fitting the assembly with a grounded shield to prevent the plasma from coming in contact with the support. The front surface of the substrate platform must be exposed to permit film deposition. Net deposition on all exposed surfaces

is observed, leading to the conclusion that this should not be a source of film impurities once there is an initial coating.

The MSU system is capable of inducing large substrate voltages sufficient to promote net sputtering from the substrate rather than deposition. The rate of resputtering is spatially non uniform, probably due to the shielding arrangement, leading to a ring of net sputtering for bias voltages in excess of about 150 volts for silicon or molybdenum. Although inside this ring the thickness of the deposit is quite uniform and net deposition is seen even for a 190 volt bias, 150 volts represents an upper limit for sputtering a film without significant contamination from the platform.

The substrate bias is normally measured as the difference in potential between the substrate platform and the large grounded electrode consisting of the sputtering chamber and shields. Perhaps a rather more meaningful voltage is the difference in potential between the plasma and the substrate platform. However the plasma potential is not easily measured on a regular basis. The measured bias should certainly yield reproducible control of the sputtering conditions, and since the plasma potential is expected to remain almost constant with respect to bias, the

error should merely shift the voltage axis by a fixed amount.<sup>62</sup>

Since voltages are measured on the target and substrate platforms, rather than on the exposed surfaces, the question arises as to what the surface voltages of the target and substrate really are. The target is a conductor and the dc current flow is essentially zero, so the measured voltage corresponds to the actual target voltage. The situation at the substrate is considerably more complex since the substrate is often an insulator and the sputtered film is semi-insulating. Two cases are considered. In the first, applicable to films sputtered to produce Schottky barriers, the film is deposited on an electrically conducting substrate which is in contact with the metallic substrate holder. In this case the voltage at the surface of the substrate will differ from the measured voltage by the voltage drop across the film. With no dc current flow, as is the case for rf induced substrate bias, this will be 0 V. However, when the holder is grounded for a zero V bias run, approximately a 4 mA current flows, corresponding to a current density of  $2 \times 10^{-4} \text{ A/cm}^2$ . From the known properties of the film, the resistance of a 1 cm square perpendicular to the surface is about  $9 \Omega$ , giving a 1.8 mV voltage drop with respect to the

film surface. So for the case of a conducting substrate, the film surface and substrate platform are at essentially the same voltage.

The second case, applicable to coplanar samples, involves an amorphous silicon film deposited on an insulating glass substrate. Again from the known properties of the film, the sheet resistance is about  $1.8 \times 10^9 \Omega/\square$ . Considering a resistance due to about 1 square of material, as typical of resistances in the film plane, a 100 V voltage drop across the film corresponds to a  $5.6 \times 10^{-8}$  A current, much smaller than the currents available from the plasma. Thus it is concluded that in this second case the film must be treated as an insulator.

What is the substrate voltage for this second case? The surface of an insulator or a dc isolated conductor in a plasma charges up to a certain potential, called the floating potential, at which the electron and ion currents are equal. If the surface is not at this potential a net current will flow until the surface is returned to the floating potential. Similarly, if an rf voltage exists at the surface, the current flow over one period of the voltage must be zero, resulting in a dc potential that is more negative than the floating potential due to the non-linear I-V characteristic of the probe-plasma interface.

(Recall that a blocking capacitor in the substrate biasing network ensures zero dc current.) For our system this implies that if the rf voltage is the same at the surface of the insulator as at the surface of the substrate platform (which are both coated with amorphous silicon) the voltage of the surface of the substrate will be the same as the measured platform voltage.

The capacitance of the glass substrate turns out to be  $4.35 \text{ pF/cm}^2$ . This coupled with an ion current which will be less than an estimated  $1 \text{ mA/cm}^2$  at the target,<sup>51</sup> gives an rf voltage drop of less than about 3 volts across the substrate at 13 MHz. These estimates indicate that the voltage at the surface of the insulating substrates may be fairly accurately equated to the measured platform voltage.

In our system, the smallest possible substrate voltage measured with respect to the sputtering chamber for an insulating substrate and the small target turns out to be -40V. This is the potential at which the substrate holder floats when no rf is applied to it, or even when plasma induced rf is shorted to ground with a capacitor. The holder may be grounded to dc also, but this does not ground the surface of the insulating substrate. Bias voltages of 0 V may be achieved, however, for the Schottky barrier samples

since they are deposited on a conducting substrate which can be dc grounded.

The observation that a current flows when the substrate is grounded implies that the plasma in the vicinity of the substrate is different, in potential at least, than the average plasma in contact with the walls of the chamber. This is not unexpected since the substrate is closer to the target than most parts of the chamber.

Because of several of the above factors the substrate voltage bias scale reported by different investigators is probably different from system to system by up to 40 V. For more complete characterization, the plasma potential in the vicinity of the substrate should be measured.

#### 3.2.4 Film Deposition

This section outlines the procedures involved in the deposition of the films examined in this study.

The sputtering system used to deposit the undoped amorphous silicon films was also used to deposit other films over the course of the research. Phosphorus doped silicon films and molybdenum films were deposited before the undoped layer for the Schottky barrier devices and cadmium telluride was sputtered by another researcher in between series of amorphous silicon

runs. Following the sputtering of CdTe and its consequent coating of the sputtering chamber, the sputtering system was disassembled and the coated parts were sandblasted in the machine shop, then cleaned in the laboratory. Thus each series of up to 15 runs began with a relatively clean stainless steel sputtering can. Small changes in the properties of "first run" films as compared to the rest of the films were noted, indicating that the condition of the can does affect the film to some extent.

The substrate used for deposition of all but a few of the initial films was Corning code 7059 barium borosilicate glass chosen for its low sodium content and satisfactory optical and insulating properties.

The substrate cleaning procedure began with an ultrasonic cleaning in an Alconox bath. This was followed by a 5 minute running deionized water rinse, a 15 minute soak in a beaker of boiling 30%  $H_2O_2$  and another identical rinse. The substrate was then dried and mounted on the substrate holder.

Targets used in this research were 2 inch disks of molybdenum and platinum and 2 and 3 inch crystalline silicon wafers. The silicon wafers were slightly doped with phosphorus to resistivities of  $2\frac{1}{2}$  and 6 ohm-cm respectively. Assuming no compensation, these

resistivities correspond to purities of 99.99999% and 99.999996% indicating that the silicon targets were not a significant source of impurities.

After an initial series of runs which tested a variety of device structures, the research focused on just 2 types of devices, coplanar and Schottky barrier. The coplanar devices consist simply of an undoped layer of amorphous silicon deposited on the glass substrate with aluminum electrodes evaporated on top. The Schottky barrier devices have a molybdenum bottom contact followed by a  $n^+$  doped amorphous silicon layer, an undoped layer and evaporated gold Schottky contacts. Details of sample preparation are in Appendix A. The sample structure is shown in Figure 3.4.

### 3.3 Measurements

#### 3.3.1 Optical measurements

Optical properties of and thicknesses of films fabricated over the course of the research were derived from measurements of the transmittance and reflectance of the films at various wavelengths. The experimental set up is sketched in Figure 3.5. A Bausch & Lomb grating monochromator supplies the nearly monochromatic light. Different width entrance and exit slits may be fitted, trading off intensity against spectral purity. The collimated beam is collected directly

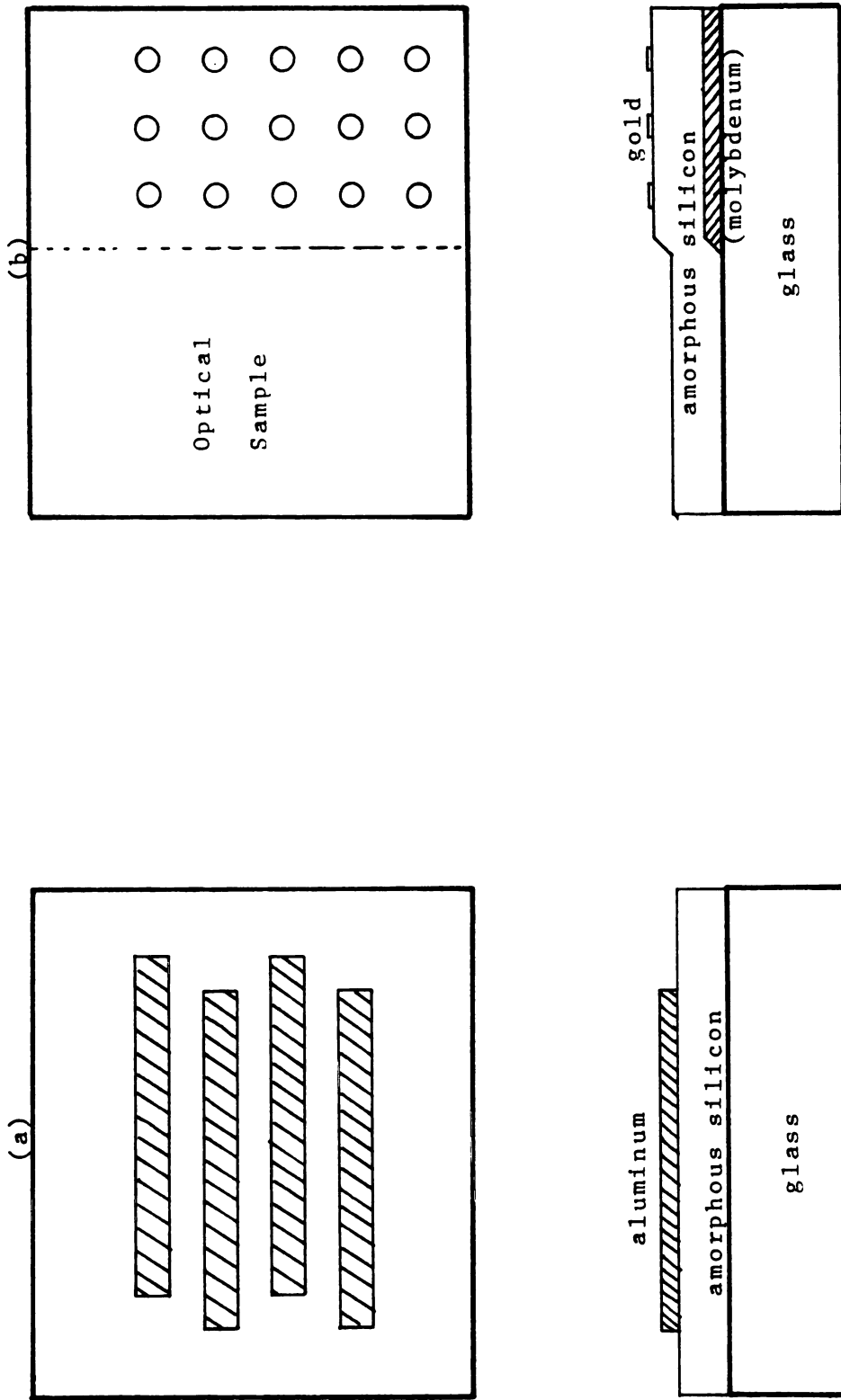


Figure 3.4 (a) Coplanar device structure.  
(b) Schottky barrier structure.

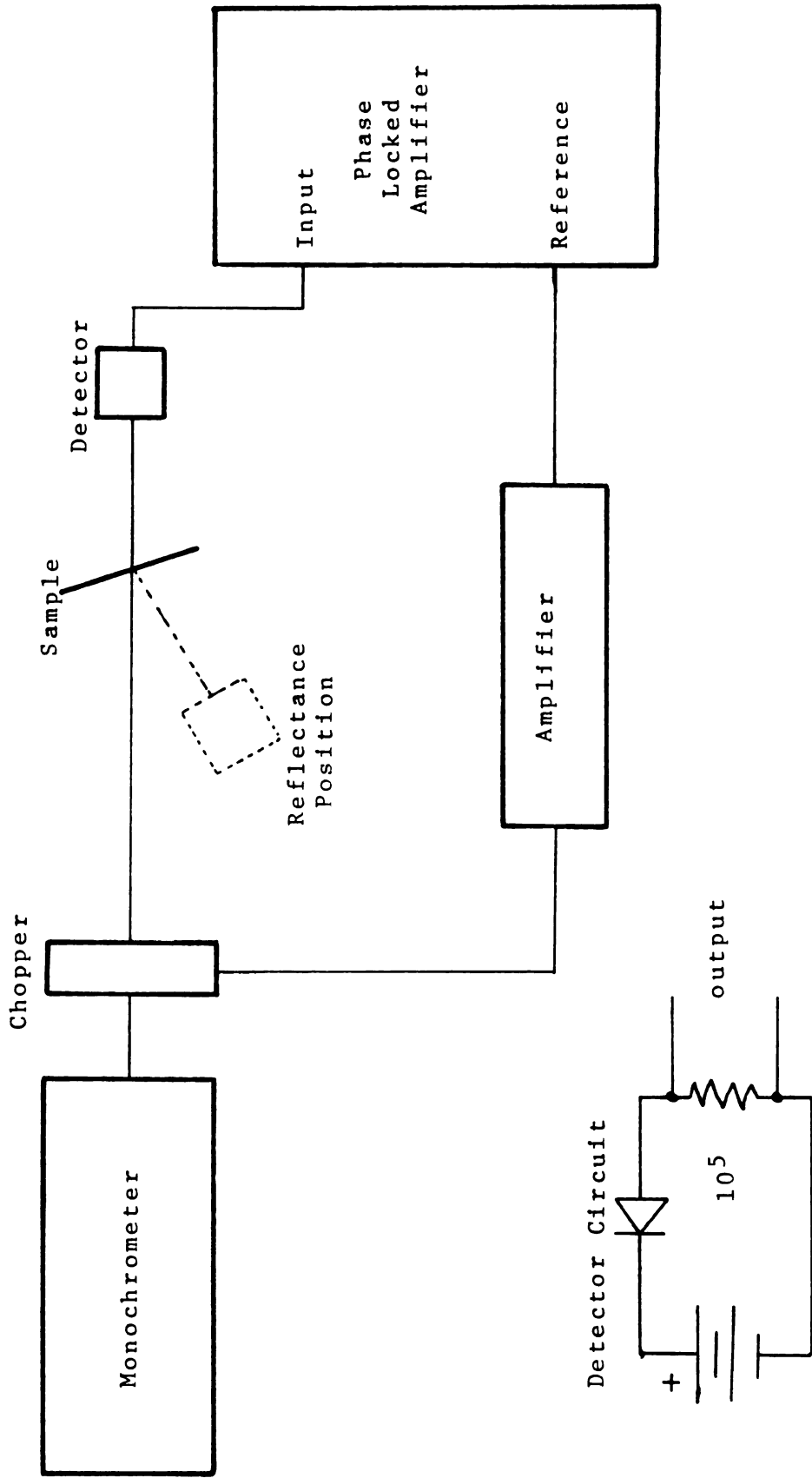


Figure 3.5 Optical measurement schematics.

by a reverse biased silicon photodiode to measure the reference intensity or, after passing through or being reflected from the sample, to measure the transmission and reflection. The collection area of the diode is in all cases sufficiently large that the entire beam is collected, and small placement errors do not change its output voltage. The light at the monochromator is chopped at 200 Hz and the diode voltage is detected by a phase locked amplifier to reduce noise.

To make a measurement at a given wavelength, first the reference intensity is measured without the sample in the sample holder. Next the sample is mounted and a transmission value is read. Third, the photodiode is moved to the predetermined reflectance position and the reflection intensity is recorded. The sum of  $T = \text{transmission/reference}$  and  $R = \text{reflection/reference}$  add to 1 to within 1% for non-absorbing samples. The 200 Hz current output of the silicon detector has been found to be linear for intensities corresponding to output voltages between 10  $\mu\text{V}$  and 500 mV and is presumed to be linear at lower intensities since under low injection conditions the photodiode is a linear device. A small area germanium detector is used at photon energies below the bandgap of silicon, but only for location of reflection and transmission maxima

and minima since the active area is small and placement is critical.

### 3.3.2 Index of Refraction and Thickness Measurement

The index of refraction is one of the properties used to characterize and compare amorphous silicon films. In addition, the value of the index is necessary to determine the thickness of the film by interference of light within the film, a method that has proved very useful in this research.

The index of refraction is measured at sufficiently long wavelengths that the film is transparent. Under these conditions, if the film is thicker than about  $0.15\mu$ , maxima and minima in the reflected and transmitted light are seen corresponding to constructive and destructive interference of light reflected between the film's surfaces. For coatings with index greater than that of the substrate, at a maximum in  $R(\lambda)$ , the amount of light reflected by the film is independent of film thickness, but does depend on the indices of the film, the substrate and the surrounding medium (air). Somewhat surprisingly, the reflectance at a minimum in  $R(\lambda)$  may be shown to be equal to the reflectance of the substrate.<sup>63</sup> Thus to determine the index,  $R(\lambda)$  is measured at a maximum and, since the index of the substrate and of air are known,  $n_f$ ,

the index of the film, may be obtained from the quadratic in  $n_f^2$

$$n_f^4 - 2n_a n_s \left(\frac{1+R}{1-R}\right) n_f^2 + n_a^2 n_s^2 = 0$$

where  $n_a$  is the index of the surrounding medium, air,  $n_s$  is the index of the substrate and  $R$  is the reflectance of the sample, corrected for light reflected from the back surface of the substrate.<sup>63</sup>

Once the index of refraction of the film is known, the thickness may be found by determining the wavelengths at which minima in  $R(\lambda)$  occur and applying the following equation, valid for transparent films of index greater than the substrate index.

$$d = \frac{m\lambda}{2n_f}$$

$d$  - film thickness

$\lambda$  - wavelength at  $R(\lambda)$  minimum

$m$  - order of minimum

The orders of the minima are determined by trial and error subject to the constraint that all minima yield the same thickness.

Determining the thickness by this method gives excellent repeatability and good thickness accuracy for the amorphous silicon films. The minima can be located to within less than 1% accuracy in wavelength and the accuracy of the index determination is approximately  $\pm 3\%$  giving a thickness accuracy of  $\pm 4\%$ .

Measurements of the thickness of a film deposited on a glass substrate, half of which has been coated with molybdenum give different values for the thickness on opposite sides of the molybdenum/glass border. This is probably due to the unknown phase shift upon reflection from the molybdenum surface. Other possibilities are that the silicon deposits on the metal at a different rate or that the substrate affects the growth of the film sufficiently to change the index measurably. The difference is fairly small and for the most samples the molybdenum side measures about  $200\text{\AA}$  thicker, assuming the phase shift at the molybdenum/silicon boundary is  $0^\circ$ . In a typical  $8000\text{\AA}$  sample, this corresponds to a 2.5% apparent thickness difference. A more complete description of these techniques is given in Appendix B.

Thicknesses of various films were also measured using a Varian  $\text{\AA}$ -Scope multiple beam interferometer, an instrument specifically designed to measure thickness steps in thin films. A Fizeau plate is positioned, slightly tilted, near the specimen, resulting in bright and dark fringes due to the interference of light reflected between the two surfaces. The amount of tilt and contours of the Fizeau plate and specimen determine the spacing and shape of the fringes. The tilt is adjustable and the Fizeau plate is flat, so

any deviation from evenly spaced, parallel fringes is interpretable in terms of a surface contour. Normally a step is intentionally produced by masking the film being deposited. The thickness is then proportional to the fringe shift across the step and is calibrated by the fact that the spacing between fringes is  $\frac{1}{2}$  of the known wavelength of light used in the measurement.

The Å-Scope has a specified accuracy of  $\pm 30\text{Å}$  under the ideal conditions of a highly reflective, flat substrate. In measurements on the films used in this research several other potential sources of error are present. The substrate is not perfectly flat, resulting in curved fringes, the steps are sometimes not coated with highly reflective material, increasing the width of and reducing the contrast of the fringes, and the film in the region of the step is not necessarily representative of the active area of the coating due to the presence of the mask and the mask's location near the edge of the substrate. A more subtle error can occur when the step in thickness has different materials on opposite sides. In this case the phase shift of light reflected from the two surfaces may be somewhat different, resulting in a certain amount of fringe shift not due to surface contour.

Experimentally, thickness measurements on a single sample by the Fizeau fringe method varied 10-20% and generally underestimated the thickness as measured by the more accurate  $R(\lambda)$  method by 15-50%. Therefore thicknesses of amorphous silicon films quoted in this report have generally been measured by observation of minima in  $R(\lambda)$  while thicknesses of opaque films have been measured with the multiple beam interferometer.

The thickness uniformity of a typical film deposited in our sputtering system on a 1 inch square substrate is about  $\pm 5\%$ , the film being thicker in the center and thinner toward the edges. Quoted thicknesses are measured at an intermediate point about  $\frac{1}{4}$  inch from the center of the sample.

### 3.3.3 Optical Absorption Coefficient and Optical Energy Gap

The optical absorption coefficient is also found by measuring  $R(\lambda)$  and  $T(\lambda)$ . At photon energies near and above the optical absorption edge, hydrogenated amorphous silicon absorbs light and the absorption coefficient  $\alpha(E)$  shows a strong energy dependence. Structure in the reflectance and transmittance curves is due to reflection, absorption and interference. See Figures 3.6 and 3.7.

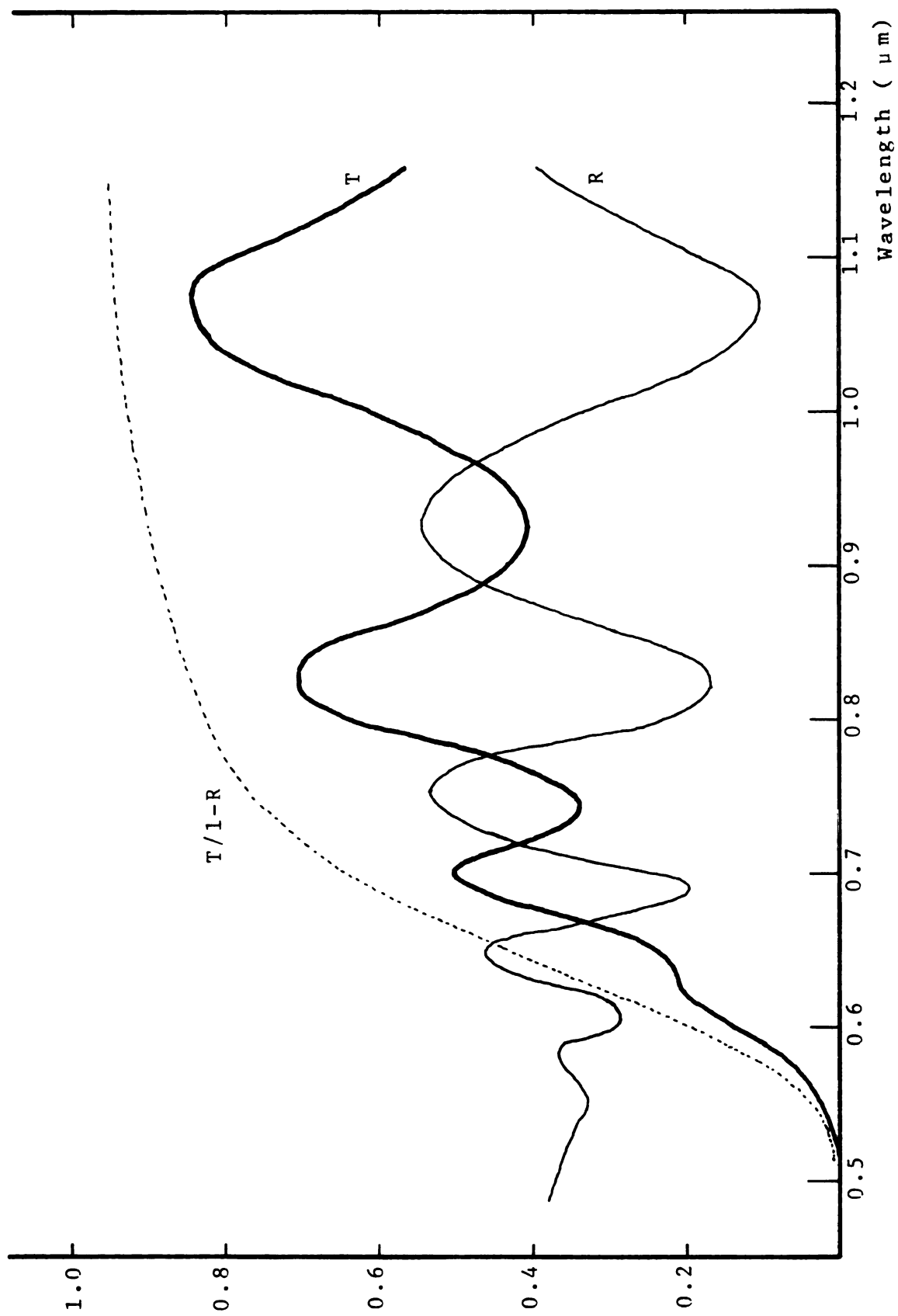


Figure 3.6 R, T and T/1-R vs wavelength (ND-7).

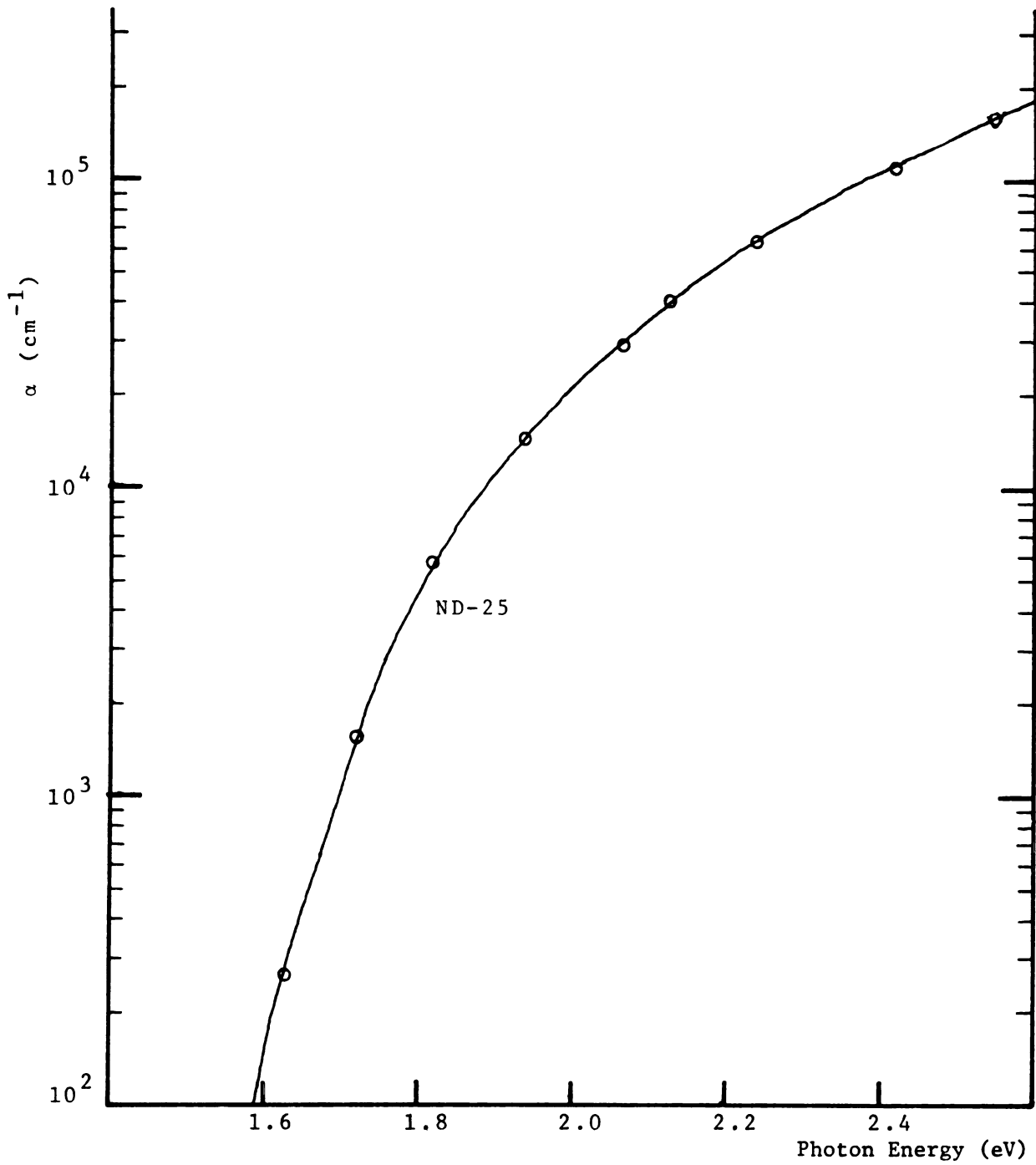


Figure 3.7 Optical absorption coefficient.

For the purposes of this thesis,  $\alpha$  is computed from the following equation:

$$T = (1-R)e^{-\alpha d}$$

T and R are the measured transmittance and reflectance at each wavelength and d is the thickness of the film. This approximation is discussed in detail in Appendix C.

A useful number for comparing amorphous silicon films is the optical energy gap, derived from  $\alpha$ . In amorphous semiconductors the density of states does not fall abruptly to zero at the conduction and valence band edges and consequently the absorption of photons does not have an abrupt cutoff. Therefore the question of how to define an optical energy gap arises. Two methods are commonly used.<sup>13,65,66</sup> In the first the optical gap is defined as the energy at which the absorption coefficient reaches some arbitrary value, usually  $10^4 \text{ cm}^{-1}$ . The second method assumes the absorption edge is similar to that of crystalline semiconductors at sufficiently high energies that the band tails are insignificant.

This work has relied on the second method. Mott and Davis<sup>65</sup> show that, assuming parabolic bands and identical matrix elements for extended and localized states, and no phonon interactions as in a direct gap semiconductor,

$$\alpha(\omega) = \frac{\text{const.} (\hbar\omega - E_{\text{og}})^2}{\hbar\omega}$$

This equation is used to define the optical energy gap  $E_{\text{og}}$ . A plot of  $(\alpha\hbar\omega)^{\frac{1}{2}}$  vs  $\hbar\omega$  will yield a straight line that intersects the  $\hbar\omega$  axis at  $E_{\text{og}}$ . See Figure 3.8. The presence of band tails modifies the plot of  $(\alpha\hbar\omega)^{\frac{1}{2}}$  vs  $\hbar\omega$  somewhat, especially at lower energies where absorption of photons by excitation of electrons to or from the band tails is relatively more important. Experimental results show a good fit to the above equation for  $\alpha > 10^4$ . See Figure 3.9. Determining which part of the curve should be extrapolated to obtain  $E_{\text{og}}$  from the experimental plot is somewhat arbitrary, but since we are more interested in any change in the optical gap than in its absolute value, the choice is not critical, providing it is applied uniformly.

In this research the extrapolation is performed by fitting the best straight line to data points at 487, 512, 553, and 582 nm, which happen to correspond to transmission peaks of filters used in the measurement. The scatter in  $E_{\text{og}}$  results determined by this method turns out to be about  $\pm 1\%$ .

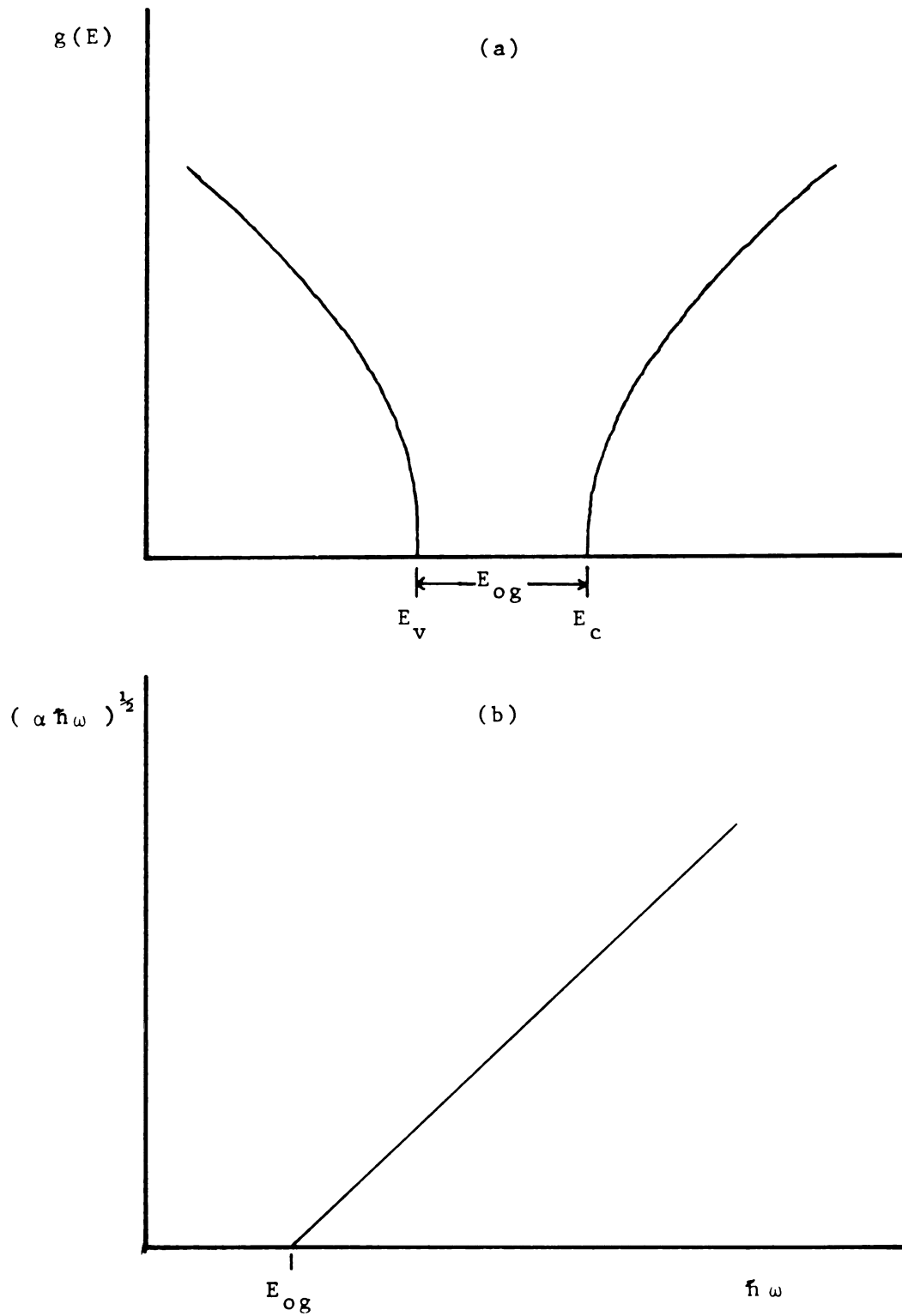


Figure 3.8 Optical energy gap for a crystalline semiconductor.  
 (a) Density of states  
 (b)  $(\alpha \hbar \omega)^{1/2}$  vs  $\hbar \omega$

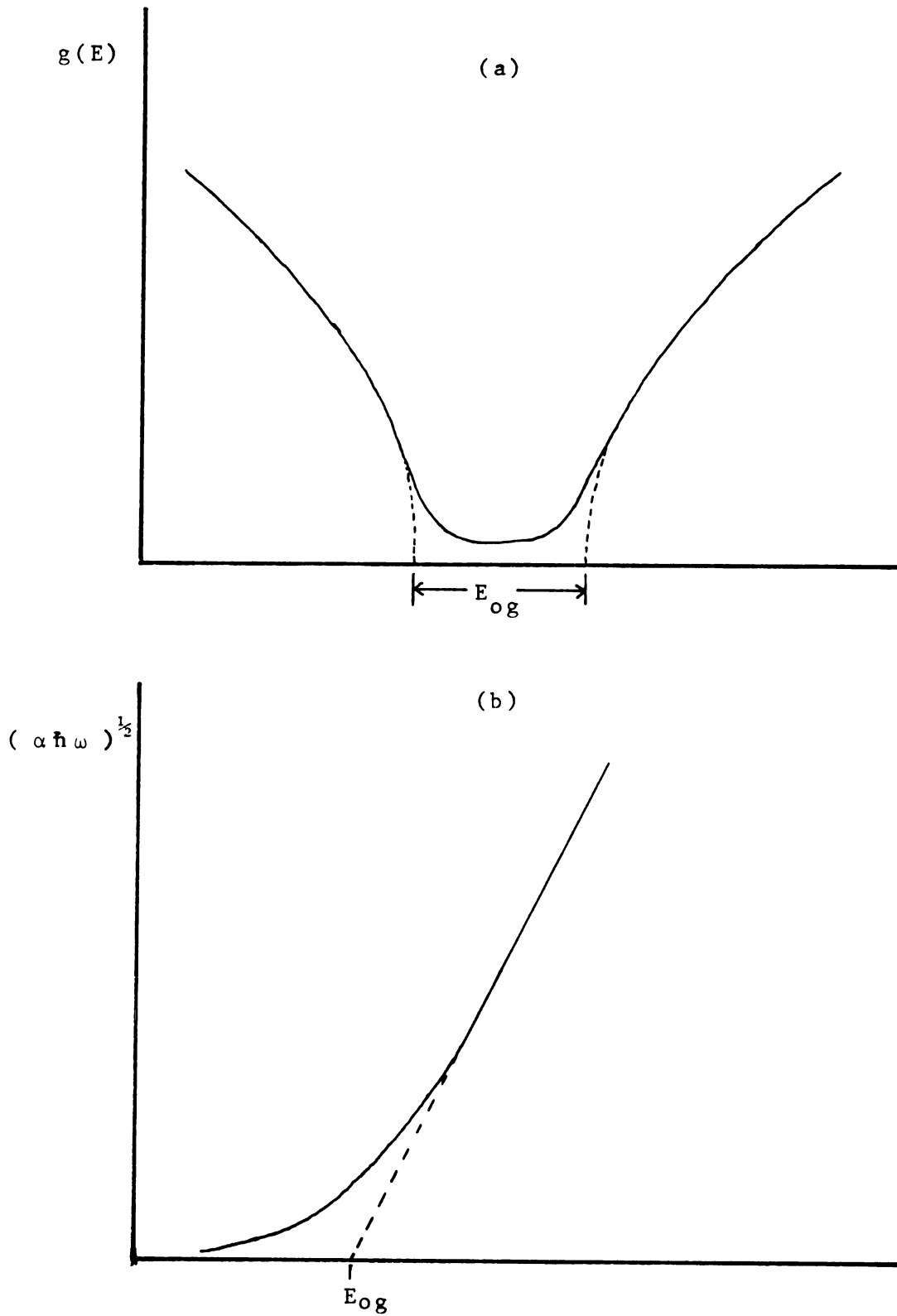


Figure 3.9 Optical energy gap for an amorphous semiconductor.  
 (a) Density of states  
 (b)  $(\alpha \hbar \omega)^{1/2}$  vs  $\hbar \omega$

### 3.3.4 Gold transmission measurement

Knowledge of the transmission characteristics of the gold films deposited to form Schottky barrier devices is essential to determination of the amount and spectral distribution of light actually reaching the semiconductor. Gold transmission samples are obtained for the Schottky barrier evaporations by placing an uncoated glass substrate adjacent to the amorphous silicon sample on which devices are being fabricated. In general, the reflectance,  $R$ , and transmittance,  $T$ , of the gold film depend on the optical properties of the substrate. A substantially higher reflectance is observed in films deposited on silicon. Assuming the optical properties of the gold deposited on the silicon and the glass are identical and using known optical constants for gold films,<sup>63</sup> the amount of light transmitted into the silicon as compared to the amount of light transmitted into the glass may be computed. See Appendix D for details of the calculation.

To determine the amount of light entering the film,  $T$  is measured for the gold film on glass. This number is then multiplied by a factor (which depends on  $T$ ) to determine the amount of light entering the silicon. For certain films, for which only the reflectance,  $R$ , of the gold deposited on the silicon is known,  $T$  may again be found by appeal to theory since  $R$  and

T are both functions of thickness. The measured R yields a thickness from which T may be calculated.

The transmission information is used in comparison of Schottky barrier samples which, due to unavoidable run to run variations in gold thickness, "see" different fractions of the incident light. A wavelength of 550 nm is chosen for comparison of gold transmittance since the spectral response of the Schottky barrier, the transmittance of the gold film and the incident intensity are all large at this wavelength, giving a representative comparison.

### 3.3.5 Hydrogen content

The hydrogen content vs depth was profiled for one sample deposited at 0 V bias, with the deposition parameters at their standard values for the small target, by the  $^1\text{H}(^{15}\text{N}, \alpha\gamma)^{12}\text{C}$  resonant nuclear reaction method.<sup>68,69</sup> This method is claimed to be the most accurate method available for depth profiling of hydrogen content.<sup>13</sup> The amount of hydrogen in the film is determined by measuring the intensity of the characteristic gamma rays emitted in the reaction. Good depth resolution is possible due to the fact that the nitrogen nucleus loses energy at a known rate in silicon and the reaction takes place only over a narrow range in energies. The hydrogen content at different depths is probed by varying the incident energy of

the  $^{15}\text{N}$  ions. Calibration is achieved through comparison with a standard, a crystalline silicon wafer implanted with a known dose of hydrogen. Accuracy is estimated to be better than  $\pm 10\%$  of the measured value. Several points remeasured after profiling the entire film showed no change in measured hydrogen concentration, indicating insignificant loss or mobility of hydrogen under irradiation.

The hydrogen content in the film generally ranged between 18 and 24 percent with an irregular dependence on depth. See Figure 3.10. At the time the profiled film was deposited, the rf source was quite unstable causing sudden power variations of 30% lasting for minutes to tens of minutes, possibly causing different amounts of hydrogen to be incorporated.<sup>70</sup> This is the probable cause of the irregular dependence on depth. For films whose properties are reported in chapters 4 and 5, the rf power was stable. The average hydrogen content of the film is similar to that of material produced under similar conditions.<sup>68,64</sup> (The hydrogen was profiled by A. M. Hernandez, J. N. McGruer, R. J. Irwin, N. J. Doyle and J. A. Rabel at the University of Pittsburgh, work supported in part by NSF Grant #DMR 81-02968.)

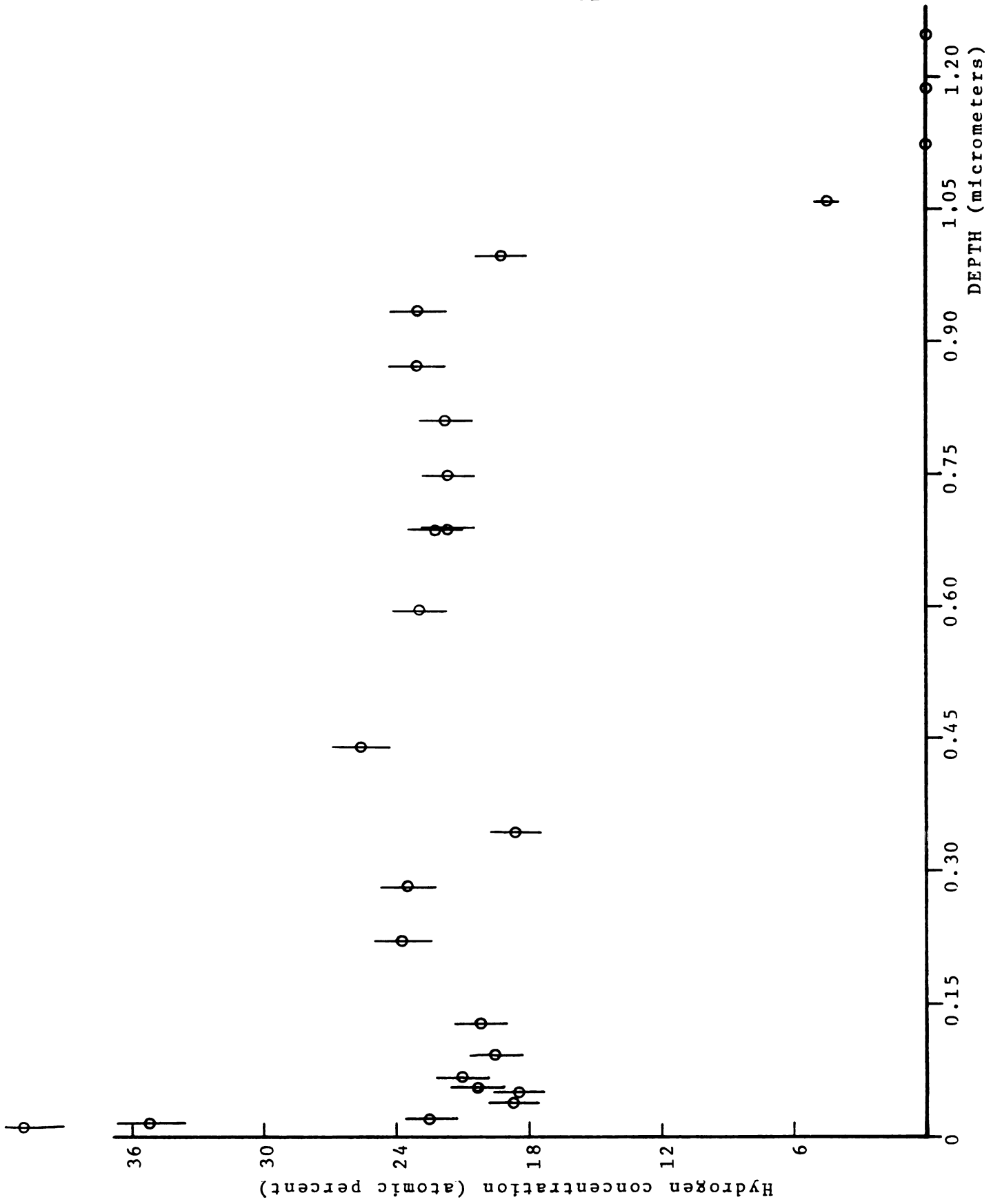


Figure 3.10 Hydrogen content vs depth.

$\phi$

### 3.3.6 Conductivity vs Temperature

Conduction mechanisms in the material are studied by examining the conductivity of the sample as a function of temperature. Most of the conductivity vs. temperature data is from coplanar samples which consist of a layer of amorphous silicon deposited on Corning 7059 glass with aluminum contacts evaporated on the top surface. To determine the conductivity, the resistance of the sample is measured and the conductivity is calculated from the geometry.

$$\sigma = \frac{R \text{ Th} W}{L}$$

$\sigma$  = conductivity  $\sim 10^{-4} - 10^{-11} \Omega\text{-cm}$   
 $R$  = resistance  $\sim 10^7 - 10^{13} \Omega$   
 $\text{Th}$  = thickness  $\sim 7 \times 10^{-5} \text{ cm}$   
 $W$  = width  $\sim 1.3 \text{ cm}$   
 $L$  = length  $\sim 4.6 \times 10^{-2} \text{ cm}$

Conductivity samples were also constructed in a sandwich geometry with top and bottom metallic contacts for confirmation of the coplanar measurements. In this second case the resistances and consequently measurement voltages used are much lower and producing the desired ohmic contacts turns out to be a major problem.

The measurements on all samples are made with the sample enclosed in an argon filled aluminum testing box. The box is sufficiently massive to provide a

constant temperature environment, being  $3\frac{1}{2}$  inches square with  $\frac{3}{4}$ ,  $\frac{1}{2}$  and  $\frac{3}{8}$  inch thick base, sides and top, respectively. The flow of argon is kept to a rate well below that which causes observable cooling of the sample. Heat is applied to the box by a resistance heater controlled by a Micro Technical Industries Thermo-Probe which also measures the temperature of the testing box to a stated accuracy of  $\pm .5^{\circ}\text{C}$  via a thermocouple embedded in the base. The heating and cooling rates are kept sufficiently low ( $\sim 3^{\circ}\text{C}/\text{minute}$ ) that no hysteresis is observed as the sample is heated then cooled.

The resistance of the sample is measured to an accuracy of  $\pm 5$  or  $\pm 3\%$  of full scale, giving an accuracy of  $\pm 3$  to  $\pm 15\%$  for individual values, depending on the part of the scale used and the resistance value. Resistances of the coplanar samples are measured with applied voltages of 9-90 volts to eliminate contact effects. At these voltages the I-V characteristics of the devices appear completely linear. Measurement of the characteristics of similar contacts in the sandwich geometry indicate that at the current levels of the test, the contact voltage is entirely negligible.

The I-V characteristics of the sandwich samples are generally extremely non-linear indicating barrier and/or injection effects. Resistance measurements

are made at very low voltages, typically less than .05V, such that the measured resistance is independent of voltage. Results of these measurements will be discussed in Chapter 4.

If the conductivity is of the form

$$\sigma = \sigma_0 e^{-E_A/kT}$$

a plot of  $\sigma$  vs  $10^3/T$  will yield a straight line characterized by the quantities  $\sigma_0$  and  $E_A$ . In general this relation holds for the coplanar samples and  $\sigma_0$  and  $E_A$  are determined by a least squares fit to the plot of  $\log \sigma$  vs  $10^3/T$ . For a substantial number of samples the lowest temperature points do not fall on the line and are not included in the least squares fit. See Fig. 3.11.

In addition to the inaccuracies described in measuring the resistance, additional error enters through uncertainties in geometry.  $W$  and  $L$  are known quite accurately (~3%) through simple measurements under a microscope equipped with a reticle. In any case, since the same part of the mask is used for all measured devices the error is fixed. Although the thickness is known to a 4% accuracy at any given point, it varies by about 10% over the area of the sample. The measurement is done at what is thought to be a representative point, but the actual thickness is uncertain to about

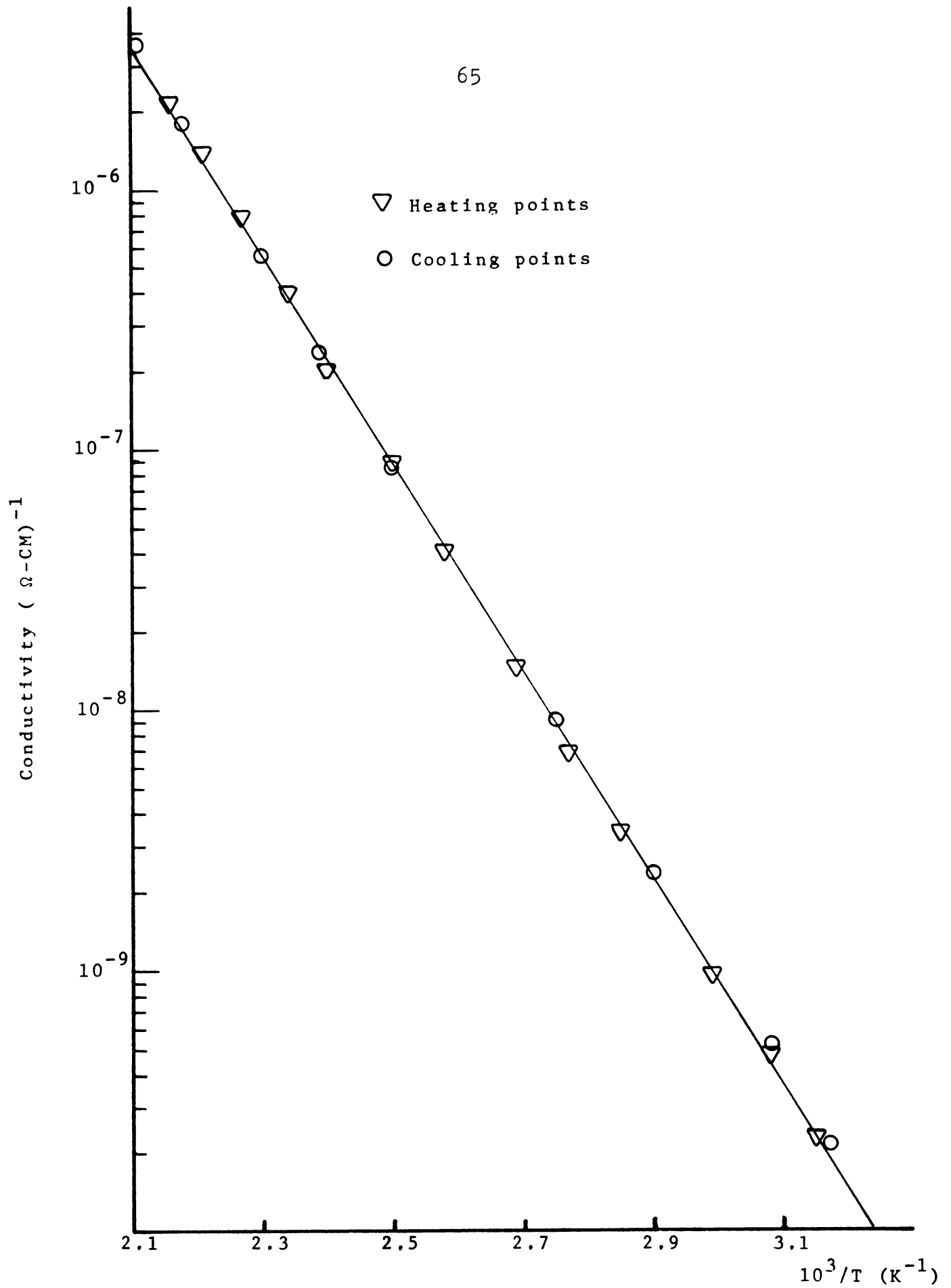


Figure 3.11 Conductivity vs 10<sup>3</sup>/T (ND-61).

5%. The error in W and L will change  $\sigma$  by a constant factor, leading to an uncertainty in  $\sigma$  of 11% in an absolute sense or 5% from sample to sample.  $E_A$  is completely insensitive to geometry. Five percent errors in resistance, could, if incorrect in opposite directions for high and low resistances cause errors in  $E_A$  and  $\sigma_0$  of approximately  $\pm 1\%$  and  $\pm 25\%$  respectively, much larger in  $\sigma_0$  since  $\sigma$  is proportional to  $e^{-E_A}$ .

### 3.3.7 Photoconductivity, $\mu\tau$ product

Another measure used to characterize the films produced at different biases is the photoconductivity, or in a more exact sense, the mobility-lifetime ( $\mu\tau$ ) product. In the experiment, the sample is illuminated and the photoconductivity defined by the difference between the light and dark

$$\sigma_{ph} = \sigma_l - \sigma_d$$

conductivities, that is the conductivity induced by the absorption of photons and consequent generation of free carriers. The  $\mu\tau$  product is found by relating the measured photoconductivity to  $\mu\tau$ . First,

$$\sigma_{ph} = q\mu_t\Delta n$$

$q$  = electronic charge

$\mu_t$  = trap limited drift mobility

$\Delta n$  = density of photo-generated electrons

since the mobility of photogenerated holes in amorphous silicon is extremely small due to the presence of deep hole traps.<sup>13</sup> The number of photogenerated electrons is equal to the generation rate times the average recombination lifetime.

$$\Delta n = G\tau_r$$

and

$$\sigma_{ph} = q\mu_t G\tau_r$$

Ideally each absorbed photon would generate a hole electron pair, and evidence for and against this being the case for amorphous silicon exists.<sup>43,71,72</sup>

Assuming an efficiency of generation of hole-electron pairs for absorbed photons of  $\eta$ ,

$$G = \eta A$$

where  $A$  is the number of photons absorbed per  $\text{cm}^3$  sec. Combining the above equations, the efficiency mobility lifetime product is given by

$$\eta\mu_t\tau_r = \frac{\sigma_{ph}}{qA}$$

For the samples tested in this research  $A$  is determined by measuring the intensity of light falling on the sample and the fraction of that light which is absorbed. The average value of  $A$  over the thickness of the sample is then given by

$$A = \frac{I(1-R-T)}{Th}$$

I = intensity, photons/sec-cm<sup>2</sup>  
 Th = thickness  
 R = reflectance  
 T = transmittance

The factor (1-R-T) is the fraction of incident light absorbed by the sample. Diffusion to and recombination at the surface is neglected in this treatment, since  $\mu\tau$  is used primarily in sample to sample comparison and the magnitude of the diffusion losses is unknown and likely to be small due to the short diffusion length of holes and thus the short ambipolar diffusion length.<sup>73,74,13</sup>

Experimentally, the conductivity with and without light is measured in much the same way as the dark conductivity, with the sample mounted in the testing box and its resistivity measured with the Keithly electrometer. The top of the box is removed to provide optical access. Relatively weakly absorbed 650 nm light is supplied by the monochromator to provide illumination uniform to within  $\pm 30\%$  over the thickness of the sample. See Figure 3.12.

R and T are measured as described earlier. The incident intensity is measured with the silicon detector, which has in turn been calibrated at 645 and 680 nm using an Epply model 8-48 radiometer as follows. Light

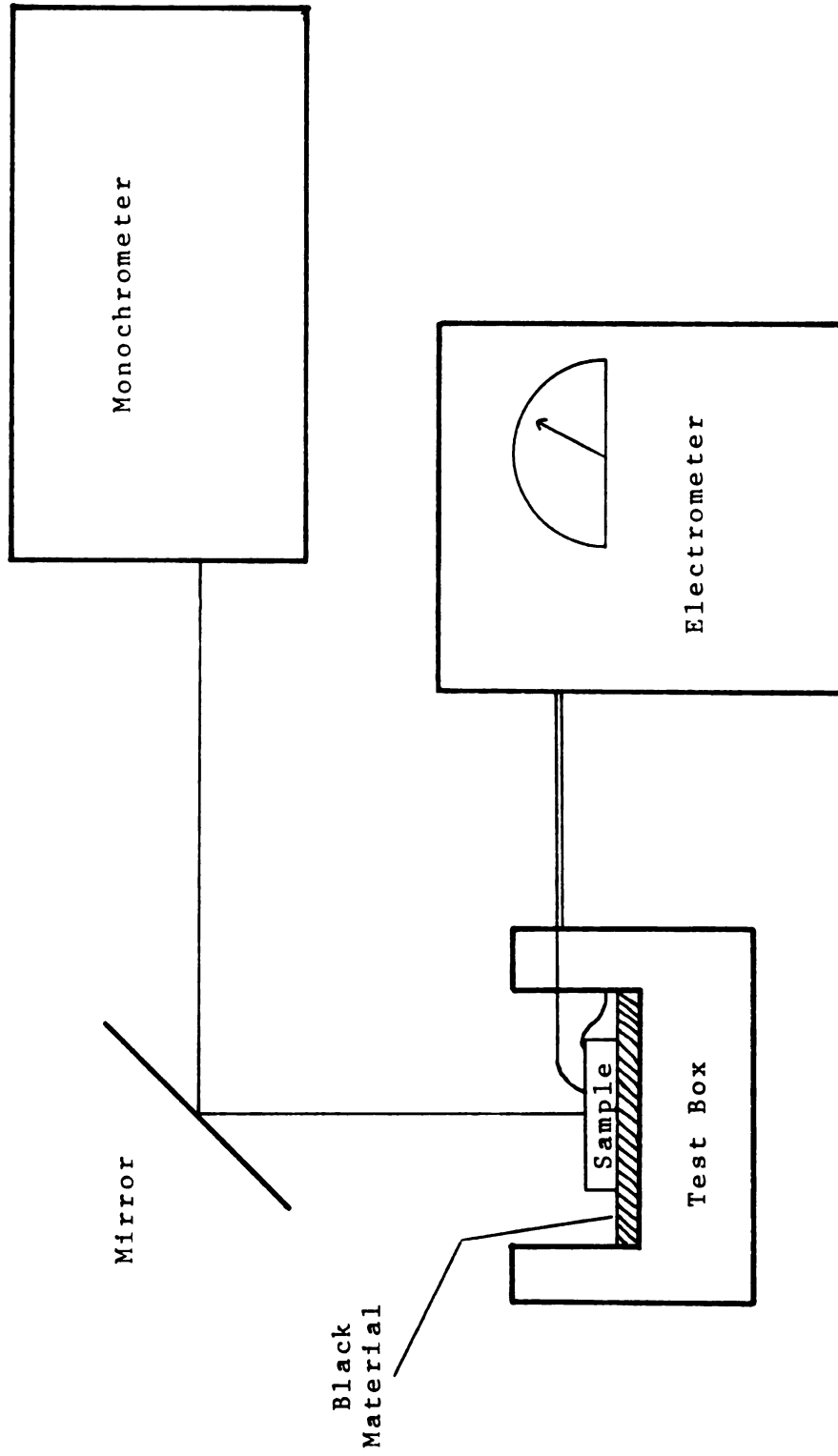


Figure 3.12 Photoconductivity measurement .

from a tungsten source is passed through a monopass filter (described earlier) and focused to a nearly uniform intensity spot slightly larger than the active surface of the radiometer. After the intensity as measured by the radiometer is recorded the intensity is reduced by a calibrated filter ( $\pm 2\%$ ) to a value within the range of the silicon cell. The output of the silicon cell is then recorded and the calibration factor calculated. The overall accuracy of this procedure is estimated as  $\pm 10\%$ . The error in determining  $\mu\tau$  is a combination of this error, the uncertainty in R and T and the measurement errors in determining the conductivity and incident intensity. Therefore the total uncertainty may be as high as 25%, although 10% of this is due to calibration of the silicon cell and does not affect sample to sample comparison of  $\mu\tau$  products.

The  $\mu\tau$  product is also measured as a function of intensity by inserting calibrated neutral density filters in the light path before it enters the monochrometer. Since the intensity in the  $\mu\tau$  tests was not held constant from sample to sample due to variations in incident intensity and film reflectivity, approximately an additional  $\pm 15\%$  uncertainty is introduced.

### 3.3.8 Schottky Barrier Characterization

During the course of this study a number of Schottky barrier devices were constructed, first to evaluate the quality of material produced here at Michigan State University and second to study the dependence of diode and solar cell properties on substrate bias and film thickness. This section describes briefly the measurements used to characterize the devices.

One important and relatively straightforward measurement is the determination of the current voltage (I-V) characteristic of the diode. The simplest measurement is made at room temperature, again in the aluminum testing box for shielding and to enclose an argon atmosphere if desired. In practice the I-V characteristics are identical in argon or dry air. A voltage is established by a regulated dc power supply and measured to a .5% accuracy with a digital multimeter. The resultant current is measured with a Keithly 610B electrometer to a 5% accuracy. Any voltage drop across the electrometer is subtracted from the voltage reading. See Figure 3.13.

For measurement of high current points where heating is a problem, the voltage source is replaced by a pulse generator, the voltmeter by an oscilloscope and the ammeter by a resistor whose voltage is

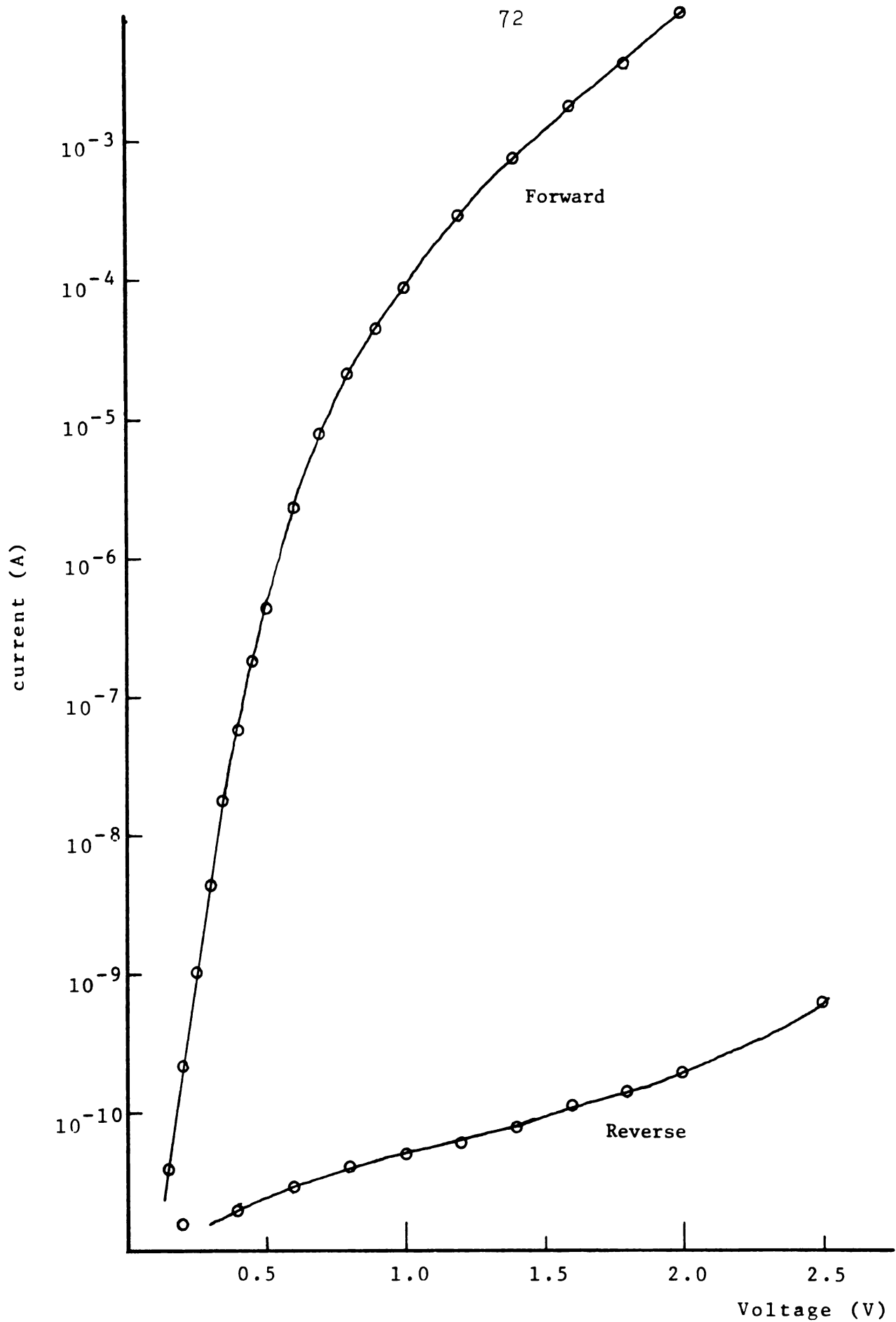


Figure 3.13 ND-11 Dark I-V characteristics.

monitored on an oscilloscope. The high current measurement limit of this set-up is reached when heating, as evidenced by an increasing current with time, is observed before the diode current reaches an equilibrium value.

Several numbers useful in comparison of devices are derived from the I-V data. The rectification ratio is simply the ratio of the forward to reverse current at a specified voltage. The I-V characteristic at small currents is very nearly exponential and so the parameters of the ideal diode equation are convenient for comparison purposes.

$$I = I_0 (e^{nqv/kT} - 1)$$

$I_0$  is the extrapolated zero voltage intercept of the linear part of the log I vs V plot. The quality factor,  $n$ , is the inverse of the slope of the straight segment.  $I_0$  may be determined within  $\pm 10\%$  and  $n$ , in the exponential, within about  $\pm 2\%$ .

The photovoltaic properties of the device are examined through measurement of the current-voltage characteristic under illumination. The open circuit voltage,  $V_{oc}$ , short circuit current,  $I_{sc}$ , efficiency  $\eta$ , and the fill factor, FF, are all used for device to device comparison in conjunction with the gold transmittance information described earlier. See

Figure 3.14.

The barrier height is derived from an activation energy measurement of the forward current at a given voltage. Additional discussion of the Schottky barrier measurements is included in Chapter 5.

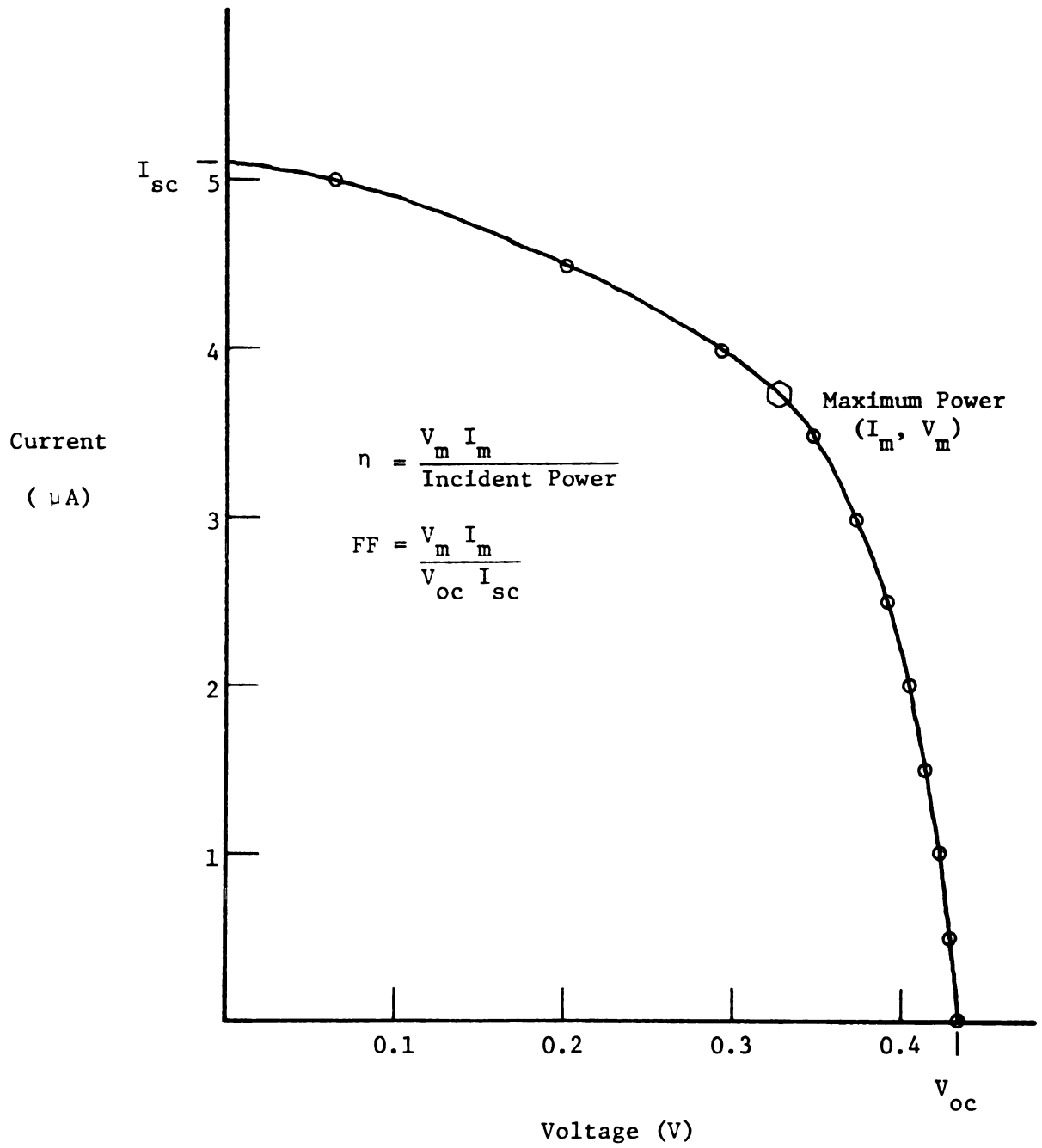


Figure 3.14 Light I-V characteristics.

## CHAPTER IV

### MATERIAL PROPERTIES: SUBSTRATE BIAS EFFECTS

#### 4.1 Introduction

This chapter first discusses preliminary work on the upgraded sputtering system, then presents the results of measurements on the coplanar samples sputtered at different substrate biases and target voltages. Finally these results are interpreted in the context of the current understanding of hydrogenated amorphous silicon.

A considerable investment of time in the laboratory was necessary prior to the preparation and testing of the samples actually used in the investigation of substrate bias and target voltage. First the sputtering system was extensively modified and tested to improve the purity of the sputtering atmosphere. Following this, considerable testing of various films and device structures was necessary to identify a workable experimental design.

The results of the controlled experiments testing the effects of substrate bias and target voltage are first reported along with some relevant background information. At this point the parameters describing electrical

conduction refer to a single conduction path. In the detailed discussion of the results that follows, a two path conductivity model is shown to more accurately describe the electrical conduction in our samples. The first path is a constant of the material, but the second path is directly related to substrate bias.

## 4.2 Preliminary Work and Results

### 4.2.1 Initial Material Evaluation and Device Layout Testing

The first stage of this research involved upgrading and testing the sputtering system. Mark Thompson, who investigated sputtered hydrogenated amorphous silicon at Michigan State University prior to this work, identified the purity of the sputtering atmosphere as an important factor in producing high quality films.<sup>66</sup> To improve the purity of the sputtering atmosphere in this study, gasses 20 times as pure were used and the leak/outgassing rate was improved considerably. The system purity achieved is discussed in Chapter III.

The first several samples constructed verified that the system worked as expected, producing high quality amorphous silicon films as evidenced by the good rectification characteristics of Schottky barrier devices. Following this initial test, a number of

samples (23) were made to evaluate doped films, device structures and substrate biasing as well as a device layout initially proposed to quantify the effects of substrate bias on amorphous silicon. The results of these tests are described briefly below, since they form the basis for the eventual experimental design in this thesis.

After the substrate biasing circuitry was added to the sputtering system 5 molybdenum films were sputtered at various biases to study the thickness uniformity and rate of deposition. The results of multiple beam interferometer thickness measurements are shown in Figure 4.1. The sputtering rate did not change much for a bias of -60 volts, but decreased to  $\frac{1}{2}$  the zero bias rate for a negative bias of 120 volts and to approximately  $\frac{1}{4}$  the zero bias rate at -160 volts. At all bias levels the thickness decreased at distances from the center of more than one centimeter. At the highest bias level net sputtering of the substrate, rather than deposition, occurred in a ring with a diameter of 4 cm. This ring of enhanced sputtering was seen on both the substrate at high biases and on the target and is thought to be an artifact of the shielding at the substrate and target. See Figure 4.2. The target, when not fitted with an overhanging shield, sputtered fastest toward the edge.

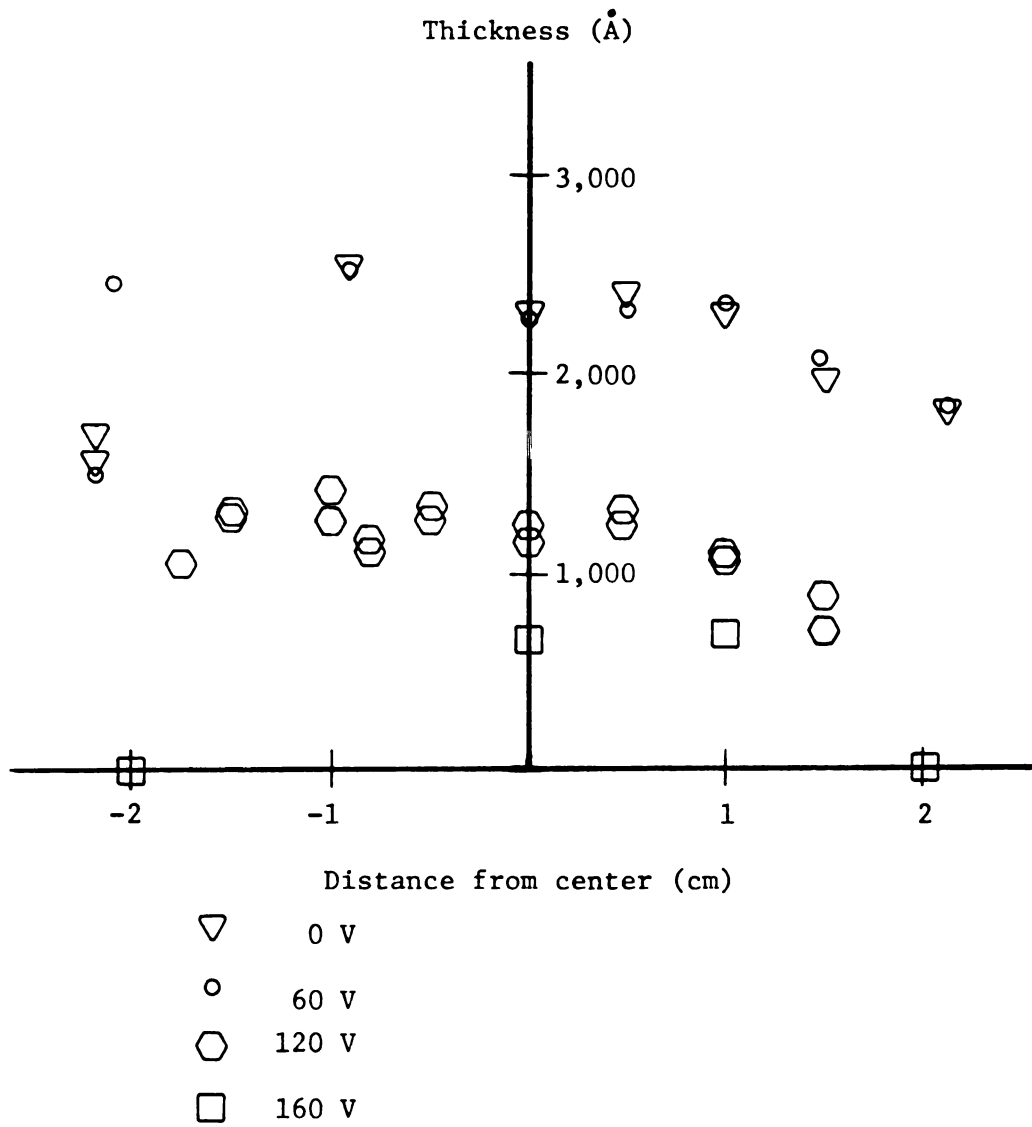
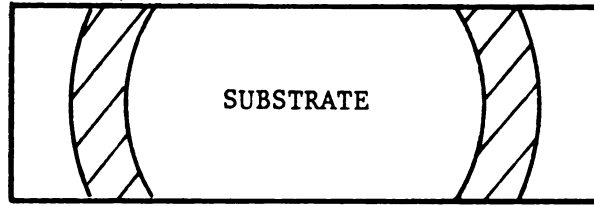
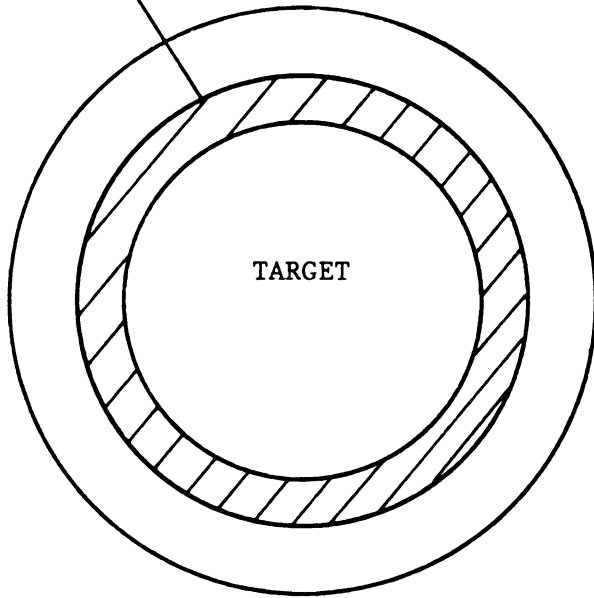


Figure 4.1 Thickness of bias sputtered Mo.

Net Sputtering



Enhanced sputtering



Target profile  
after sputtering

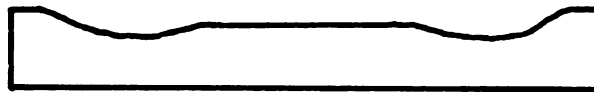


Figure 4.2 Non-uniform sputtering.

Doping of amorphous silicon films sputtered in the Physical Electronics Laboratory became possible with the addition of the 3 channel gas flow system and the acquisition of dopant gasses ( $B_2H_6$  and  $PH_3$ ). Previously, in this laboratory, non-rectifying metal-semiconductor contacts were achieved by sputtering a thin layer of unhydrogenated material adjacent to the metal before deposition of the film, rather than by the more usual method of separating the metal and semiconductor by a thin, heavily doped layer.

Doped films were first studied alone, in various devices structures, then as contact layers at the molybdenum -undoped amorphous silicon interface. The first doped test film, ND-6, was doped with 1500 ppm phosphine in the sputtering atmosphere (7.5 millitorr argon, 0.63 millitorr hydrogen and 0.012 millitorr phosphine). Two device structures were used to investigate how well this material provided ohmic contacts. Gold Schottky barrier devices constructed as described in chapter II showed a rectification ratio of 900 as well as large photovoltages and photocurrents, indicating significant band bending and depletion layer thickness. The molybdenum-n amorphous silicon-molybdenum sandwich devices were non linear at voltages greater than about 0.25 V. The conclusion is that 1500 ppm phosphine is not sufficient to provide reliable ohmic contacts.

The second film, ND-7 was doped more heavily, at 11,000 ppm (7.5 millitorr argon, 0.55 millitorr hydrogen and 0.09 millitorr phosphine). This time the gold Schottky barrier devices showed slight rectification, that is the I-V characteristics were not symmetric, but the observed currents at a given voltage were much higher. Also the photovoltage and photocurrent were too small to be observed. The molybdenum sandwich device was quite linear out to at least 0.5 volts. The slopes at the origin for the molybdenum and gold devices give upper limits on the contact resistances of 4 and  $10 \Omega\text{-cm}^2$  respectively, sufficient for our applications. The I-V characteristics for ND-6 and ND-7 are shown in Figure 4.3. The currents supported by the contacts, even at low voltages, indicate that the ND-7 material is suitable for an interfacial layer to promote good metal-n type amorphous silicon contacts. (Undoped amorphous silicon is slightly n-type.)

Comparison of Schottky barrier I-V characteristics for samples using unhydrogenated and  $n^+$  contact layers demonstrate that the latter is a better contact material, allowing larger forward currents to flow in the device at a given voltage. (Figure 4.4) The resistivity of the bulk material is on the order of  $10^9$  to  $10^{11} \Omega\text{-cm}$  at room temperature, which for

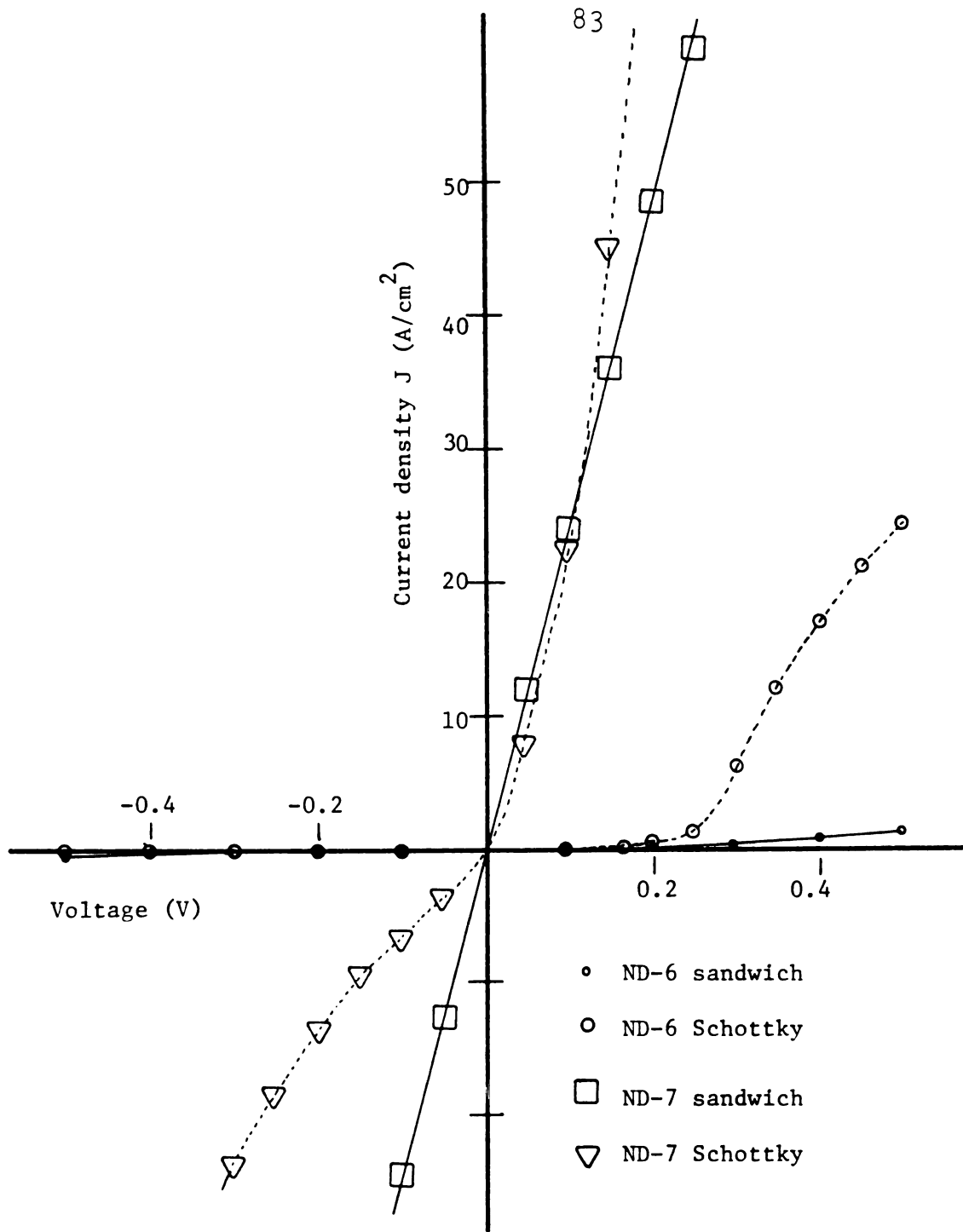


Figure 4.3 ND-6 and ND-7 I-V characteristics .

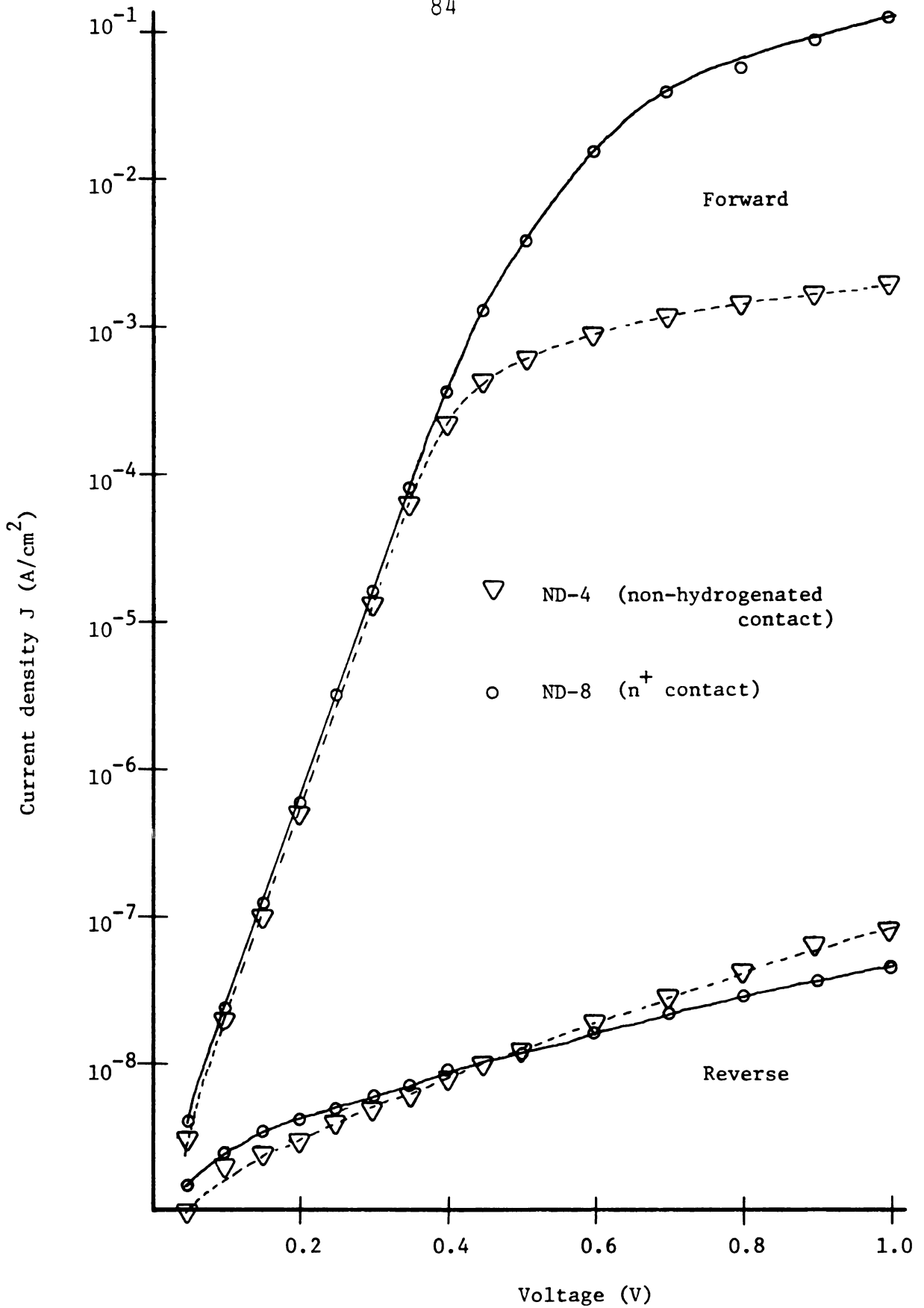


Figure 4.4 I-V characteristics showing improvement with an  $n^+$  contact layer.

a layer 0.2  $\mu\text{m}$  thick gives device resistances of  $10^6$ - $10^8 \Omega$  for our geometry. The observed resistances of the undoped layer in diodes under forward bias conditions are much lower, indicating significant injection, especially in devices constructed with an  $n^+$  contact layer.

The originally proposed device layout consisted of two  $1 \times 0.875$  inch substrates on which coplanar resistance, sandwich resistance, Schottky barrier and optical samples were deposited, all using a common undoped hydrogenated amorphous silicon film. See Figure 4.5. To produce these samples the sequence of events was as follows. Molybdenum was first sputtered onto half of each substrate. The can was opened to change targets and an  $n^+$  layer sputtered over the molybdenum layer, with the other side of the substrate still shielded. Then the undoped amorphous silicon was deposited and the can opened. To produce the devices gold top contacts were evaporated on one sample and molybdenum contacts sputtered on the other.

Several samples yielded the following general results. The Schottky barrier samples were of high quality, not differing in any apparent way from Schottky samples made individually. The molybdenum sandwich samples had very non-linear I-V characteristics, which were often somewhat unstable with respect

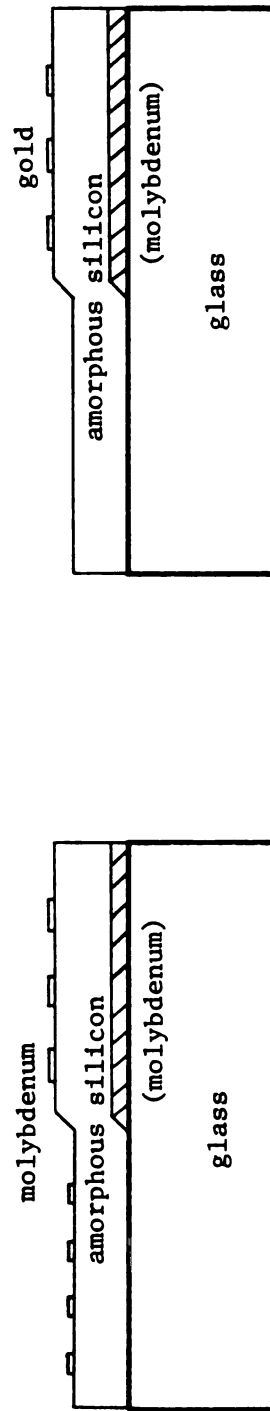
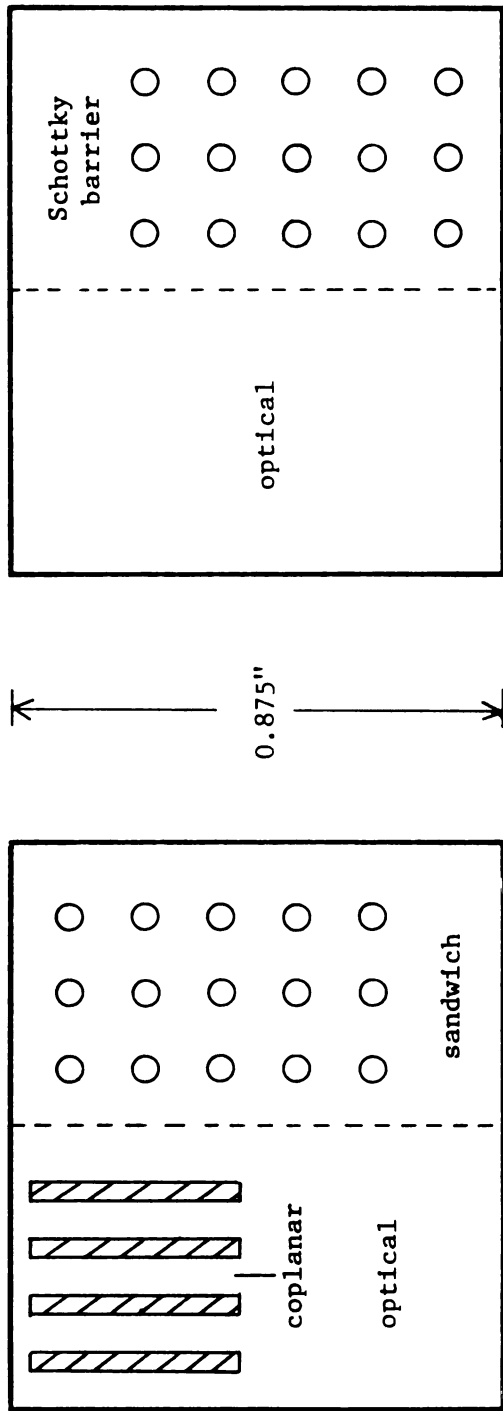


Figure 4.5 Original device layout.

to time and which varied greatly from device to device within a given run. The coplanar samples yielded much higher values for the conductivity,  $\sigma$  than expected and  $\sigma$  varied by factors as large of 1000 from device to device on the same film.

Two conclusions from these observations are that contact effects at the molybdenum undoped silicon interface are important and that masking of the coplanar samples during sputtering of the more conductive  $n^+$  and molybdenum layers is insufficient.

Attempts to improve the masking, as required to produce coplanar samples along with the sandwich and Schottky barrier samples, were unsuccessful. However, coplanar samples sputtered alone and contacted with evaporated aluminum stripes were found to give reasonable and repeatable values for  $\sigma$ .

Since in measurements of the coplanar sample resistance questions of enhanced or reduced conductivity in surface layers arise, it is desirable to compare results from sandwich and coplanar structures. The problem of poor sandwich device contacts was attacked in two ways. First molybdenum- $n^+$ -undoped- $n^+$ -molybdenum structures were fabricated, resulting in characteristics both much more similar from device to device, and much more linear with increasing thickness. See Figure 4.6.

The resistances of these sandwich devices with

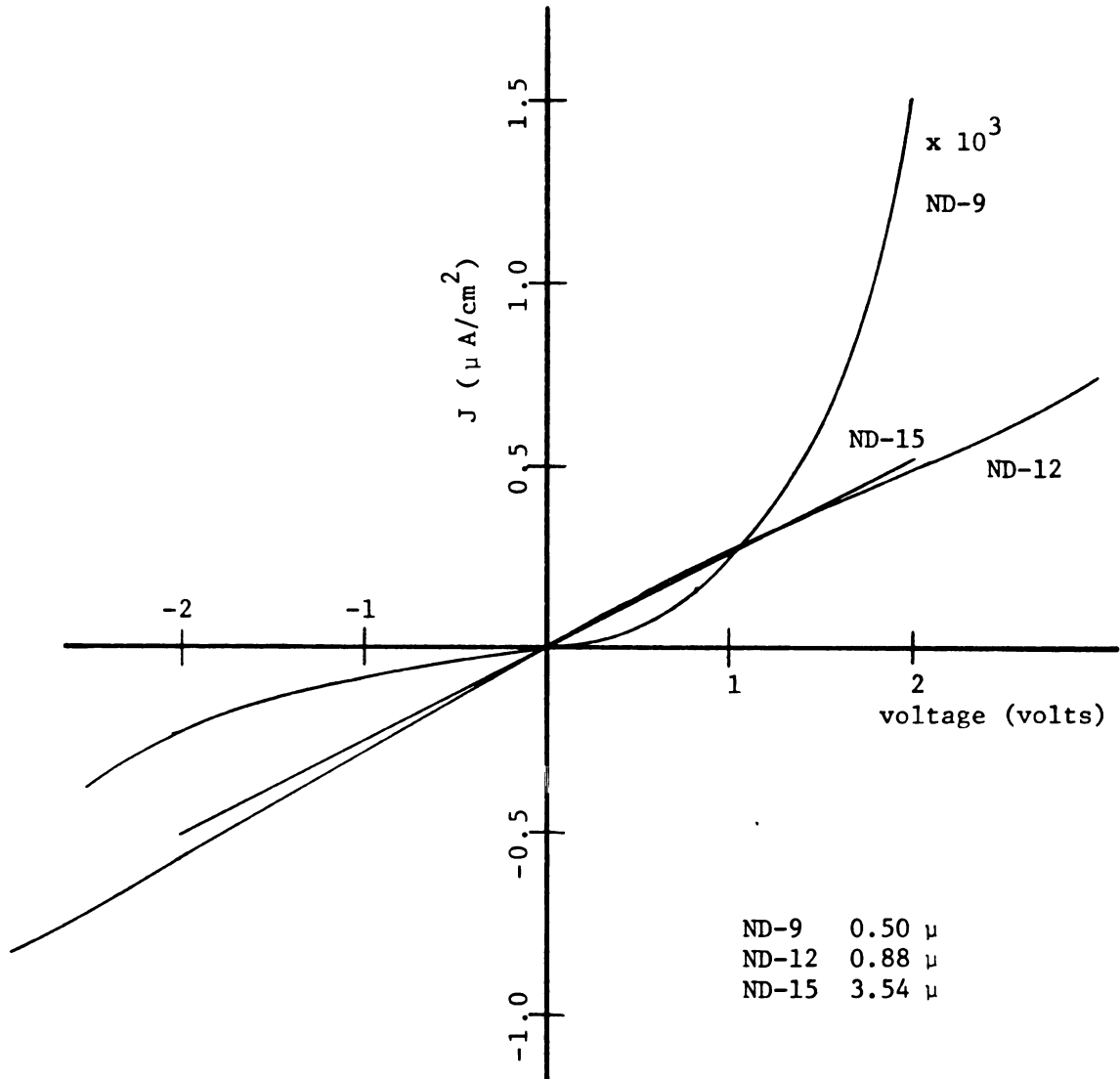


Figure 4.6  $n^+$ -undoped- $n^+$  characteristics.

$n^+$  contacts on both sides are reduced by the high conductivity of the top  $n^+$  layer, however. Evidence for this exists in several forms. First the devices are very light sensitive, even though the molybdenum film is opaque, second the resistivities of devices are decreased by the addition of adjacent conducting stripes on the surface, and third the plot of conductivity vs  $1/T$ , expected to be linear, (and indeed linear for coplanar samples) is seen to curve upward.

All these results are consistent with horizontal conduction in the  $n^+$  layer, which results in conduction through the undoped layer over a larger area than expected. Light sensitivity is expected since the material reached by light now conducts part of the current. A conductor adjacent to the device distributes current over a wider area, reducing the observed resistance and the different temperature dependences of the  $n^+$  and undoped layer result in a non linear plot of  $\sigma$  vs  $1/T$  as shown in Figure 4.7, although each film may individually behave linearly with temperature.

The second approach tried in the attempt to produce useful sandwich samples was to use lower work function metals as contacts to the top of the undoped layer. Aluminum and indium were evaporated through the usual mask. The I-V characteristics of these devices are significantly non-linear for voltages in

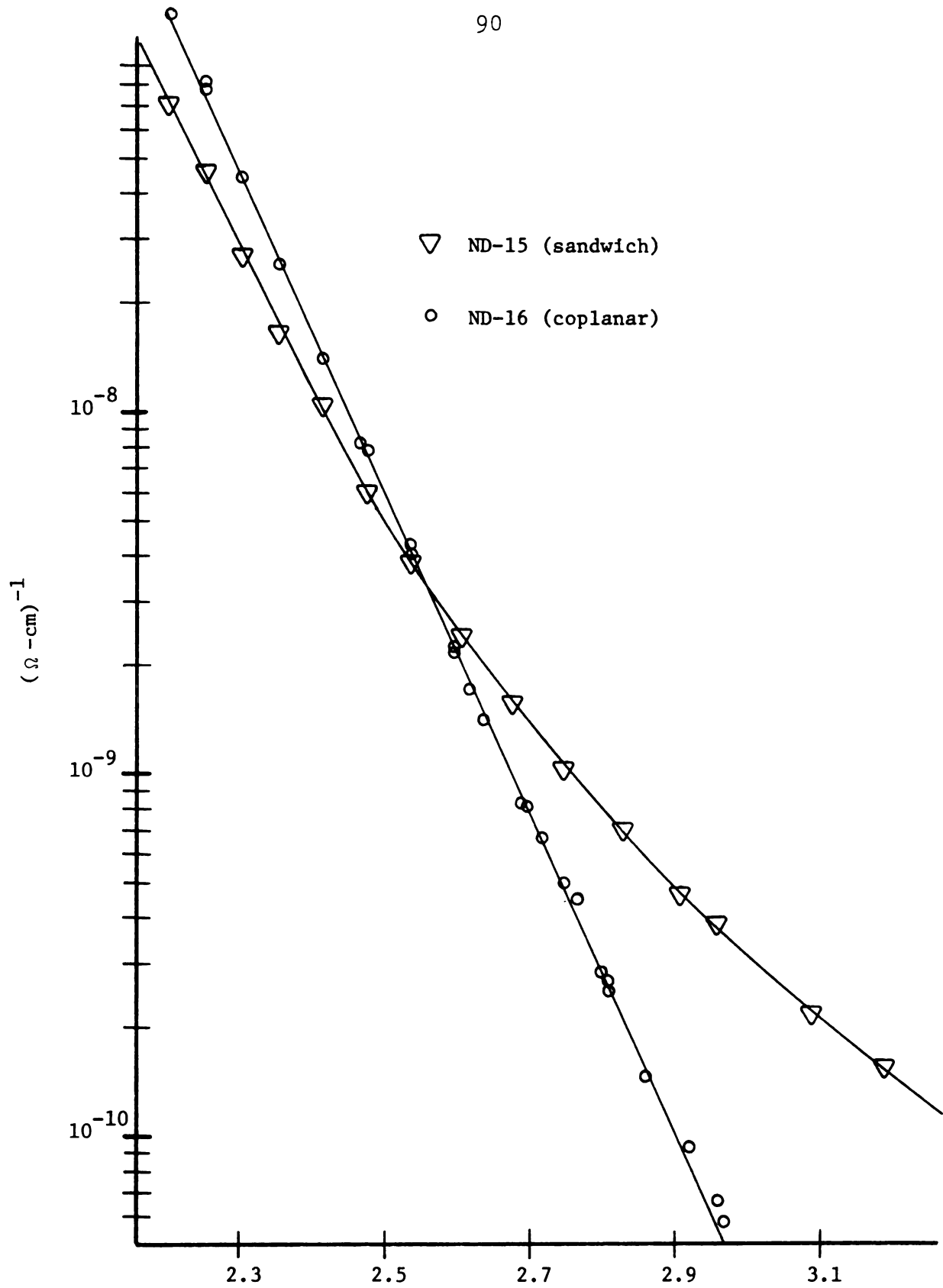


Figure 4.7 Curvature in  $10^3/T$  for  $n^+$ -undoped- $n^+$  sample.

excess of approximately 0.05 volts in contrast to the characteristics of  $n^+$ -undoped- $n^+$ -samples of comparable thickness which are linear to several volts. Again the contact effects appear to be significant.

From these preliminary experiments it is concluded that the types of samples yielding the most reliable data for comparison of films sputtered at different substrate biases are the coplanar and Schottky barrier samples, each type of sample sputtered alone, without critical shielding requirements except during evaporation of the top contacts. The coplanar samples yield bulk material properties while the Schottky barrier samples give a more direct measure of the suitability of the material for diodes and photovoltaics.

#### 4.2.2 Effects of Aluminum Contamination

After the testing just described, a fixed set of parameters was chosen to produce coplanar samples at different substrate biases. The procedure used to produce samples is described in detail in chapter III.

The first two week run resulted in 13 coplanar samples (Device numbers ND-25 through ND-37) with varying properties, the most notable of which were variable and generally large values of the conductivity activation energy,  $E_A$ , and relatively low values of the

conductivity prefactor,  $\sigma_0$ . At the end of the run, when the sputtering chamber was disassembled for cleaning, the probable cause became apparent. The target shield, which prevents the plasma from coming in contact with the aluminum target holder had several small (1 mm) gaps which allowed ions to reach and sputter the target holder. The target holder had several clean shiny areas, characteristic of sputtering, opposite the gaps. A lower prefactor and higher activation energy are both characteristic of amorphous silicon films co-sputtered with small concentrations of aluminum.<sup>66</sup> These films were not used in evaluation of bias effects, and replacement of the target shield led to more reproducible results and the absence of any observable sputtering from the target holder or anything else enclosed by the shield.

### 4.3 Substrate Bias Results

#### 4.3.1 Introduction

Although a significant amount of time during the course of this research was devoted to investigation of other questions, the main motivation and thrust of the work has been toward understanding the effects of substrate bias on the properties of sputtered hydrogenated amorphous silicon.

Bias sputtering attempts to change conditions

at the substrate where the film is growing. Specifically it alters the number and energy of charged particles bombarding the surface of the film. The measurements described previously are used to characterize each film and identify changes in film properties as the bias voltage is varied.

This section presents the results of these measurements. The index of refraction and optical absorption results, which are expected to vary with gross structural changes or large changes in the density of states are presented, followed by the results of measurements of the more sensitive electrical properties. In addition, although this report is primarily on the effects of substrate bias, the effects of a related parameter, target bias, are reported. Target bias and substrate bias both affect substrate bombardment, but in different ways.

#### 4.3.2 Index of Refraction

One film property that is expected to change with gross structural or compositional changes in the film is the index of refraction,  $n$ . In fact, significant variations in  $n$  are seen for changes in certain deposition parameters. A group at Exxon<sup>64,12</sup> reports that the index decreases with either increasing hydrogen or argon pressures in the plasma. They suggest that

the high argon pressure films contain voids that reduce the density.

The results of the present study are all fit, to well within the  $\pm 3\%$  experimental error, by the Wemple-Di Domenico single oscillator dispersion equation with the given values of  $E_o$  and  $E_d$ .

$$n^2(E) = 1 + E_o E_d (E_o^2 - E^2)^{-1}$$

$$E_o = 3.503$$

$$E_d = 32.08$$

This indicates that the index does not change measurably (within 3%) over the whole range of substrate and target voltages examined. Certainly no variation outside experimental scatter is seen as a function of bias. See Figures 4.8 and 4.9. Data in reference 64 indicates that the index varies, as a rough estimate, by  $-.049/\text{atomic percent hydrogen}$  in the film and  $-0.16\%$  void volume. These numbers imply that over the range of substrate bias investigated, the hydrogen content in the film does not vary by more than about 2% and the void volume by more than about 5%, assuming in either case that the index variation is due entirely to one effect or the other.

#### 4.3.3 Optical Energy Gap

The optical energy gap,  $E_{og}$ , as defined for our samples (Chapter III) is an approximate measure of

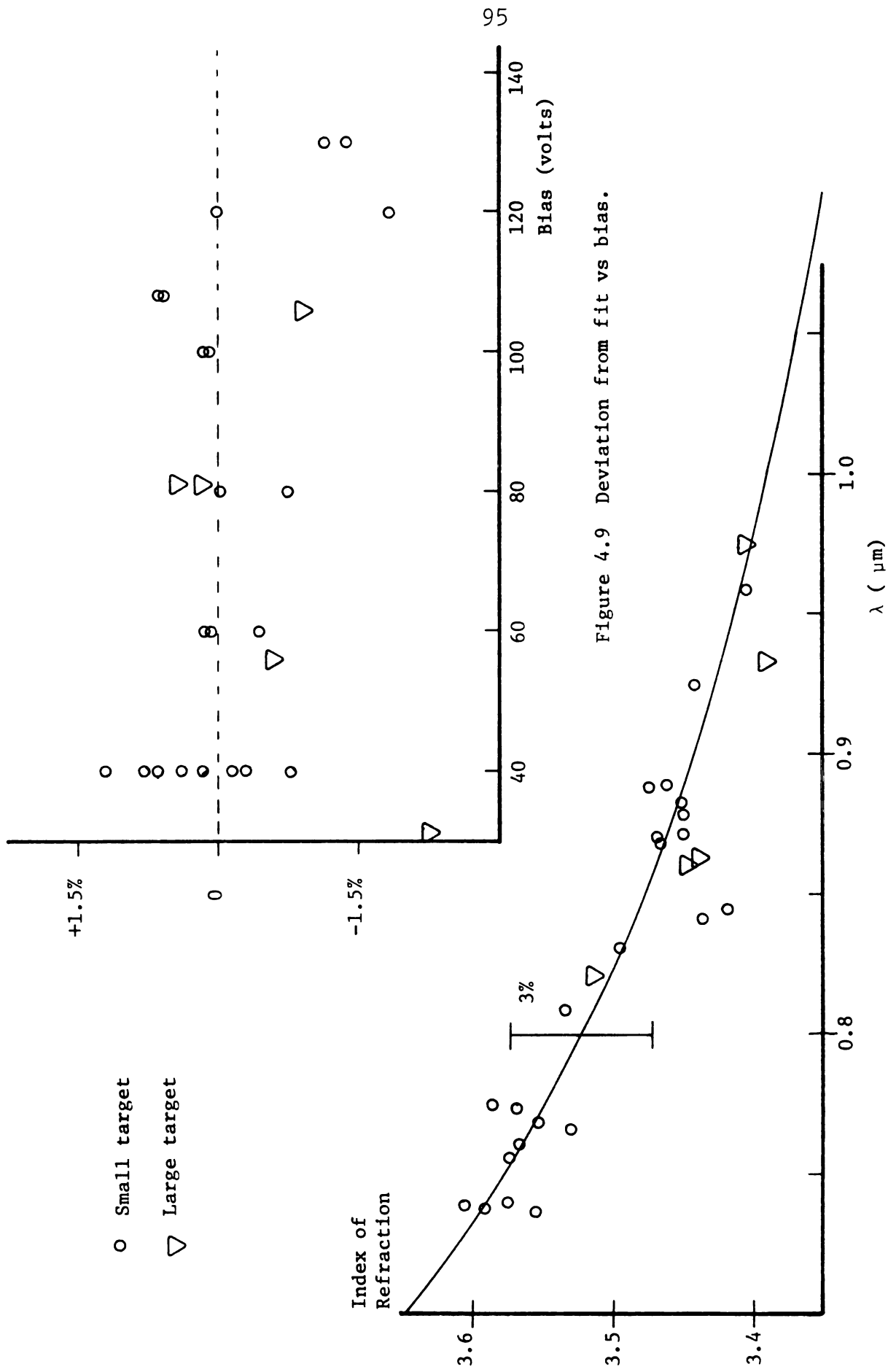


Figure 4.8 Measured index fit to Wemple-Di Domenico equation.

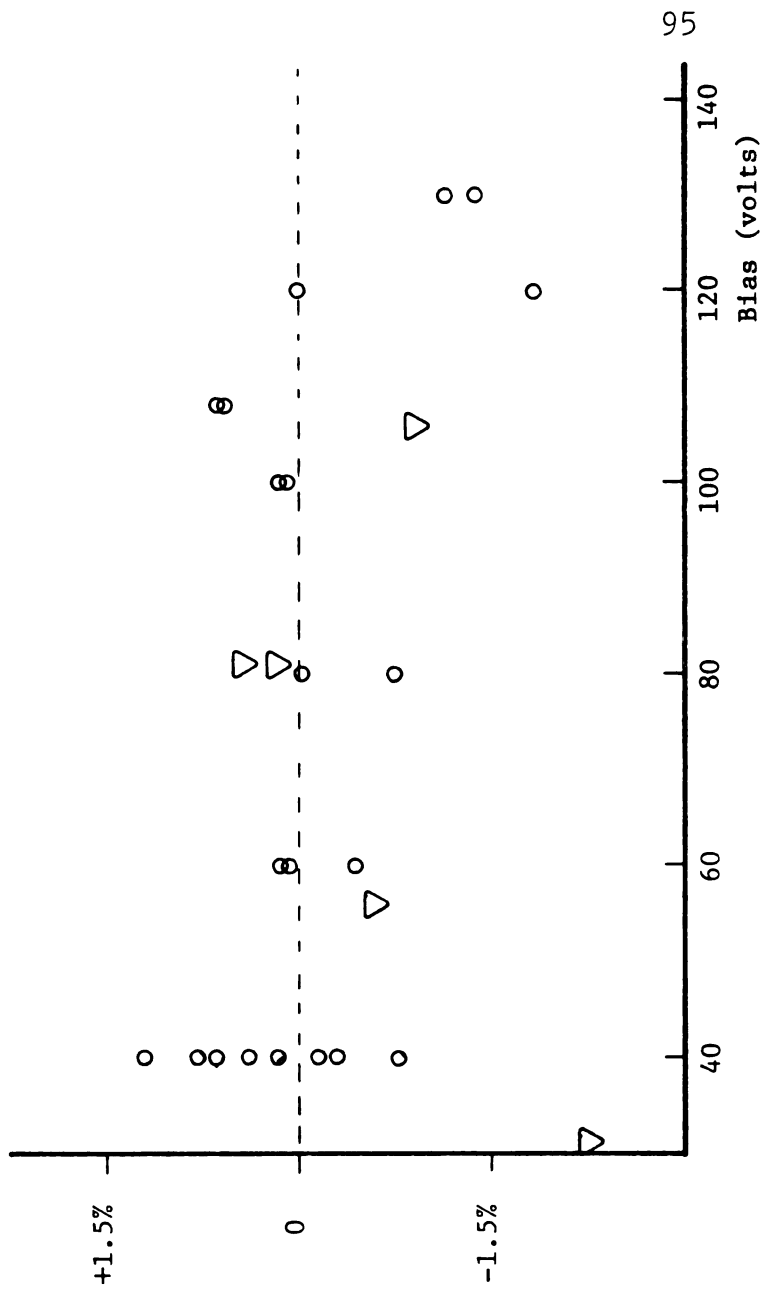


Figure 4.9 Deviation from fit vs bias.

the separation in energy of the conduction and valence bands. Therefore major changes in the density of states at the edges of the bands will show up as a shift in  $E_{og}$ . Again a large body of research has shown that the optical gap varies significantly with deposition parameters such as hydrogen partial pressure, sputtering power and deposition temperature.<sup>12,23,66</sup>

The results are often interpreted in terms of hydrogen incorporation, the hydrogen in the film first reducing the density of states in the gap, then eroding the valence band somewhat as a result of alloying.<sup>12,23</sup>

To within experimental error, as shown in Figure 4.10, the optical gap does not change as a function of a substrate bias. However, a marginally significant increase in the optical gap is seen for samples sputtered using the larger target at a lower target voltage. (Recall that a lower target bias is achieved at the same deposition rate by using a larger target.) The curved, low energy portion of the  $(\alpha\hbar\omega)^{\frac{1}{2}}$  vs  $\hbar\omega$  plot in Figure 4.11 is interpreted as resulting from electrons excited to and from the band tails and as such is a measure of their size. Again, this part of the curve is remarkably similar from sample to sample, a decrease being seen only for samples sputtered using the low voltage target. As shown in Figure 4.12, a film doped by co-sputtering aluminum

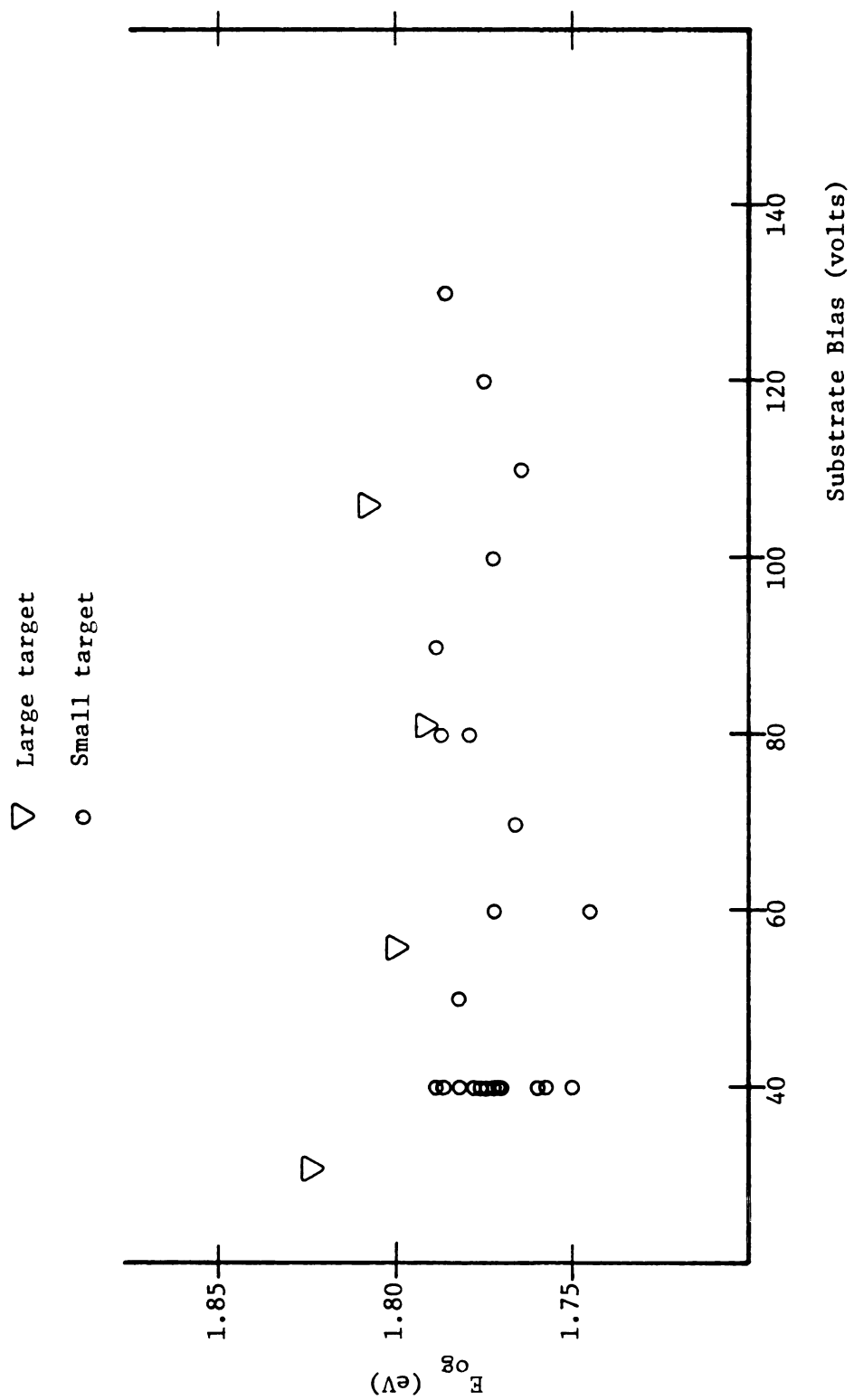


Figure 4.10  $E_{og}$  vs bias.

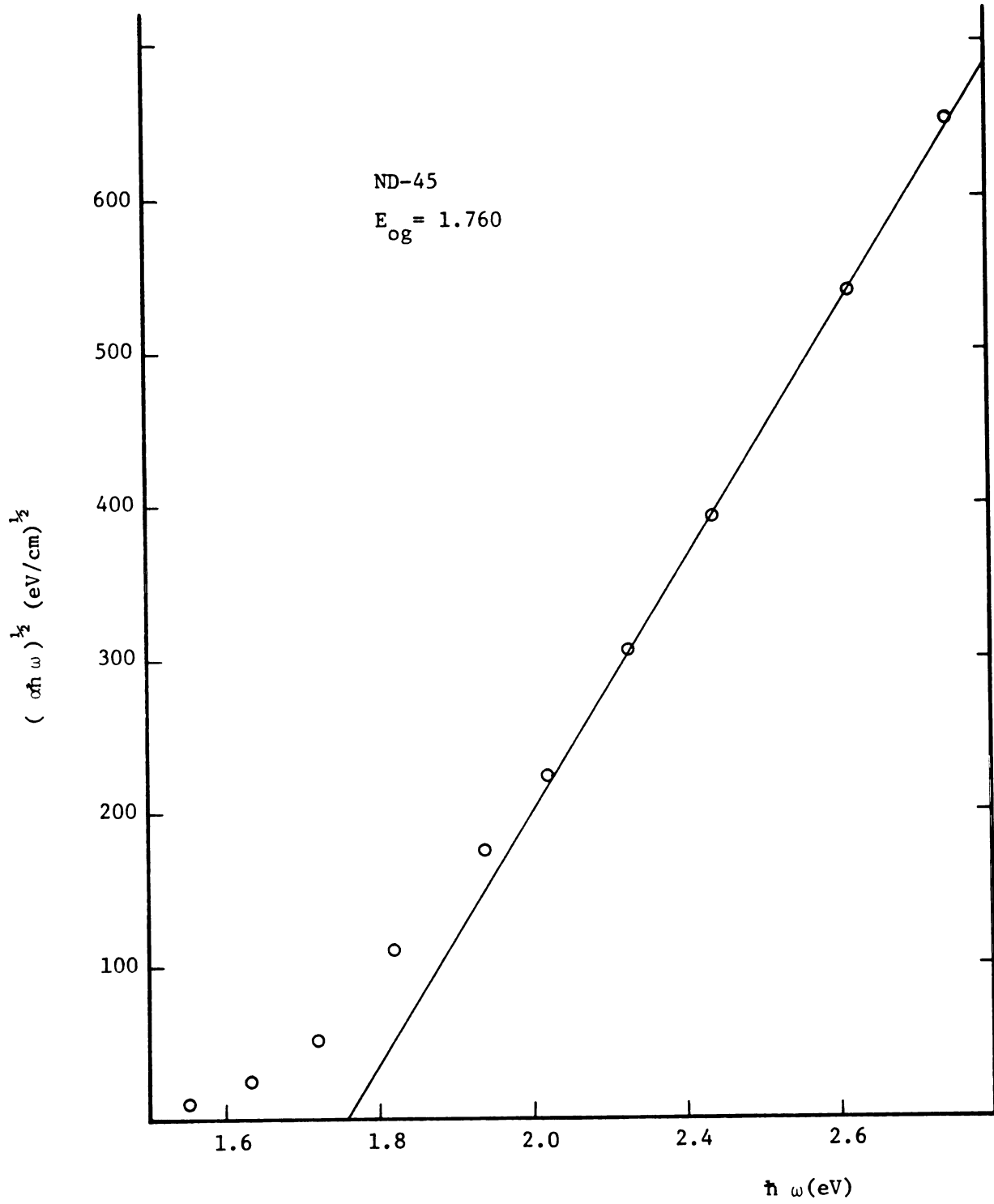


Figure 4.11  $(\alpha \hbar \omega)^{1/2}$  vs  $\hbar \omega$ .

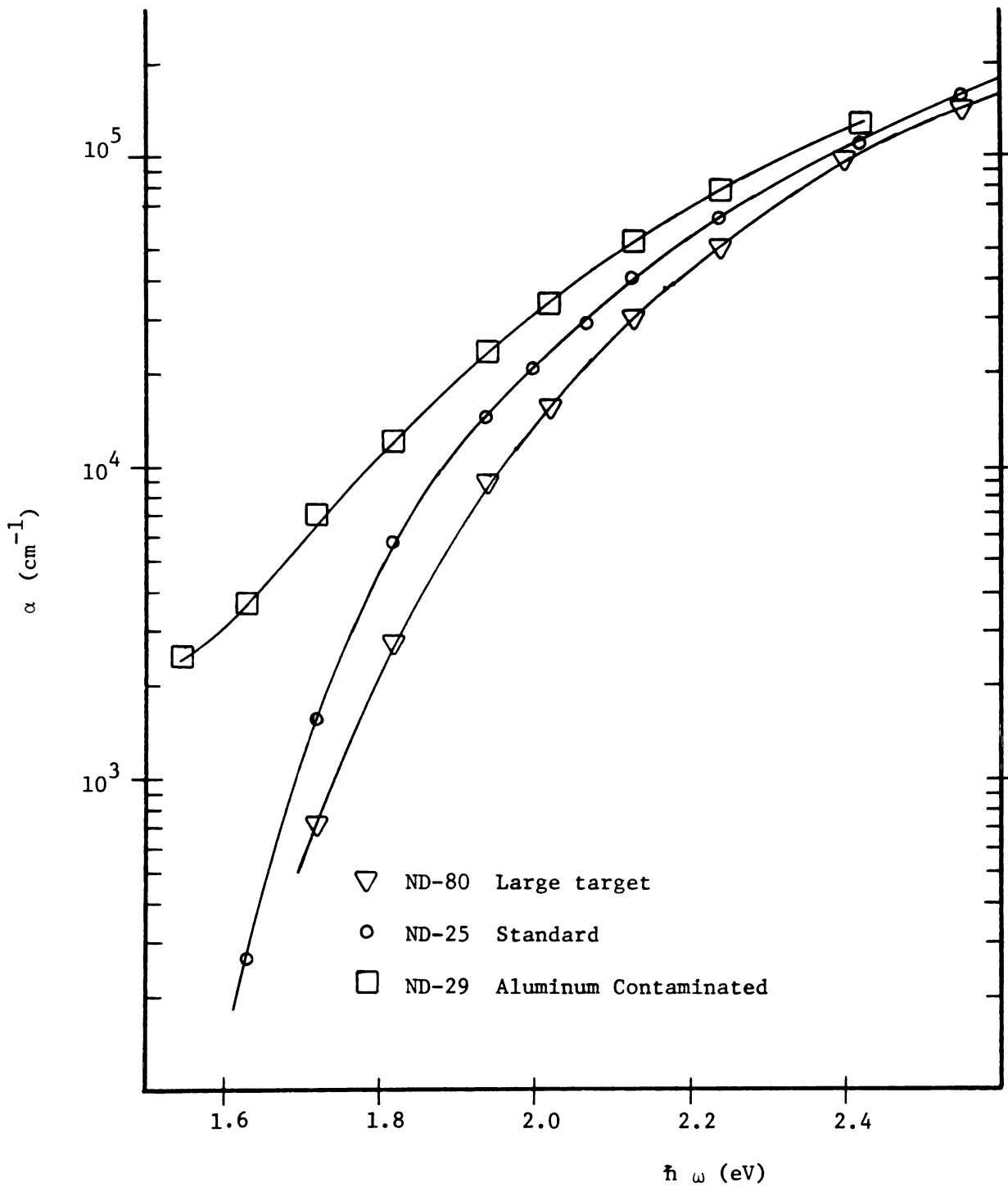


Figure 4.12 Optical absorption coefficient.

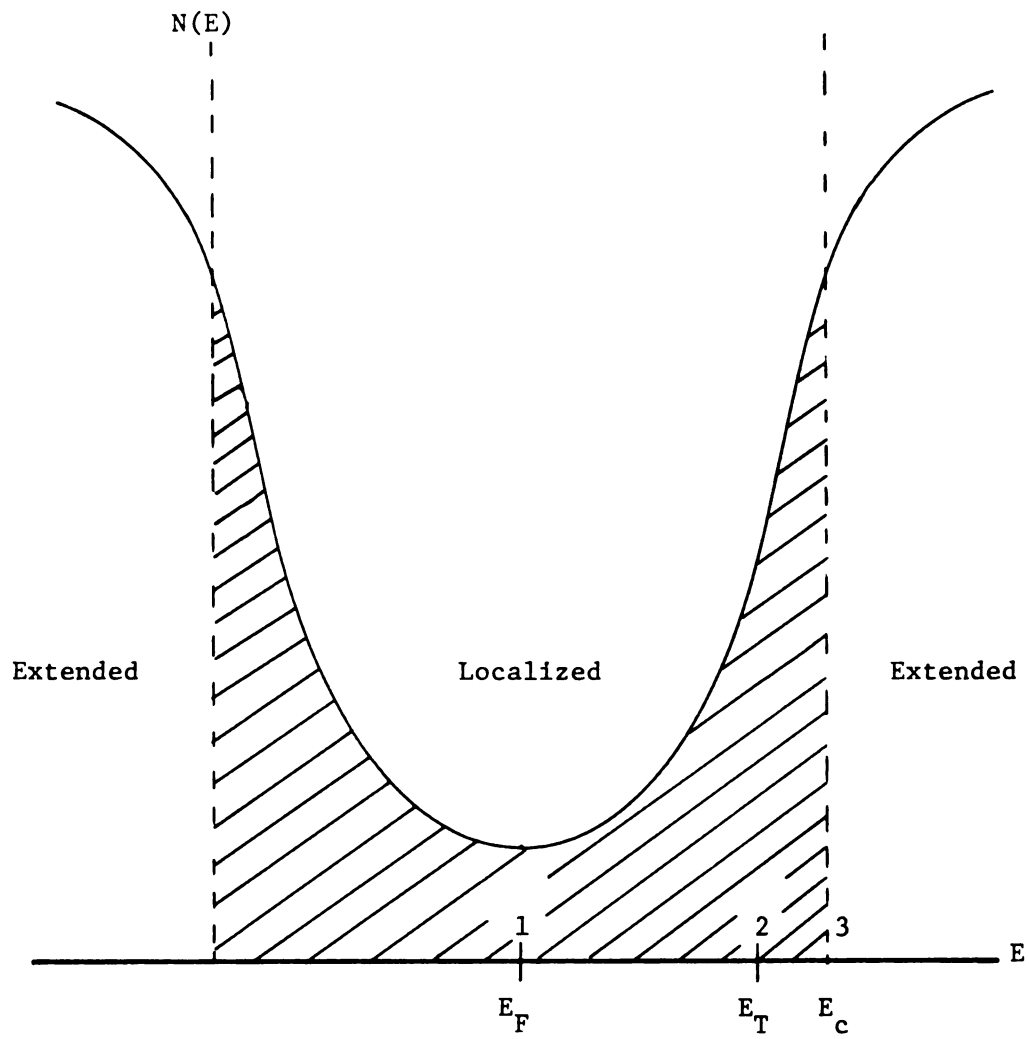
(unintentionally) shows a considerable increase in optical absorption, especially at lower energies, indicating a large increase in the density of states in the gap.

#### 4.3.4 Dark Conductivity as a Function of Temperature

Several conduction mechanisms are simultaneously responsible for electrical conduction in hydrogenated amorphous silicon. Which one, or ones, predominate depends on the details of preparation and at what temperature the measurement is made.

Although the density of states,  $N(E)$  in amorphous semiconductors does not fall abruptly to zero at the band edge as in crystalline materials, strong theoretical and experimental evidence exists to suggest that a "mobility edge" does exist.<sup>74</sup> The basic premise is that all states at a given energy in a disordered material are either localized or non-localized. The mobility of electrons in the non-localized (extended) states is considerably larger at normal temperatures, leading to a sharp increase in mobility at the critical energy separating the two classes of states. This is shown in Figure 4.13.

If the density of localized states at mid gap is sufficiently large, the states near the Fermi energy,  $E_F$ , will be close enough together to permit tunneling



1.  $\sigma \propto e^{-(B/T^{3/4})}$
2.  $\sigma \propto e^{-(E_T - E_F + W)/kT}$
3.  $\sigma \propto e^{-(E_c - E_F)/kT}$

Figure 4.13 Conduction paths.

from state to state. At this energy, of course, there will be many full and empty states since occupancy at  $E_F$  is defined to be  $\frac{1}{2}$ . In this case the conductivity is given by Mott as

$$\sigma = A e^{-B/T^{\frac{1}{4}}},$$

the weak temperature dependence occurring predominantly in the exponential, although some debate exists as to the temperature dependence of  $A$ .<sup>75</sup> This type of conductivity has, in fact, been reported by others, in unhydrogenated amorphous silicon samples prepared by evaporation, over a wide temperature range, and in hydrogenated glow-discharge samples at low temperatures.<sup>24</sup>

In addition to hopping near the Fermi energy, hopping may take place among the localized band tail states at some energy,  $E_T$ . In this case variation of the conductivity as a function of temperature is due primarily to the limited availability of carriers for conduction at distance  $E_T - E_F$  from the Fermi level, rather than to the variation in hopping probability with temperature as is the case for hopping at  $E_F$ .

In this case

$$\sigma = \sigma_H e^{\frac{-(E_T - E_F + W)}{kT}}$$

and  $W$  is an activation energy for the hopping probability, typically on the order of 0.1 eV.

Conduction in extended states above the mobility edge takes a very similar form

$$\sigma = \sigma_0 e^{\frac{-(E_C - E_F)}{kT}}$$

where  $E_C$  is the energy of the mobility edge.

The activated conductivities due to carriers above and below the mobility edge differ in that  $\sigma_0$  (typically  $10^3$ ) is considerably larger than  $\sigma_H$  (typically less than unity) and  $(E_C - E_F)$  is larger than  $(E_T - E_F)$ .<sup>13,24,75</sup> Which conductivity ends up being larger depends on the product of the two competing terms. The prefactor (related to mobility and number of states available for conduction) is higher for extended state conduction, but the occupation of these states, given by the exponential, is larger for hopping in the band tail.

Which of the three aforementioned conductivity mechanisms is ultimately observed will depend on details of the density of states in the gap as well as on the observation temperature. Extended state conduction is favored for either a low density of gap states, which discourages hopping from state to state, or for high temperatures, when the disparity in availability

of carriers for the conduction processes is not so great.

Both activated types of conductivity have been reported in the literature for amorphous silicon in addition to the Fermi level hopping mentioned earlier. In fact, all three types may sometimes be observed in the same sample at different temperatures.<sup>17,24</sup>

In this study, if a single conduction path is assumed, measurements on all films are interpretable in terms of an activated conductivity with  $\sigma_0$  generally in the  $10^2$ - $10^3$  ( $\Omega$ -cm)<sup>-1</sup> range and  $E_A$  taking on values between 0.7 and 0.83 eV. As shown in Figure 4.14, the prefactor  $\sigma_0$  remains constant with respect to reverse bias to -70 V, then decreases by an order of magnitude as the bias is increased to -130 V. At the higher target voltage, the activation energy shows no clear trend with increasing substrate bias.  $E_A$  does increase quite regularly with substrate bias in samples sputtered at the lower target voltage. This result is shown in Figure 4.15.

The plots of  $\log \sigma$  vs  $10^3/T$ , from which  $\sigma_0$  and  $E_A$  are derived for each sample, are generally linear over the measurable temperature range (~30-200°C). Annealing effects over the temperature cycle are seen only for the high bias samples where the conductivity at low temperatures decreases during the heating cycle.

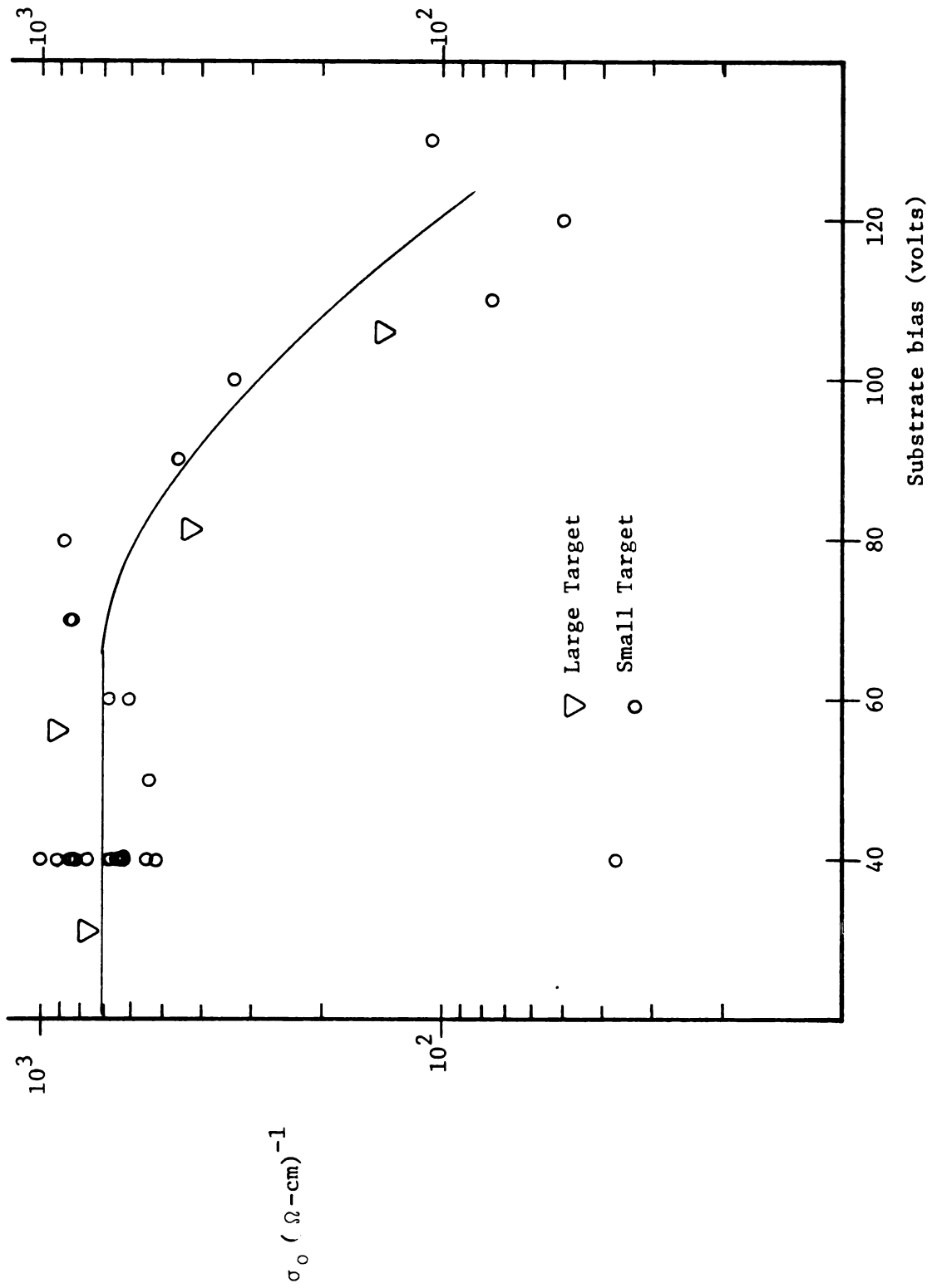


Figure 4.14  $\sigma_o$  vs bias.

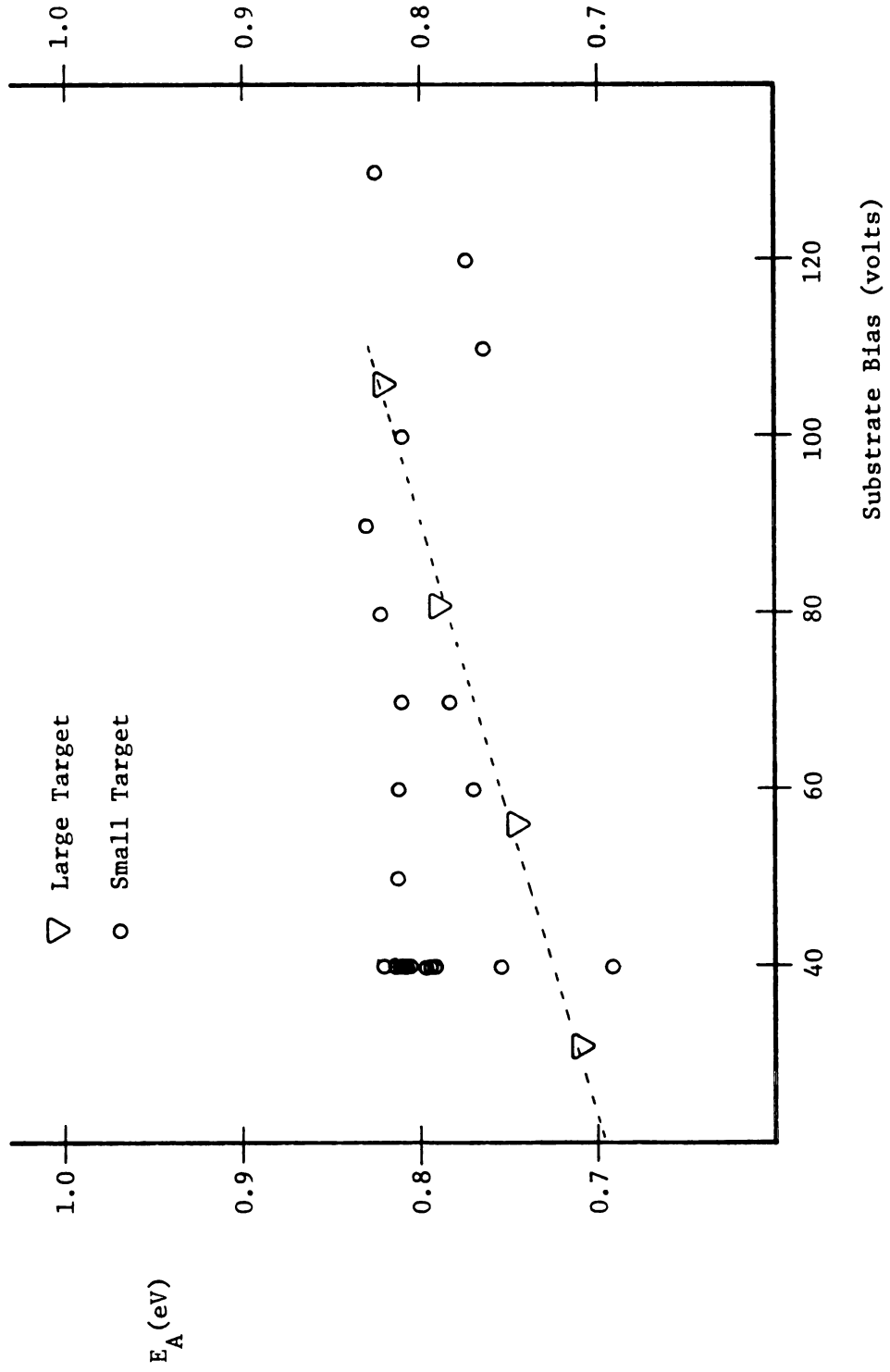


Figure 4.15  $E_A$  vs bias.

These samples also exhibit some curvature in the  $\sigma$  vs  $10^3/T$  plot at low temperatures indicating increased conductivity over that due to the dominant mechanism at higher temperatures. The two types of behavior are shown in Figure 4.16. The significance of this result will be discussed in section 4.3.2.

In this investigation, the prefactor  $\sigma_0$  is not found to be dependant on  $E_A$  as has been reported by some researchers<sup>76</sup> who have claimed large values of  $\sigma_0$  for large  $E_A$  samples. A plot of  $\sigma_0$  vs  $E_A$  for our samples (Figure 4.17) shows a modest spread of  $\sigma_0$  values corresponding to samples deposited at different substrate biases, but no systematic dependance of  $\sigma_0$  on  $E_A$ . Only very high bias samples show  $\sigma_0$  values which differ significantly from the average. Paul and Anderson argue in a recent review that the very high and low prefactors reported in the literature are anomalous and that most values of  $\sigma_0$  fall within a fairly narrow range. This is consistant with our observations.

#### 4.3.5 Photoconductivity: $\eta\mu\tau$ product

The photoconductivity as quantified by the calculation of the efficiency-mobility-excess carrier lifetime ( $\eta\mu\tau$ )product measures the change in conductivity of the material per unit of light absorbed. A few comments as to the significance of  $\eta\mu\tau$  are in order.

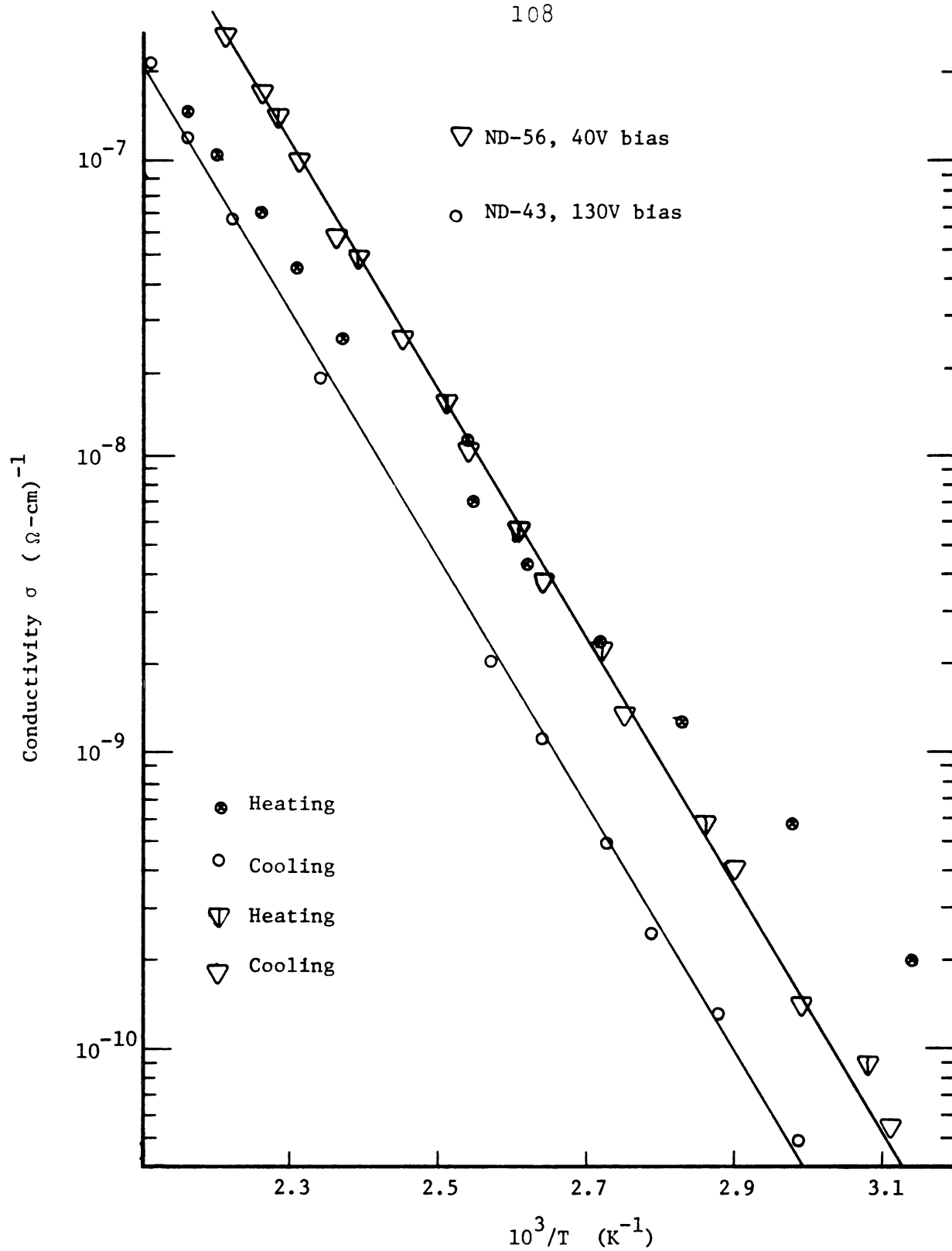


Figure 4.16 Log  $\sigma$  vs  $10^3/T$  for high and low substrate bias samples.

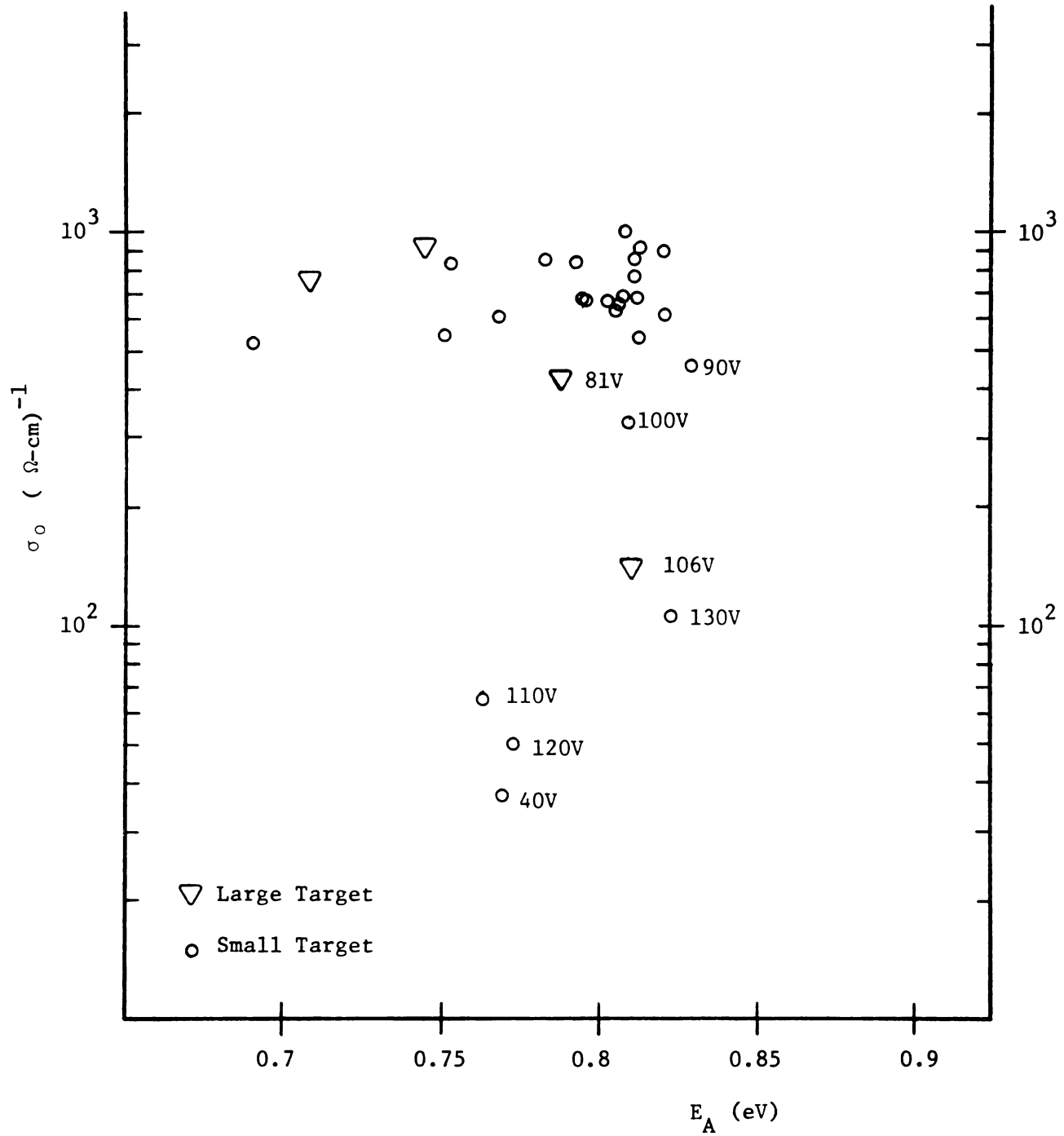


Figure 4.17  $\sigma_0$  vs  $E_A$ , high substrate bias points indicated.

In general a high  $\eta\mu\tau$  product is desirable since for a good photovoltaic material each of the three individual terms should be as large as possible. The generation efficiency  $\eta$  is the fraction of absorbed photons which generate electron hole pairs that do not recombine immediately,  $\mu$  is the mobility of the carrier responsible for conduction, in this case the electron, and  $\tau$  is the average time for a photogenerated carrier to recombine.

While a high  $\eta\mu\tau$  product is certainly desirable, all other things being equal, and provides useful information about the material, it is by itself not a good predictor of photovoltaic performance. For example, the highest photoconductivity amorphous silicon turns out to be material doped with phosphorus and having a low activation energy.<sup>12,13,17</sup> Phosphorus impurities in the bulk of the solar cell even in relatively low quantities seriously degrade cell performance.<sup>10</sup> Apparently the doping eliminates charged recombination centers<sup>17</sup> and/or increases hole trapping in the doped material.<sup>13</sup> Either of these changes inhibits recombination and thereby increases  $\eta\mu\tau$ . Since solar cell applications require efficient minority carrier transport, an increase in hole trapping can have opposite effects on  $\eta\mu\tau$  and solar cell performances.

A strong correlation is often seen between  $\mu\tau$

and the activation energy for conduction in amorphous silicon films and speculation exists that the effect is relatively independent of the mechanism shifting the Fermi level.<sup>12,13,78</sup>

In general, the normalized photoconductivity  $\eta_{\mu\tau}$  in amorphous silicon varies with incident light intensity. Spear and Lecomber report a change from a photoconductivity independent of light intensity, to a strongly intensity dependent photoconductivity as their films are phosphorus doped and the dark conductivity increases.<sup>17</sup> They interpret these results in terms of a change in the recombination from a monomolecular to a bimolecular process. Staebler and Wronski report a similar phenomenon in conjunction with changes in photoconductivity (and dark conductivity) induced by light soaking.<sup>77</sup>

For a monomolecular recombination process  $\eta_{\mu\tau}$  is independent of intensity. For a bimolecular process the normalized photoconductivity decreases with increasing intensity.

$$\eta_{\mu\tau} \propto I^{\beta}$$

$I$  = intensity

$\beta$  = 0 for monomolecular,

-0.5 for bimolecular

In the context of this background discussion the photoconductivity results of the current study

are now presented. The discussion refers to results presented graphically in Figures 4.18 through 4.22. For samples sputtered using the high voltage target, the variation of  $\eta\mu\tau$  with substrate bias is very similar to that of  $\sigma_0$  for the same samples. That is, the photoconductivity decreases by an order of magnitude for substrate biases increasing from -70 to -130 V. Samples sputtered at the lower target voltage show a considerably higher sensitivity to substrate bias effects, and the  $\eta\mu\tau$  product decreases by nearly 3 orders of magnitude between 31 and 106 volts bias.

The measured photoconductivity does show a strong correlation with the activation energy. The samples which do not fit the pattern are all samples exhibiting a low  $\sigma_0$ , suggesting a fundamentally different effect at high substrate biases.

Measurements of the photoconductivity vs. volume density of photons absorbed/second reveal that in our samples the photoconductivity does vary considerably with light intensity, by perhaps an order of magnitude over  $3\frac{1}{2}$  orders of intensity variation. Depending on the sample and the intensity,  $\beta$  varies between about 0.2 and 0.5. Samples exhibiting high and low photoconductivities exhibit essentially the same variation with light intensity.

We find, as previously reported by Stabler

and Wronski, that the effect is stronger in the high photoconductivity (low  $E_A$ ) samples. The light soaked state also exhibits a higher activation energy and much lower dark conductivity, which anneal to the original state above 150°C, typical of samples exhibiting light induced changes.<sup>77</sup>

#### 4.4 Discussion of Results

##### 4.4.1 Optical Measurements

The optical measurements indicate no measurable change in the material properties to which they are sensitive as a result of variation of the substrate bias over the range investigated. These properties include the void volume, amount of hydrogen incorporated, separation between the conduction and valence bands and large increases in number of gap states. Of course some of these parameters are interrelated, and the list could be lengthened, but the overall indication, which is supported by the electrical measurements, is that the material at all biases is similar in that it is hydrogenated amorphous silicon containing about 22 atomic% hydrogen.

Our optical absorption results are not expected to change with small changes in the density of gap states since the optical absorption caused by a typical density of gap states<sup>13</sup> is far below the sensitivity

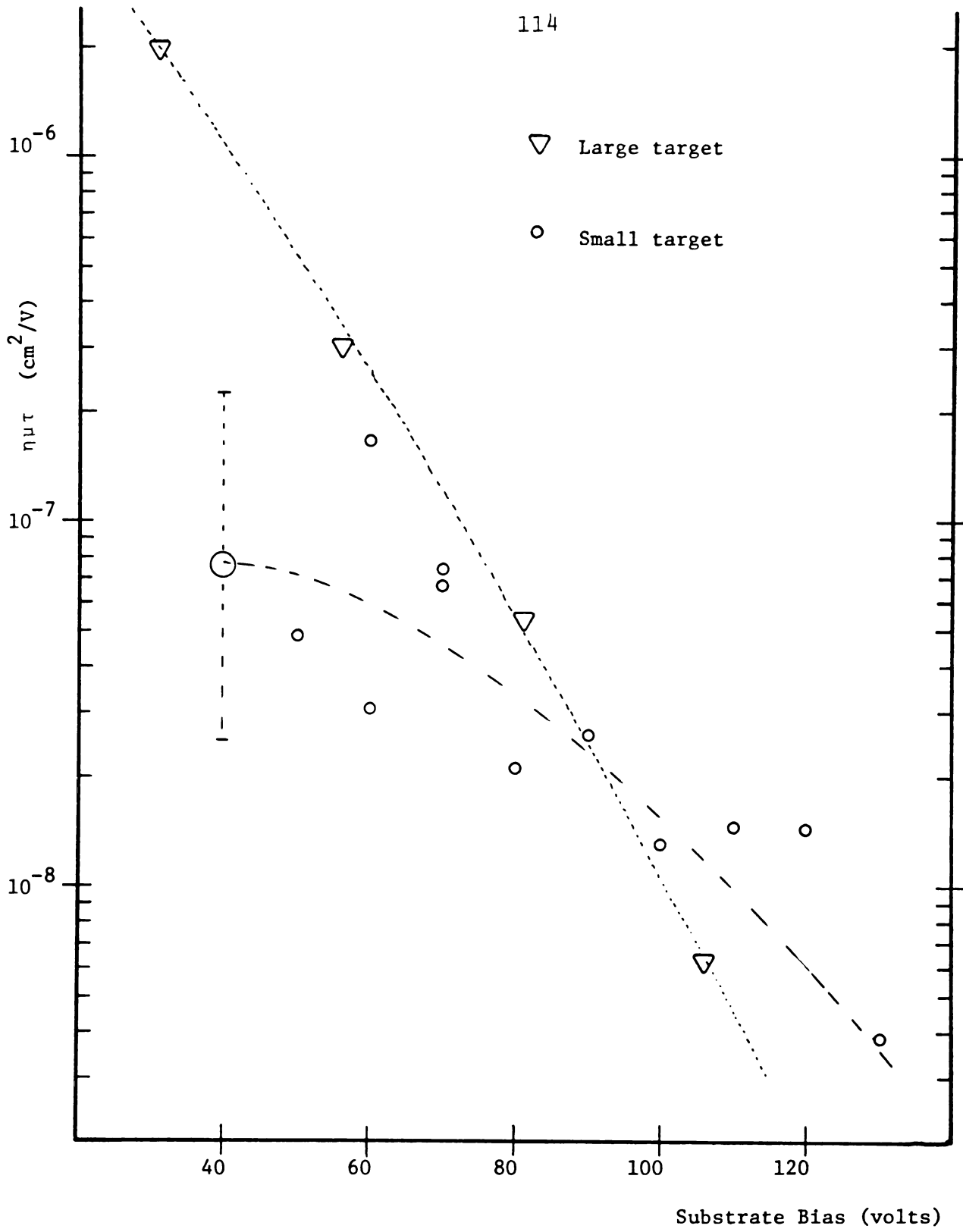


Figure 4.18 Photoconductivity vs substrate bias.

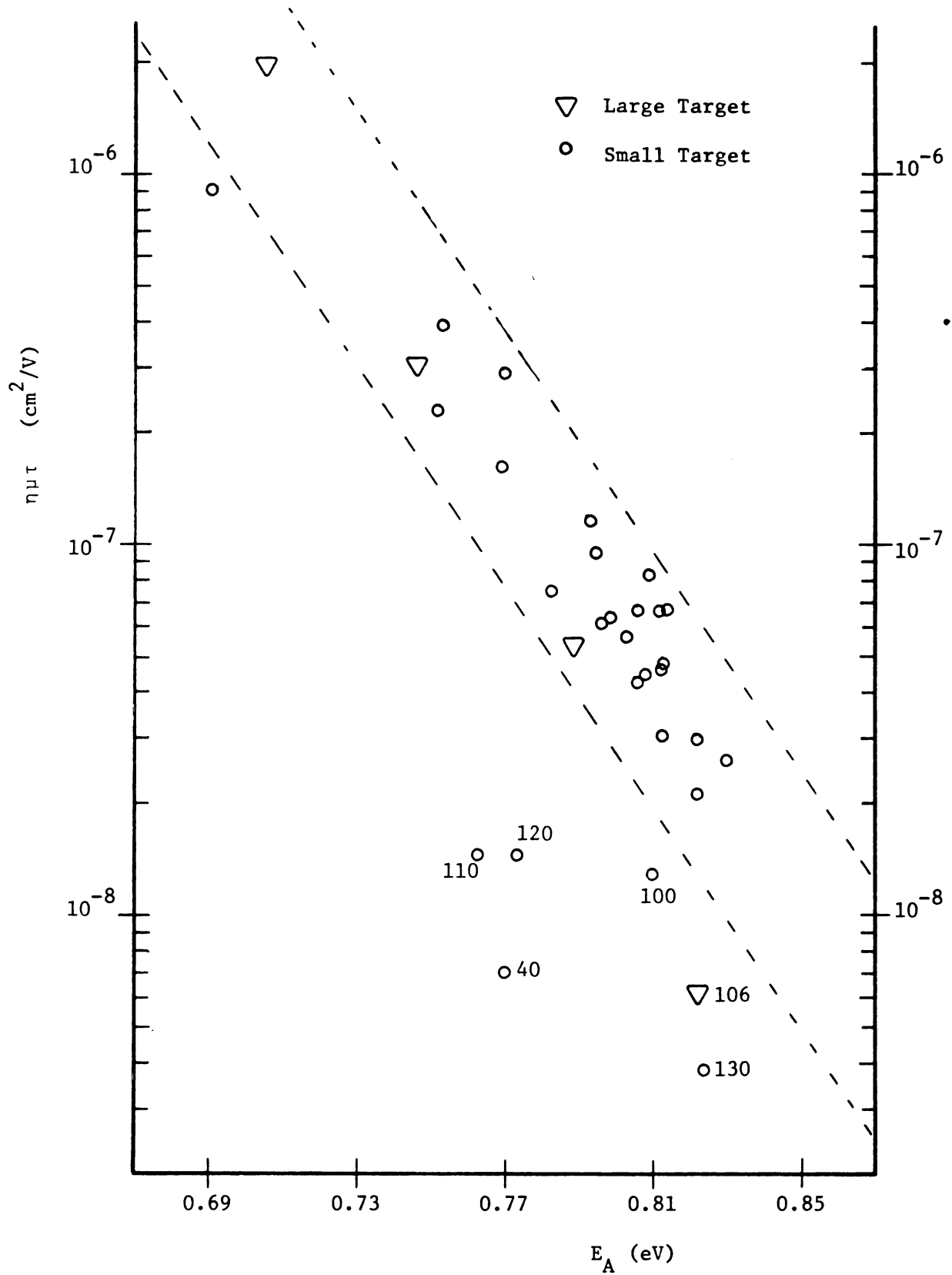


Figure 4.19 Photoconductivity vs  $E_A$ , high bias points indicated.

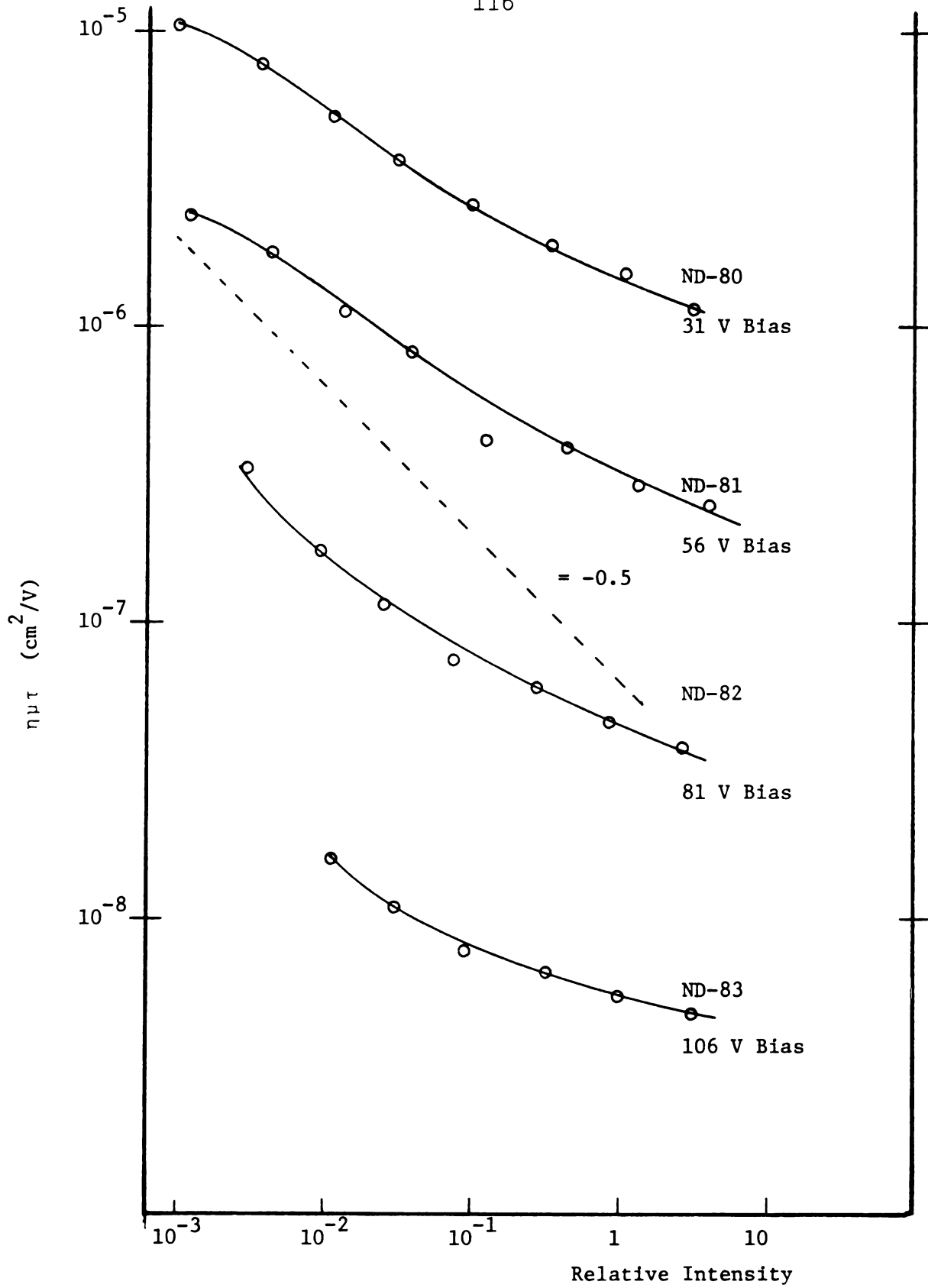


Figure 4.20 Photoconductivity vs intensity.

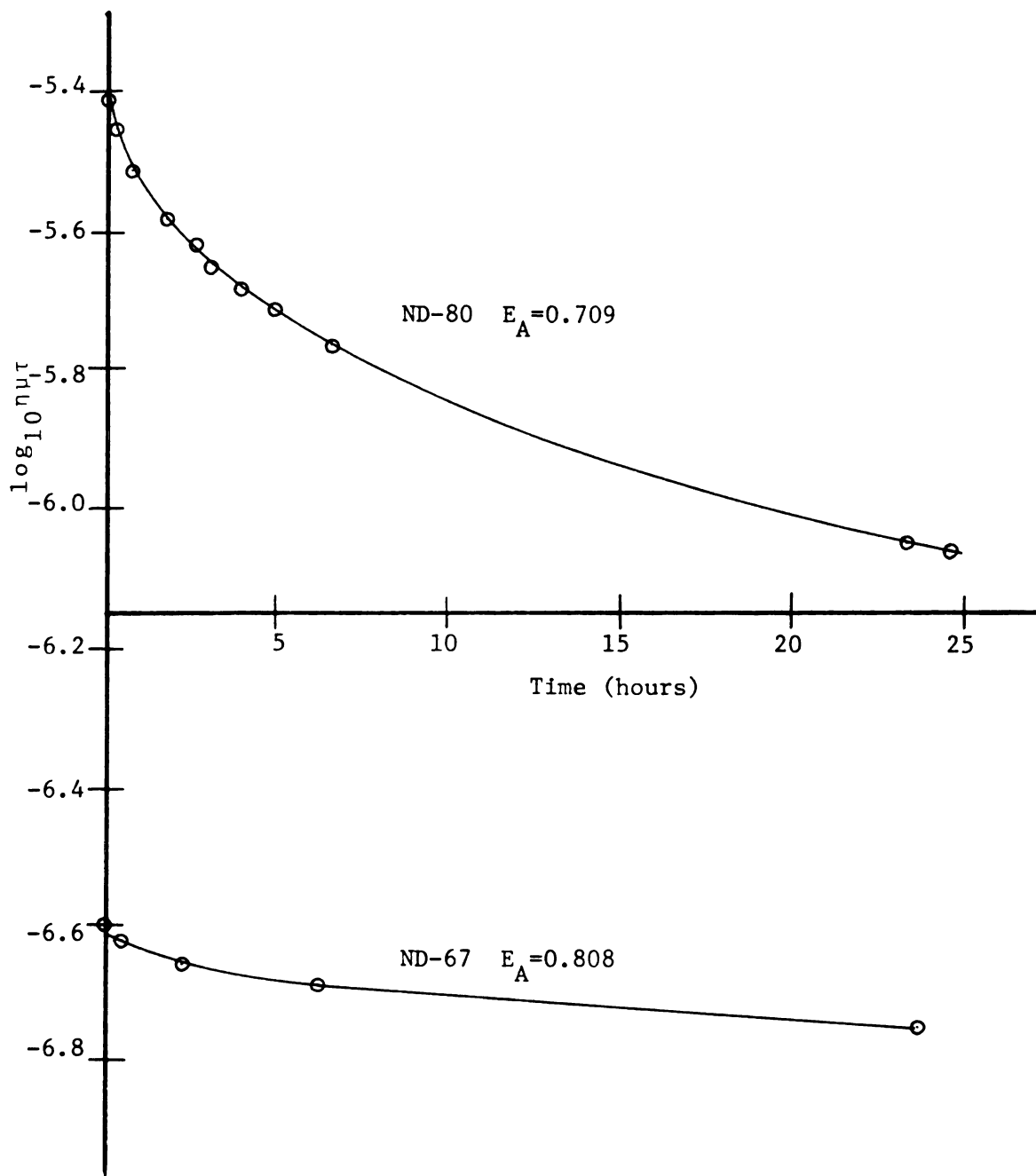


Figure 4.21 Decrease in photoconductivity with light soaking in  $200 \text{ mw/cm}^2$ , 650 nm light.

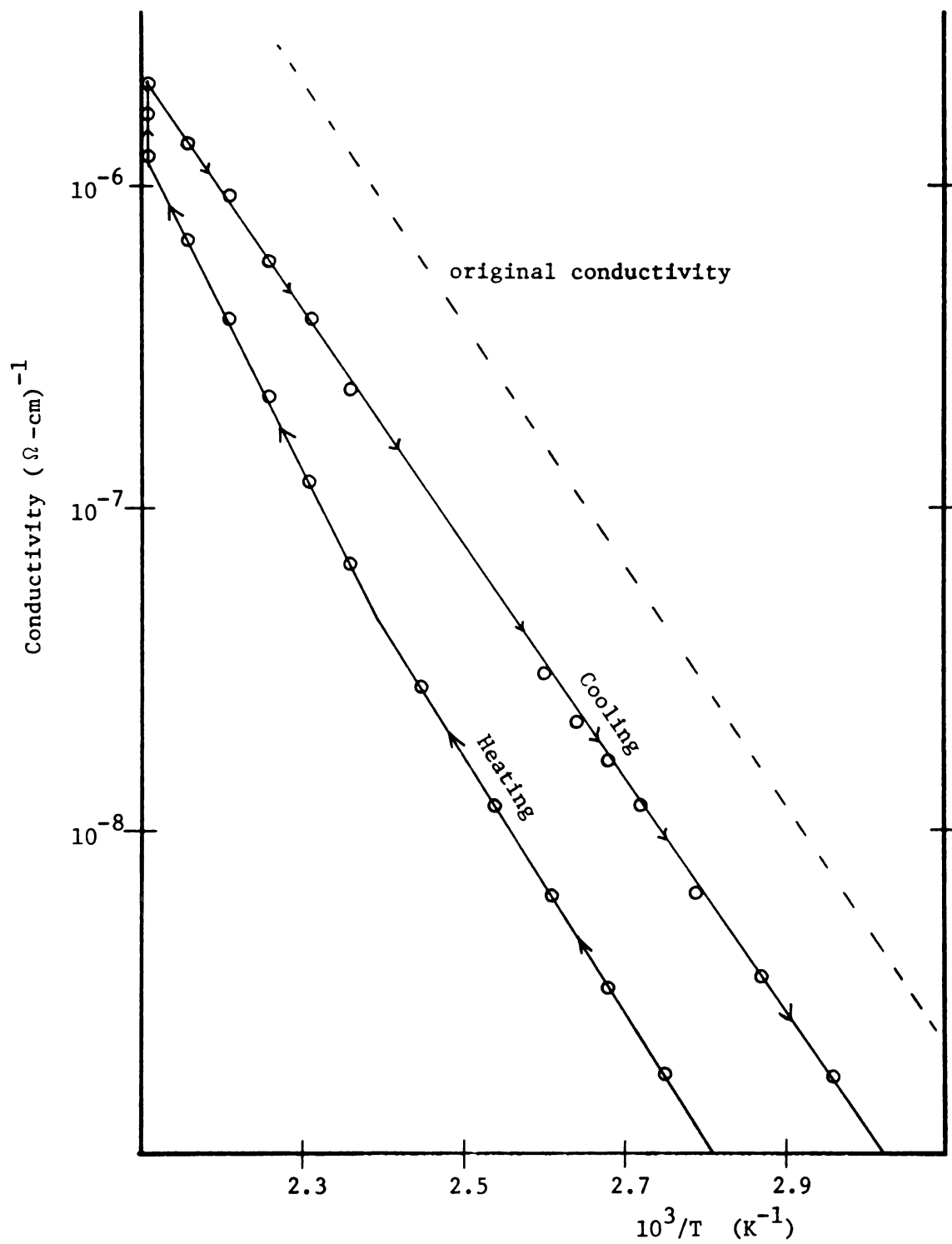


Figure 4.22 Annealing of light soaked sample ND-80.

of our apparatus; the films appear to be transparent for  $\lambda > 800$  nm. On the other hand, films doped with phosphorus or aluminum (ND-7 and ND-29 respectively) do show an appreciable increase in sub-bandgap absorption, indicating a very large increase in the density of states in the gap.

Changing the target bias did change optical properties. The optical absorption results from the samples sputtered at lower target voltage (1310 V rather than 2350 V, same deposition rate) are consistent with a simple shift to higher energies of the optical absorption edge. A change of this sort in the optical energy gap of amorphous silicon is most often associated with an increase in hydrogen content, although this was not verified experimentally in this work.

For samples sputtered using the larger, low voltage target, requiring that the deposition rate be the same as in the high voltage runs resulted in a lower sputtering power as measured at the input to the matching network. As mentioned in Chapter III, the power absorbed in the sputtering chamber is uncertain to the amount of losses in the matching network. Although these losses are expected to be smaller for the lower voltage runs, the power coupled into the plasma is indeed believed to be less when the lower voltage target is used. This also makes sense in terms

of typical sputtering yields which begin to saturate at around 1000 V. The most efficient ion energy for sputtering in terms of sputtered particles/unit energy varies with the ion and sputtered material, but is typically around 300-400 V.<sup>81</sup> These numbers imply that the lower voltage discharge is likely to be more efficient and require less power input for the same deposition rate, which is what is observed. (The standard deposition rate is 40Å/minute at either power; 75 W for the large target, 43 W for the small target.)

The effects of varying the sputtering power have been studied to some extent by others for amorphous silicon and indications are that the hydrogen content of the film, as well as the optical gap, decrease as the power increases. These studies differ from the present study in that the deposition rates were not held constant.<sup>66,70</sup> Another paper presents evidence that the hydrogen content of the sputtered film is determined by the ratio of the hydrogen partial pressure and the deposition rate, but no indication of power absorbed by the plasma or plasma density is given. If the increase in optical gap of our low target voltage samples is indeed due to an increase in hydrogen content, as seems likely, it indicates that the ratio of hydrogen partial pressure to deposition rate is not the sole

factor determining hydrogen content.

The marked insensitivity of the optical gap and refractive index, which are related to hydrogen content, to substrate bias, is evidence against the mechanism for hydrogen incorporation being surface reactions with hydrogen ions. The positive ions are expected to bombard the surface in greater numbers and at higher energies as the negative substrate bias is increased. On the other hand, saturation effects in the hydrogen content with increasing hydrogen partial pressure may cause the change in hydrogen content with other deposition parameters to be fairly small at our standard deposition pressures.<sup>12,81</sup>

#### 4.4.2 Electrical Measurements

In contrast to the results of the optical measurements, substantial changes are seen in dark conductivity and photoconductivity as a function of substrate bias. This result reflects the sensitivity of these parameters to fairly small changes in the density of states in the gap.

Several effects and interdependencies are seen. Three are singled out for further comment here. First, the photoconductivity ( $\eta\mu\tau$ ) increases as the activation energy decreases. That is, the scatter of  $E_A$  data in Figure 4.16 and the scatter of  $\eta\mu\tau$  data in

Figure 4.19 are correlated as shown in Figure 4.20. Second, the activated conduction prefactor,  $\sigma_0$ , decreases by an order of magnitude at high negative substrate bias, in the same samples that show annealing effects and appreciable curvature in the plot of  $\log \sigma$  vs  $10^3/T$ . Finally, the photoconductivity decreases by an order of magnitude at high substrate bias for the high target voltage samples and by 3 orders of magnitude over the whole range of increasing substrate bias for the low target voltage samples. These observations are considered as follows.

As mentioned earlier, a substantial body of amorphous silicon research on deposition variables other than substrate bias, especially on doping, establishes a general dependence of the photoconductivity on  $E_A$ . A definitive answer to the question of why the photoconductivity increases as  $E_A$  decreases is lacking in the literature, although a number of plausible explanations have been advanced.<sup>13,78,83,84,85</sup> Most of the explanations center around the change in occupancy of fast recombination centers near the middle of the gap with changes in the Fermi level,<sup>78,83,85</sup> although an increase in hole trapping with phosphorous doping, which also inhibits recombination has been suggested.<sup>13</sup> In any case, our results show that the photoconductivity varies with activation energy in a regular and predictable

way for essentially all low substrate bias samples. See Figure 4.19. However, at high substrate bias, the photoconductivities ( $\eta\mu\tau$ 's) deviate from the "regular"  $\eta\mu\tau$  dependence on activation energy. As compared to samples sputtered at the high target voltage, the low voltage target samples show a greater and more regular variation in activation energy,  $E_A$ , with bias, but show the same variation in measured  $\sigma_0$  at high bias and the same anomalous  $\eta\mu\tau$  variation for high bias, low  $\sigma_0$  samples. We interpret this to mean that very large substrate biases produce "damaged" films with low photoconductivities. The mechanism for the damage is elaborated on later in this section. The activation energy is sensitive to small changes in the number or distribution of states in the gap, which means that  $E_A$  is likely to be very sensitive to deposition parameters. In fact, in this study as in many others, this results in scatter in  $E_A$  and thus in dark conductivity and photoconductivity from run to run under nominally identical conditions. Thus it is not surprising to find that the activation energy varies with substrate bias in the samples sputtered with the low voltage target, but it perhaps is initially surprising that  $E_A$  does not change with substrate bias in the same way for samples sputtered with the high voltage target. Substrate bombardment is, however,

affected by both substrate bias and target bias. For samples sputtered with the high voltage target, bombardment due to the high target voltage dominates the substrate bias induced bombardment except at high values of substrate bias.

Next we consider the variation of  $\sigma_0$  and  $\eta\mu\tau$  with substrate bias. At high substrate bias,  $\sigma_0$  and  $\eta\mu\tau$  are both seen to decrease by an order of magnitude, and apparently this  $\eta\mu\tau$  variation is in addition to its normal dependence on the activation energy. Although this research is not designed to study in detail the conduction mechanisms in hydrogenated amorphous silicon, some discussion of the reason or reasons for the decreases in  $\sigma_0$  and  $\eta\mu\tau$  is appropriate at this point.

For extended state conduction by electrons, the conductivity is given by<sup>13</sup>

$$\sigma = \sigma_0 e^{-(E_C - E_F)/kT}$$

$$\sigma_0 = N_c kT q \mu_c e^{\gamma/k}$$

where  $N_c kT$  is an effective conduction band density of states and  $\mu_c$  is the band mobility of the electron. The exponential in the  $\sigma_0$  expression allows for any shift,  $\gamma$  of the Fermi level with respect to the band edge. The photoconductivity is given, as in Chapter III,

by

$$\sigma_{ph} = q\mu_t\tau_r\eta A$$

where  $A$  is the number of photons absorbed/cm<sup>3</sup>,  $\eta$  is the generation efficiency and  $\tau_r$  is the recombination lifetime for the electron. The trap limited mobility,  $\mu_t$ , is used for the excess carrier mobility since the electrons suffer capture and release from shallow traps before final recombination. The hole contribution is normally neglected since the trap limited hole mobility is thought to be much lower due to the presence of deep hole traps.<sup>13</sup>

Looking only at the equations, the most likely cause for the observed simultaneous decrease in  $\sigma_o$  and  $\sigma_{ph}$  would seem to be a decrease in  $\mu_c$ , the band mobility, which would cause an equal decrease in  $\mu_t$ . Thus  $\sigma_o$  and  $\sigma_{ph}$  would decrease by the same amount, for the same reason. In reality, a decrease of this magnitude in the microscopic mobility of an amorphous semiconductor is highly unlikely, especially considering the relatively small changes observed in other material properties. In addition, the more sensitive parameters  $\tau_r$ , and the trapping affecting the trap limited mobility would be expected to reduce the photoconductivity much more quickly than  $\sigma_o$  with increasing bombardment damage.

Another, perhaps somewhat more plausible explanation

for the observed behavior is that the reduced  $\sigma_0$  and photoconductivity are a result of increased long range potential fluctuations at the higher bombardment levels. These potential fluctuations would have the effect of confining the predominant current path to filaments of area smaller than the total area of the sample, reducing  $\sigma_0$  due to an effective decrease in the density of states participating in conduction. A weakness of this explanation is that the photoconductivity would not necessarily decrease since the number of excess carriers generated by absorption of photons and participating in conduction is not changed due to the potential fluctuations. On the other hand, a coincidental increase in the number of recombination centers, decreasing  $\tau_r$  and the photoconductivity is possible at the higher bombardment levels and is consistent with the results.

A two path conductivity model fits the experimental results better than either of the aforementioned explanations, and has considerable precedent in amorphous silicon literature. A number of researchers have suggested two parallel conductivity paths, the lower mobility and activation energy path appearing at low temperatures or high doping levels.<sup>12,17,24,87</sup>

A simple activated conductivity is expected to yield a straight line on a plot of  $\log \sigma$  vs  $10^3/T$ . On close inspection, virtually all the samples in this

research show a certain amount of curvature in the log  $\sigma$  plot, always concave upward. The high bias, low  $\sigma_0$  samples show the most curvature.

A conductivity given by

$$\sigma_0' e^{-(E_c - E_F)/kT} + \sigma_h e^{-(E_T - E_F + W)/kT}$$

fits the measured conductivities to within experimental error, and better than the straight line approximations from which the  $\sigma_0$  values quoted earlier in this chapter are derived. Values of  $2000 (\Omega\text{-cm})^{-1}$  for  $\sigma_0'$ , 0.38 for  $E_T - E_F$  and 0.1 for  $W$  provide good fits to the data. The values of  $E_F$  and  $\sigma_h$  vary from sample to sample. See Figures 4.23 and 4.24.

The interpretation of this model is that activated conduction occurs at two levels, at the mobility edge, with a prefactor that is characteristic of extended state conduction in hydrogenated amorphous silicon, and in a band of states of variable density, lying below the mobility edge. Conductivity at the second level is enhanced at sufficiently high bombardment levels. This is evidenced by the fact that  $\sigma_h$  is larger for the high bias samples.  $E_F$  varies from sample to sample, but is generally further from  $E_c$  for the high substrate bias samples. Holding  $\sigma_0'$  and  $E_c - E_T + W$  constant as providing good fits to all data and being constants of the material,  $E_c - E_F$  varies between 0.743

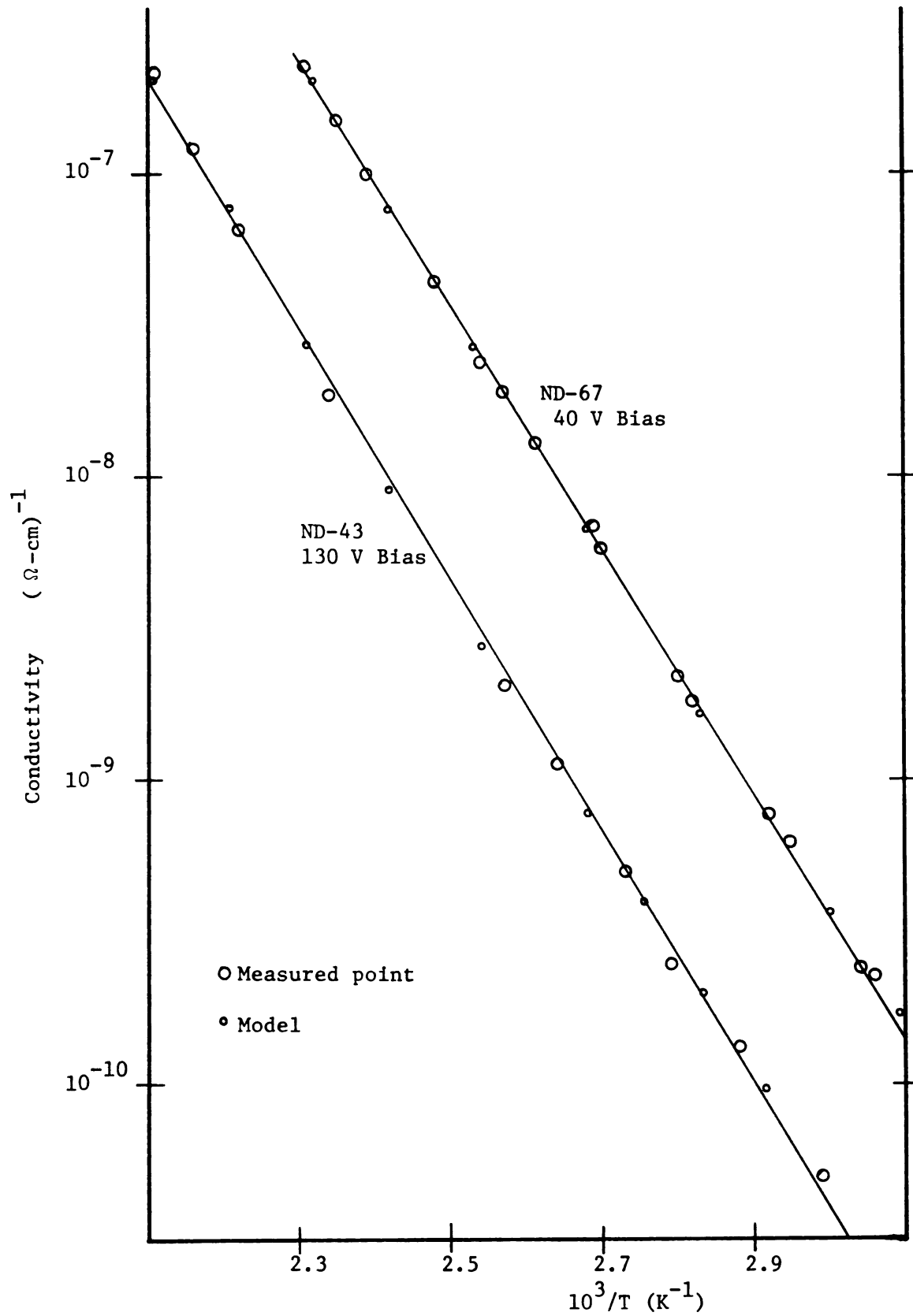


Figure 4.23 Model fit for high and low substrate bias samples.

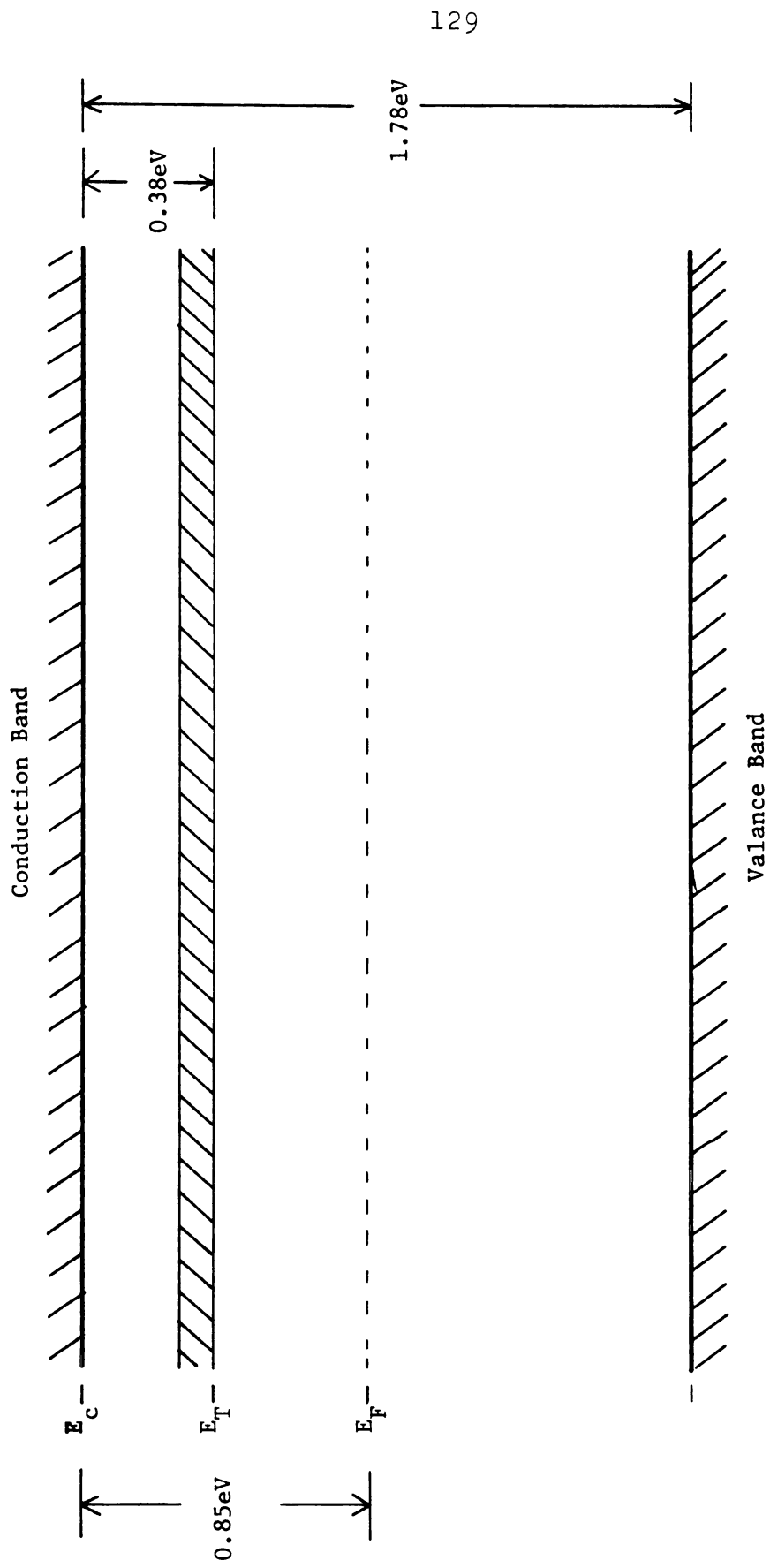


Figure 4.24 Band diagram for 2 conductivity paths. (ND-67)

and 0.946 eV and  $\sigma_h$  between 0.03 and 0.43. These values for  $\sigma_o'$  and  $E_c-E_F$  are consistent with those reported by researchers for high quality amorphous silicon films.<sup>13,88</sup> The alternate conductivity path appears to be somewhat similar to one introduced by phosphorus doping.<sup>59,87</sup> Values of  $W$ , the activation energy for the hopping process are typically on the order of 0.1 eV.<sup>57</sup>

At this point it should be noted that while the two path conductivity model has precedent and is consistent with the experimental results the values of the parameters are not certain to a high degree of accuracy. The result of the introduction of the two path conductivity is to produce a slight curvature in the predicted  $\log \sigma$  vs  $10^3/T$  curve. (Of course, in addition, it explains the mechanism for the observed decrease in  $\sigma_o$ .) The ratio of the prefactors is adjusted to fit the observed curvature. With the amount of experimental error present, a range of parameters is reasonable, so the  $\sigma_o'$  and  $\sigma_h$  values are only known to within a factor of 2 or so. The values of the exponents ( $E_c-E_F$  and  $E_T-E_F+W$ ) are considerably less sensitive to experimental error, although the reference energy shift  $\gamma$ , which is unknown and may be small, must be subtracted from ( $E_c-E_F$ ) and perhaps from ( $E_T-E_F+W$ ), depending on its origin.

This two path model also offers plausible explanations for the decrease in photoconductivity with increased trapping in the enhanced hopping band and with the downward movement of the Fermi level for low  $\sigma_0$  samples.

#### 4.4.3 Comparison with Other Bias Results

Three other groups have studied the effects of substrate bias on sputtered amorphous silicon over the last two years. A Japanese group reports decreased ESR spin density and increased photoconductivity with increasing bias on unhydrogenated amorphous silicon sputtered at argon pressures >200 millitorr.<sup>89</sup> Since the material is unhydrogenated, there is little point in comparison with this work. Another study, again conducted at fairly high argon pressures (20-150 mTorr) concludes, in substantial agreement with the results of our optical measurements, that bias sputtering at -150 or -300 volts has no effect on hydrogen content or bonding configuration.<sup>90</sup> A third group at the University of Sheffield has done significant work on high quality hydrogenated amorphous silicon similar to our material.<sup>91,92</sup>

The material at the University of Sheffield was grown under deposition conditions rather similar to ours; 6 millitorr argon, 0.4 or 0.8 millitorr hydrogen,

a deposition rate which was only 10% lower and substrate temperature of 240°C. A significant difference was their lower target voltage of 800 V. Recall that our target voltages were 2350 V and 1310 V for the two and three inch targets.

Their results include an increase in photoconductivity with a simultaneous drop in the activation energy for dark conduction at biases less negative than -100 V. See Figure 4.25. In consideration of these results, it is important to realize that the photoconductivity depends upon the (unknown) intensity of the incident light and that, as described earlier, the bias voltage scale, although measured in the same way as in this work, is somewhat arbitrary. Other results include a reported 10% increase in refractive index and a 0.05 eV reduction in optical gap as the bias increases from 0 to -100 V. The hydrogen concentration in the 0.4 millitorr H<sub>2</sub> samples, as measured by hydrogen evolution, is reported to fall from 12% at zero bias to 10% at 50 volts bias and above, and the percentage of hydrogen attributed to the 2000cm<sup>-1</sup> absorption peak (SiH bond) is said to increase by a factor of two at moderate bias levels.

Some of the above results are clearly different than those of the present study. The hydrogen content of our films is apparently higher, which is surprising

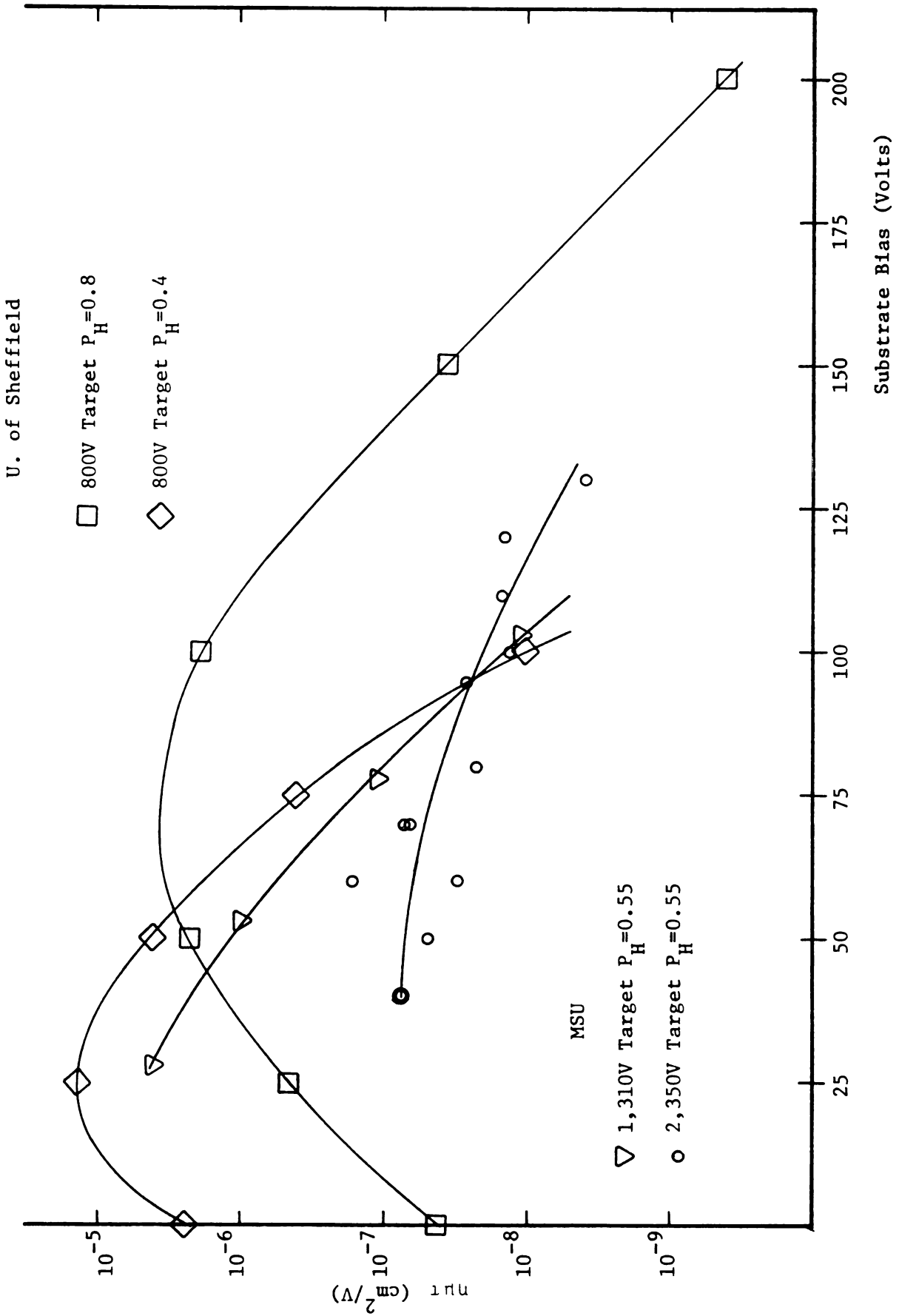


Figure 4.25 Photoconductivity vs substrate bias. MSU and U. of Sheffield results.

considering the similarity of sputtering conditions. We do not see the changes with bias in refractive index or optical gap, although the sensitivity of our measurements is great enough. Finally, the position of the Fermi level and the photoconductivity are not as sensitive to bias in the present work. If the hydrogen content is indeed lower, the greater variation of the optical gap and index could be due to a lack of the saturation effects referred to earlier which may come into play at higher hydrogen concentrations. Our decreased sensitivity of  $E_f$  and  $\eta_{PT}$  to substrate bias is presumably due to our larger target voltages, which mask small substrate bias effects.

Several other reports of interest in relation to bombardment effects are found in the literature. Ross and Messier measure the floating potential of the substrate with respect to argon pressure and find that the floating potential of the substrate varies from -18 to -50 volts with respect to the plasma potential as the argon pressure is decreased from 30 to 7 millitorr in their sputtering system.

A study of the properties of amorphous silicon films sputtered at identical deposition rates in the same atmosphere, as a function of target voltage in a triode sputtering system, revealed a linear increase in hydrogen content from 5 to 27 atomic % as well as

an increase in trapped argon as the target voltage was increased from 100 to 2000 volts.<sup>94</sup> In addition films sputtered at less than 800 volts target bias were porous and showed evidence of hopping transport near the fermi level.

Another rather unusual experiment correlates increased argon content and  $\text{SiH}_2$  over  $\text{SiH}$  formation in the film with increased substrate bombardment by high energy neutrals reflected from the sputtering target at small angles.<sup>95</sup>

#### 4.5 Conclusions

The measurements in this chapter show first that we are working with high quality amorphous silicon, typical of the best sputtered material. The measured optical constants as well as the observed conduction at the mobility edge and the high photoconductivity are all indicative of state of the art sputtered material. Further evidence that our material is "device quality" is provided by the Schottky barrier results in Chapter V.

The optical measurements indicate that no large increase in either void volume or hydrogen content occurs as a function of bias or target voltage. Results of electrical measurements show that the electrical properties of sputtered hydrogenated amorphous silicon as

prepared in this study are sensitive to bombardment effects induced by substrate bias. A pattern of increased sensitivity to bias effects is seen as the target voltage is decreased, first in our results at high and low target voltages, then continuing in the results reported by the group at the University of Sheffield for a still lower target voltage. This observation is interpreted as bombardment effects at the higher target voltages masking the effects of bombardment due to substrate bias.

Conduction in our films appears to take place at two levels, in extended states at the mobility edge and by hopping in a band of defect states whose density increases at high substrate biases.

The Fermi level position is insensitive to bias effects for the high target voltage samples to -80 V substrate bias, but becomes more sensitive at the lower target voltage in this study and at the still lower target voltage reported by the group at the University of Sheffield. This is consistent with the film properties being limited by bombardment from the target under conditions of low substrate bias and high target voltage.

A certain amount of bombardment of the film by species from the plasma during growth appears to be beneficial, but either high substrate biases ( $> \sim 100V$ ) or high target voltages ( $> \sim 1000V$ ) lead to over

bombardment and undesirable changes in the film properties.

## CHAPTER V

## SCHOTTKY BARRIER RESULTS

## 5.1 Introduction

The construction of Schottky barrier photovoltaic diodes using the material under investigation provides a tool for very direct evaluation of the materials suitability for use in solar cells, one of the main motivations for amorphous silicon research. In addition electrical measurements on Schottky barriers provide insights into the properties of the device and the semiconductor film itself.

The intent of this chapter is first to report the characteristics of Schottky barriers formed on films sputtered at different biases and on films of different thicknesses. In addition factors limiting the potential photovoltaic performance of our material are discussed and a more detailed examination of the device characteristics in relation to device structure is presented.

We have chosen evaporated gold for the Schottky barrier metal. It should be noted that gold-amorphous silicon diodes are not optimal photovoltaic structures. Band bending in the undoped silicon is fairly small

as compared to other structures such as p-n junctions or platinum Schottky barriers, so open circuit voltages and efficiencies are relatively low. The emphasis of this investigation, however, is on material properties and not photovoltaic device design. Gold Schottky barriers have the advantage of simplicity of structure yet allow the investigation of basic material related device phenomena.

## 5.2 Substrate Bias for Schottky Barrier Diodes

Upon review of the coplanar sample results it was decided to examine the characteristics of Schottky barrier photodiodes sputtered at 0 and 30 V bias. The rationale was that the material of most interest for a limited investigation was the "good" material produced at low bias, that is material not damaged in any obvious way due to excess bombardment at high bias. Recall that for the coplanar material of Chapter IV, the smallest achievable substrate bias was 40 V due to the insulating nature of the sample. However, the Schottky barrier structure, with its conducting back contact allows the bias to be reduced to 0 V as described earlier. The Schottky barrier samples, then, represent an investigation of a region of substrate bias not available to coplanar samples in our system. Three 0 bias and two 30 V bias samples were sputtered

using the small target and under conditions nominally identical except for the variations in bias voltage. (Samples ND-71 through ND-75) For comparison purposes, diodes were also fabricated using the larger target.

### 5.3 Schottky Barrier Data

Following the several series of coplanar sample runs a number of Schottky barrier samples were prepared as described in Chapter 3. Several of their properties including photovoltaic parameters, barrier height and rectification ratio are summarized in Figure 5.1. The photovoltaic properties in this figure were measured under  $100 \text{ mW/cm}^2$  of tungsten illumination for comparison purposes. Measured photovoltaic performance in real sunlight was 4 to 6 times better due to the more favorable spectral distribution of the light. For a fair comparison of the short circuit current,  $I_{sc}$  from device to device, the transmittance of the gold film must be considered. This varied somewhat from device to device, since the thickness of the evaporated gold film varied slightly. For sake of simplicity, the normalization is carried out using the transmittance of the gold at a single representative wavelength where the incident light intensity, the gold transmittance and the response of the diode are all large. All devices are normalized to ND-77,

Device #	Substrate Bias	Undoped Layer Thickness	Median $V_{oc}$	Median $I_{sc}$	Median $I_{sc}$	Normalized $I_{sc}$ $\mu A$	Fill Factor	Max. Rect. Ratio	n	$\phi_b$	Comments
ND-71	0	0.71	0.430	4.4	4.4	4.5	0.54	$1.9 \times 10^6$	-	-	Substrate
ND-72	0	0.68	0.370	4.1	4.1	4.5	0.56	$6.4 \times 10^6$	1.22	1.005	Bias
ND-73	30	0.67	0.403	4.4	4.4	4.6	0.53	$4.3 \times 10^6$	1.23	1.033	Test
ND-74	0	0.73	0.400	5.1	5.1	4.8	0.56	$4.4 \times 10^6$	1.24	1.053	
ND-75	30	0.75	0.450	5.6	5.6	6.0	0.50	$3.6 \times 10^5$	1.32	1.063	
-----											
ND-76	30	0.20	0.351	3.1	3.1	3.2	0.54	$1.1 \times 10^2$	-	-	No exponential Characteristic
ND-77	30	0.40	0.395	4.2	4.2	4.2	0.59	$2.2 \times 10^7$	1.30	1.011	Sunlight FF
ND-78	30	0.30	0.407	5.0	5.0	4.5	0.55	$5.7 \times 10^7$	1.23	1.036	
-----											
ND-79	30	0.74	0.442	6.5	6.5	5.4	0.51	$7.5 \times 10^4$	1.25	0.987	Higher sput. rate large target
ND-84	31	0.34	0.387	4.2	4.2	4.4	0.56	$5.0 \times 10^7$	1.16	-	Large target
ND-11	0	0.48	0.47	10.7	10.7	8.5	-	$8.0 \times 10^7$	1.28	1.028	Preliminary device

Figure 5.1 Summary of Schottky barrier Properties.

which showed a representative gold transmittance, and the normalization constant varies around unity, from 0.83 to 1.11.

The Schottky barrier height is derived from measurements of the forward current at 0.13 volts as a function of temperature. The voltage was chosen such that the measurement is from the portion of the I-V characteristic which is determined solely by the barrier characteristic, without series resistance effects. This corresponds to the linear part of the I-V curve on a semilog plot. Some question arises as to whether the diffusion theory or thermionic emission theory for the Schottky barrier current is applicable for amorphous silicon devices. At voltages greater than  $3 kT/q$ , the current densities predicted by the two theories are as follows.<sup>100</sup>

$$J = A^*T^2 e^{-q\phi_b/kT} e^{(qV/kT)} \quad \text{Thermionic}$$

$$J = qN_c \mu E_{\max} e^{-q\phi_b/kT} e^{(qV/kT)} \quad \text{Diffusion}$$

where

$A^*$  = effective Richardson's constant

$T$  = temperature

$\phi_b$  = barrier height

$k$  = Boltzmann's constant

$q$  = electronic charge

$V$  = barrier voltage

$N_c$  = effective density of states in conduction band

$\mu$  = electron mobility

$E_{\max}$  = maximum barrier electric field

$A^*$  and  $E_{\max}$  are relatively temperature independent, so the major difference in functional form is in the  $T^2$  term in the thermionic emission theory expression. The barrier height is derived from the slope of a plot of  $\log I(0.13V)$  vs  $1/T$  for the diffusion theory or  $\log I(0.13V)/T^2$  vs  $1/T$  for the thermionic emission theory. In either case 0.13eV is added to the result due to the temperature dependence of the second exponential. Since virtually all of the temperature dependence is in the exponential, even for the thermionic emission case, either theory leads to good agreement with experiment in the sense that the barrier height plot is indeed linear. See Figure 5.2. The barrier heights derived from the two plots differ somewhat, however, the diffusion theory predicting values about 6% higher.

It has been argued that for amorphous silicon the diffusion theory should apply due to the short mean free path of carriers in the amorphous semiconductor.<sup>99</sup> Rhoderick gives as a criterion for the validity of either theory the relative size of the terms  $\mu_c E_{\max}$  and  $\frac{\bar{v}}{4}$ , where  $\bar{v}$  is the electron thermal

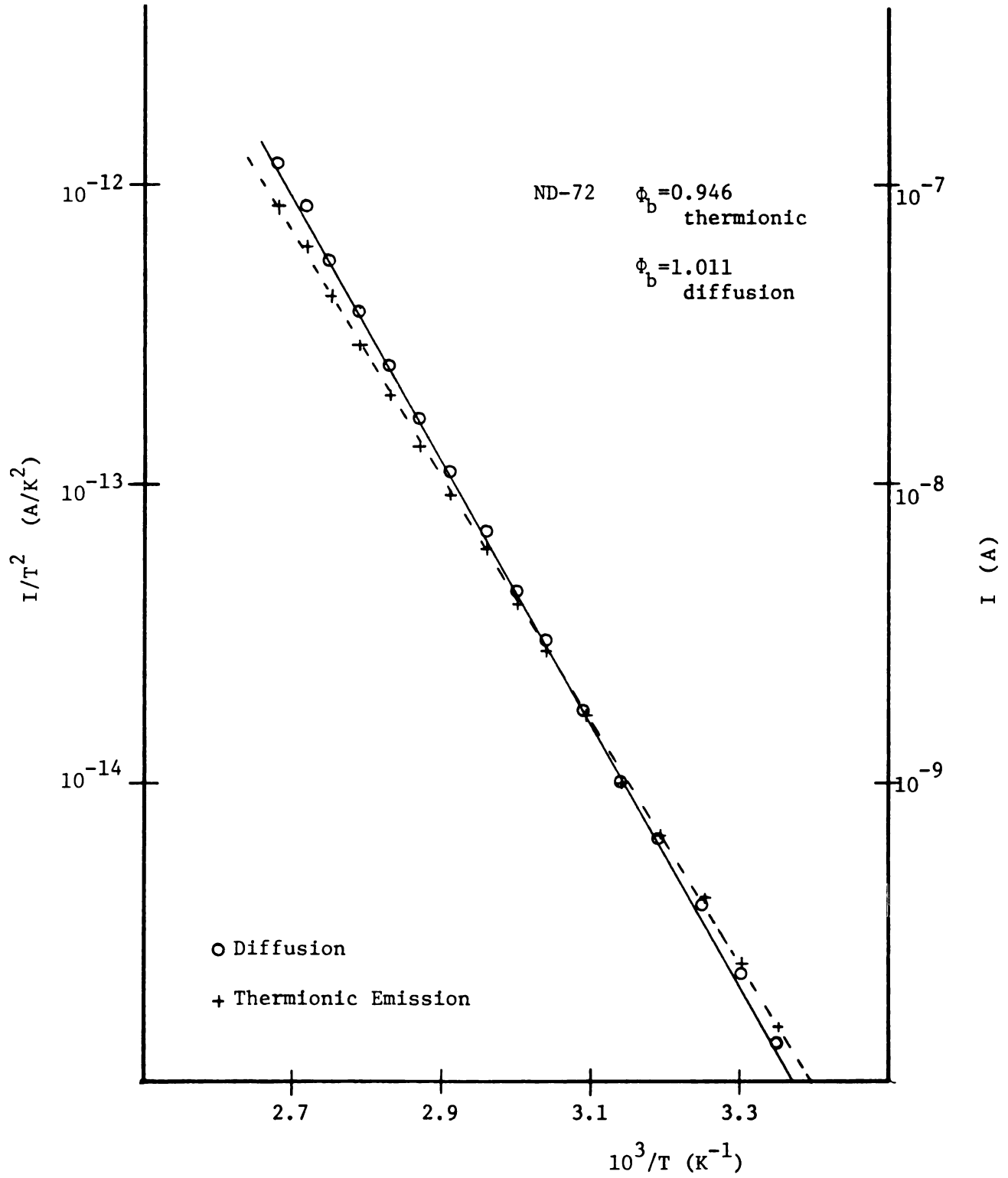


Figure 5.2 Barrier height: diffusion theory, thermionic emission theory.

velocity in the semiconductor. The condition

$$\mu_c E_{\max} \gg \frac{\bar{v}}{4}$$

implies that the thermionic emission approximations are more valid while reversing the inequality provides the condition for validity of the diffusion approximation. Assuming a depletion layer thickness of  $0.3\mu$  and a band bending of 0.6 volts in the semiconductor and assuming the linear increase in electric field toward the junction predicted by the simple abrupt depletion approximation,  $E_{\max}$  is calculated to be  $4 \times 10^4$  v/cm. The thermal velocity of an electron, assuming crystalline silicon material constants, is about  $2 \times 10^7$  cm/sec. The criterion for validity of the diffusion theory is then

$$4 \times 10^4 \mu_c \ll 5 \times 10^6.$$

Estimates for the band mobility,  $\mu_c$  vary considerably, ranging from less than one to greater than 100, and most typically are in the range 5-50.<sup>13,101,102</sup> This would seem to imply that the diffusion theory is applicable, although if the higher mobility applies and  $E_{\max}$  is somewhat greater due to the continuous distribution of gap states in amorphous silicon, the first term could be as large or larger than the second. The quoted values of  $\phi_b$  have been derived based on

the diffusion theory, but it should be realized that if the thermionic emission theory or a theory incorporating both processes<sup>103</sup> is more valid, the barrier height may be overestimated by up to 6%. Other properties summarized in Figure 5.1 were measured as described in Chapter III.

The next three sections discuss the interpretation and significance of the data in Figure 5.1.

#### 5.4 Device Photovoltaic Properties

This section attempts to answer the questions of how the amorphous silicon in this study compare to that used in other amorphous silicon photovoltaics, including those produced in this laboratory previously,<sup>66</sup> and what factors are limiting photovoltaic performance in the devices from this investigation.

First, we note that in agreement with the idea that any bias effects are masked by bombardment due to the high target voltage, no change in Schottky barrier properties outside experimental scatter is seen as the substrate bias is changed from 0 to 30 volts. The 30 volt samples do show marginally improved photovoltaic characteristics over the 0 volt samples, but these results are not viewed as significant. (Refer to Figure 5.1)

Examination of the light I-V characteristics of

our best photovoltaic device, ND-11 reveals a sunlight efficiency of 0.67%. Although uncorrected for gold transmission losses, and for a non-optimal device, this is a low value. Correcting for gold transmission, using the factor at 550nm, which being at a maximum in gold transmittance, will somewhat overestimate the amount of light reaching the semiconductor, and underestimate the efficiency, gives an "internal efficiency" of 2.0%. This is still fairly low compared to the best cells. It does, however, compare reasonably favorably with the best reported conversion efficiency for sputtered material of 4%, which was achieved in a p-n junction cell with much lower transmission losses into the semiconductor.<sup>38</sup> The fill factor of our cell in sunlight (0.59) is typical of the best devices, but both the open circuit voltage,  $V_{oc}$  and the short circuit current,  $I_{sc}$  are considerably lower. The low open circuit voltage as compared to platinum Schottky barrier or p-n junction devices is expected due to the smaller amount of band bending produced by a gold Schottky barrier.<sup>103</sup> In fact, the open circuit voltage is larger than would be expected from the band diagram derived from measurements of the barrier height of the diode and the activation energy of our typical material. The dark band diagram may well not be applicable in amorphous silicon under illumination

since typical light intensities correspond to a high injection condition where the number of photogenerated carriers exceeds the equilibrium carrier density by several orders of magnitude. An "optical doping" effect has been proposed by others due to the preferential trapping of holes.<sup>97,105</sup> See Figures 5.3 and 5.4.

The short circuit current is also expected to be smaller with less band bending due to the reduction in depletion layer thickness. However, since the variation in depletion layer thickness is slower than linear with the band bending and the shortfall in  $I_{sc}$  for our material is greater than the shortfall in  $V_{oc}$ , the rather clear indication is that our material exhibits somewhat poorer generation and/or collection efficiencies than the best sputtered or glow discharge material. Reduced space charge layer thickness, reduced collection from the bulk region or increased recombination within the space charge layer are all possibilities. These three possibilities are pursued further below.

Assuming, as is often done in amorphous silicon cells, that only carriers generated in the space charge layer are collected due to short hole diffusion lengths, allows calculation of a lower limit on cell performance for the case of no recombination in the depletion region. The short circuit current, assuming a depletion layer width  $W$  is then given by

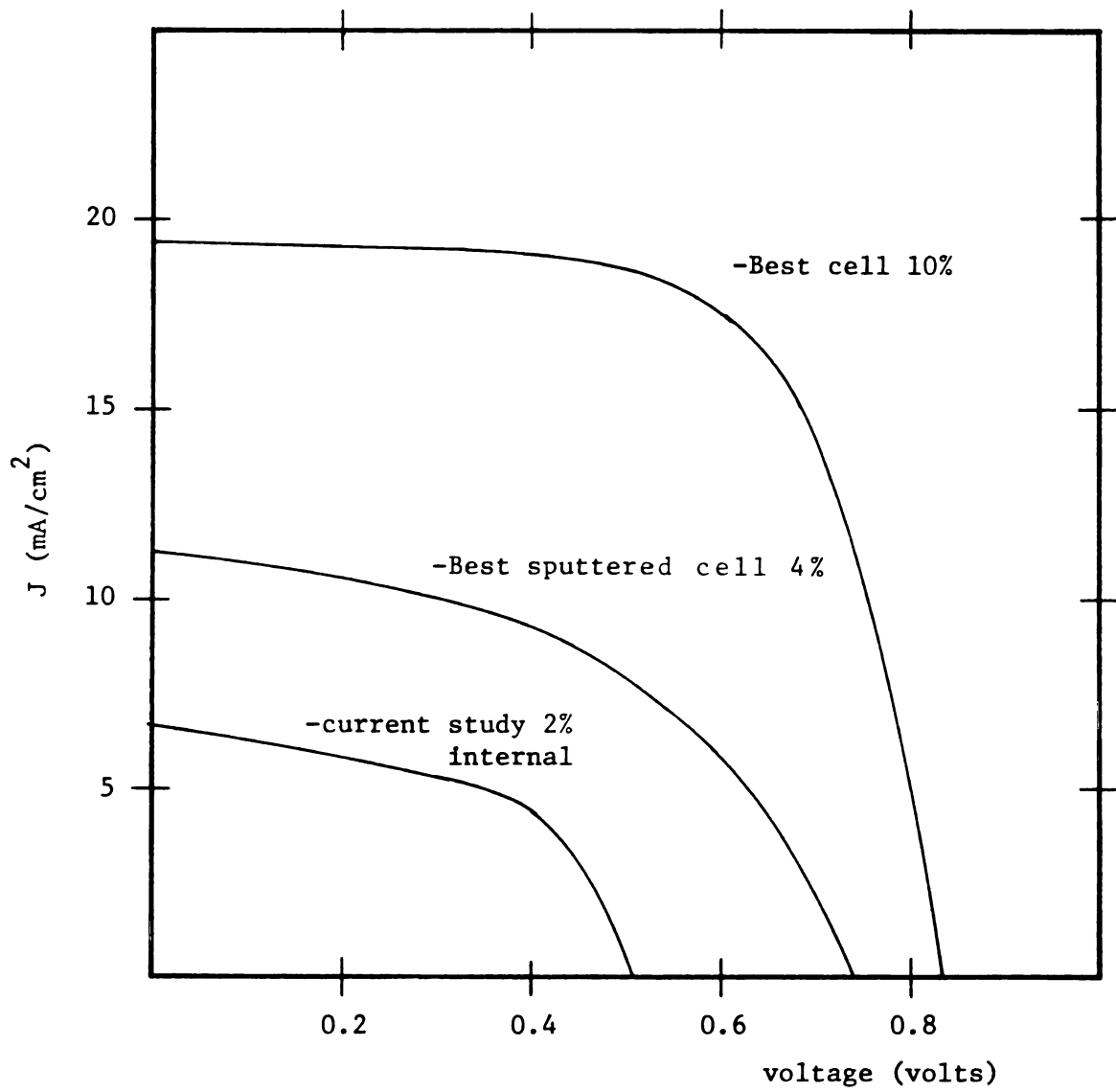


Figure 5.3 Photovoltaic performance comparison.

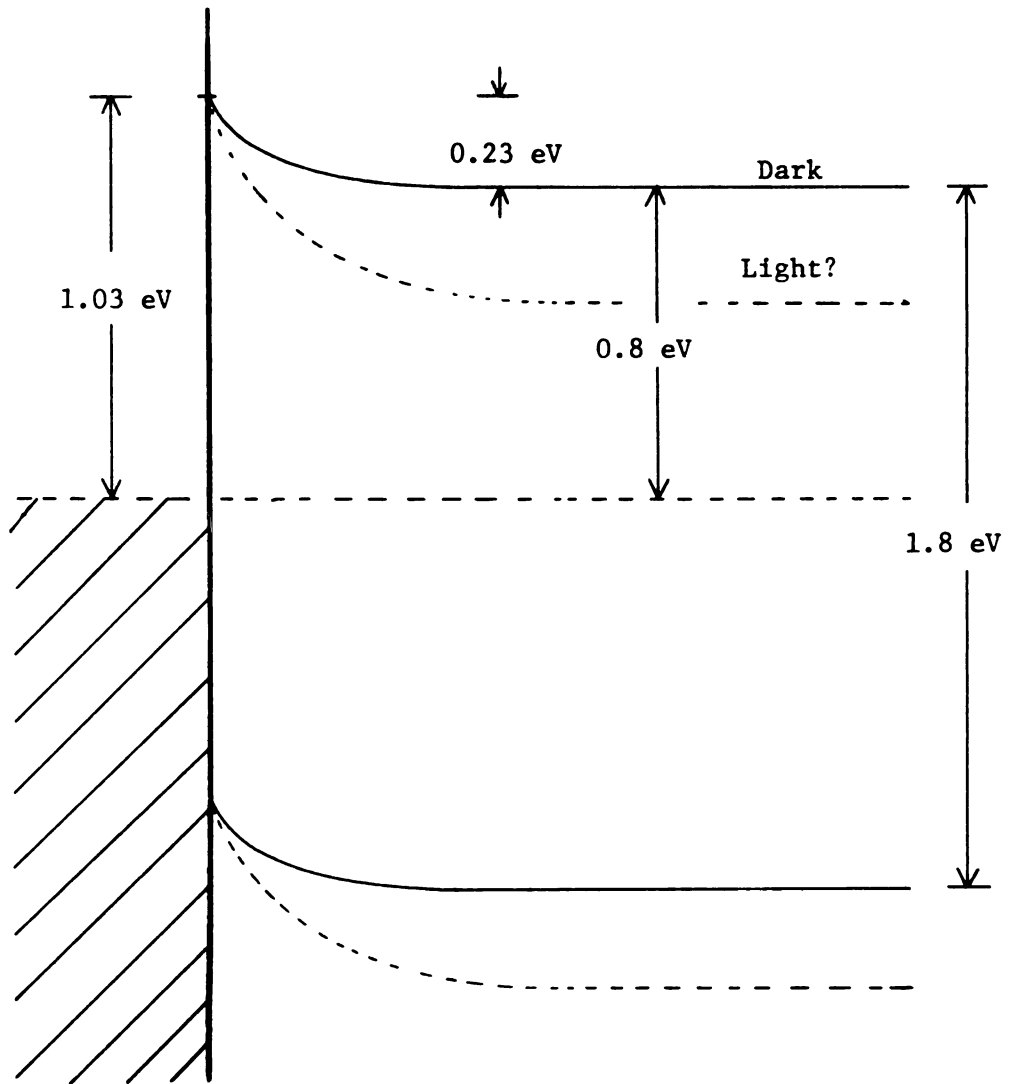


Figure 5.4 Band diagram derived from typical measurements of barrier height and bulk properties .

$$J_{sc} = \int_{\lambda} \exp(-\alpha(\lambda)W) S(\lambda) T(\lambda) d\lambda$$

where  $\alpha(\lambda)$  is the absorption coefficient of amorphous silicon,  $S(\lambda)$  is the spectral distribution of the photon flux in sunlight and  $T(\lambda)$  is the transmittance of the gold top contact. The calculation neglects surface recombination which may be expected to be low due to the high field in the semiconductor at the Schottky contact.

This calculation was performed with measured values of  $\alpha(\lambda)$  and  $T(\lambda)$  corresponding to device ND-74 and with  $S(\lambda)$  for AM2 solar irradiation taken from Hovel.<sup>104</sup> The calculated  $J_{sc}$  values normalized to  $89\text{mW/cm}^2$  East Lansing sunlight at the time of measurement, for space charge layer widths of 3000, 1000 and  $500 \text{ \AA}$  are 3.0, 1.95 and  $1.37 \text{ mA/cm}^2$  respectively. The measured  $J_{sc}$  is only  $1.16 \text{ MA/cm}^2$ , 15% smaller than even the value expected for the very thin  $500 \text{ \AA}$  depletion layer.

It may be argued, however, that the depletion layer is larger than  $500 \text{ \AA}$ . Measurements on similar material produced in this laboratory and others indicate that  $W$  is typically  $2000\text{-}3000 \text{ \AA}$ .<sup>98,105</sup> If  $W$  is indeed this large, recombination in the space charge layer, geminate<sup>71,72</sup> or otherwise,<sup>53,97,98</sup> is a major problem in our material. Thinner devices produced in this

research under the same conditions as devices ND-71 through ND-74 (ND-76 through ND-78) show that the photovoltaic performance is unchanged for  $0.3\mu$  and  $0.4\mu$  devices, but decreases for an  $0.2\mu$  device. This indicates that photogenerated carriers are collected only in the front  $0.3\mu$  of the device. In addition the insensitivity of the fill factor to thickness indicates that the resistivity of the bulk region, which is quite large for the unilluminated diode ( $2 \times 10^7 \Omega$  assuming our device area and bulk properties from coplanar measurements), becomes insignificant under illumination. The lack of variation with thickness of the photovoltaic performance also indicates that the diffusion length for carriers is quite short ( $\leq 2000\text{\AA}$ ), much less than reported for the best device in the literature ( $\sim 10,000\text{\AA}$ ).<sup>9</sup>

In comparison with the best amorphous silicon material (glow discharge), then, we find that our bias sputtered material has two shortcomings. First, there is apparently appreciable recombination in the depletion layer. Secondly, the diffusion length in the bulk material is less. Both of these observations are consistent with an increased density of states in the gap, which act as recombination centers. One might speculate that these same states provide the second conduction path discussed in Chapter IV, however,

we do not have direct evidence for this.

A comparison with the best gold Schottky barrier devices sputtered by a previous researcher, using the same system with a less pure (99.98%) atmosphere reveals that the tungsten light efficiency of the best current devices is improved by 40% over that of the previous devices. (.13% as compared to .09%)<sup>66</sup> The efficiencies are external efficiencies normalized to the 30% gold transmission value quoted in ref. 66. Sunlight efficiencies are not available for the earlier devices.

Another factor limiting efficiencies in our current cell may be unintentional doping of the intrinsic layer by phosphorus impurities left in the sputtering system after the  $n^+$  run. A group at Exxon reports that removing and compensating the phosphorus impurities results in a doubling of the efficiency.<sup>60</sup> We sputter the intrinsic layer immediately after the  $n^+$  layer, the worst case situation reported in reference 60.

### 5.5 Dark I-V Characteristics

A plot of dark current vs voltage reveals a forward characteristic that is exponential at moderate voltages and then increases less rapidly as bulk resistance effects come into play. The reverse current increases much less slowly, but does not saturate. As a function of intrinsic layer thickness, the reverse currents

and low voltage portions of the forward characteristic do not change. This shows that the barrier properties are reproducible from device to device and independent of thickness.

However, at higher voltages the bulk-controlled forward characteristic is seen to increase more rapidly for the thinner devices. The characteristics of 3 devices prepared under the same conditions, but with increasing intrinsic layer thickness are shown in Figure 5.5.

To the extent that our diodes consist of a bulk region and a barrier region, the characteristics of the two parts may be separated. Figure 5.6 is a plot of the logarithm of the device current density vs the logarithm of the bulk voltage. The bulk voltage is taken as the difference of the device voltage and the voltage across the junction at the measured current where the junction characteristics are extrapolated from the linear part of the log J vs V plot.

The bulk current grows linearly with voltage at low voltages and more rapidly at higher voltages, varying as approximately  $V^4$  at the highest measurable current levels. As expected from the device I-V curves, the current in the bulk layer of the thinner device grows rapidly at a lower voltage. These observations are consistent with the bulk resistance remaining at

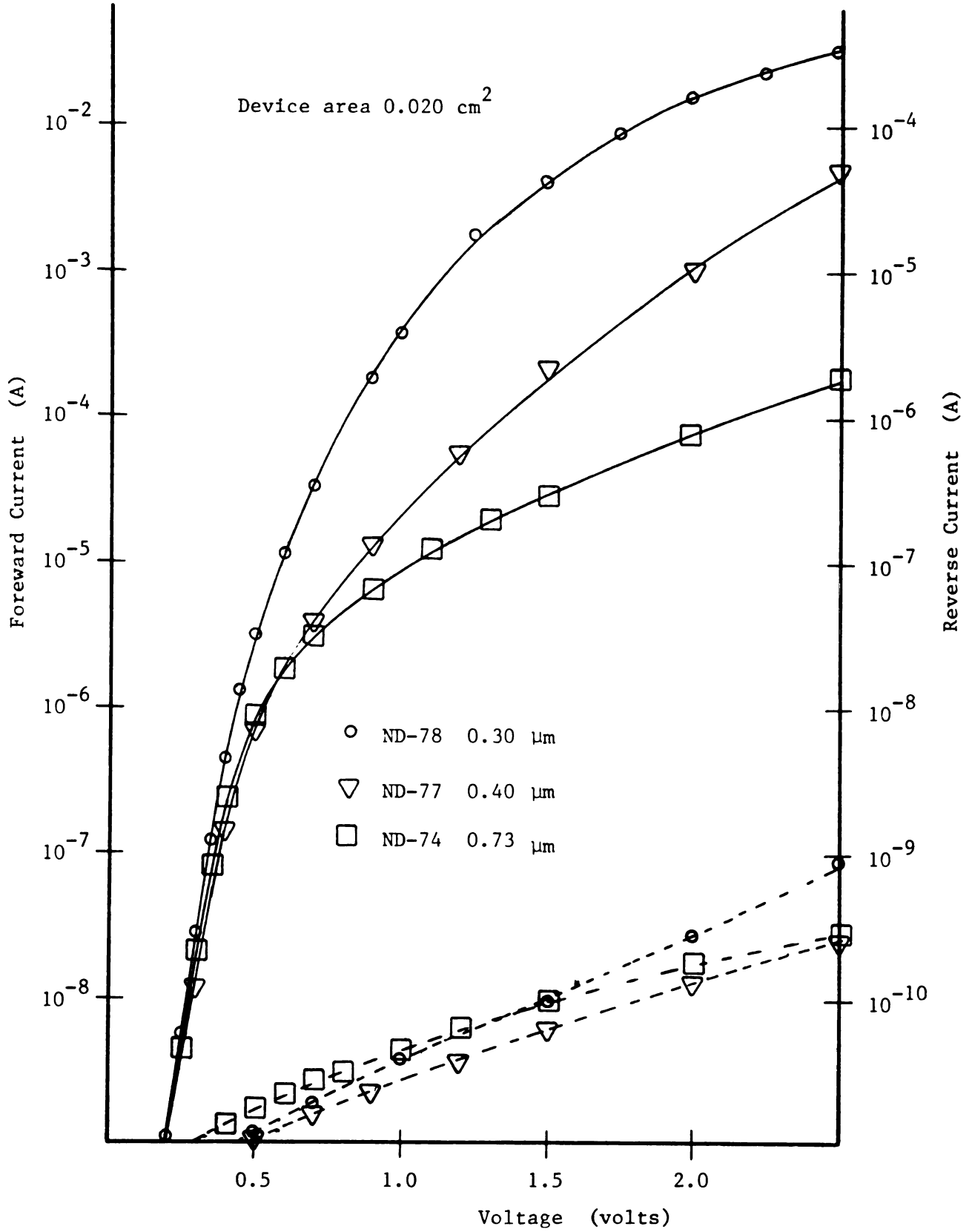


Figure 5.5 I-V characteristics of 3 devices with different intrinsic layer thicknesses.

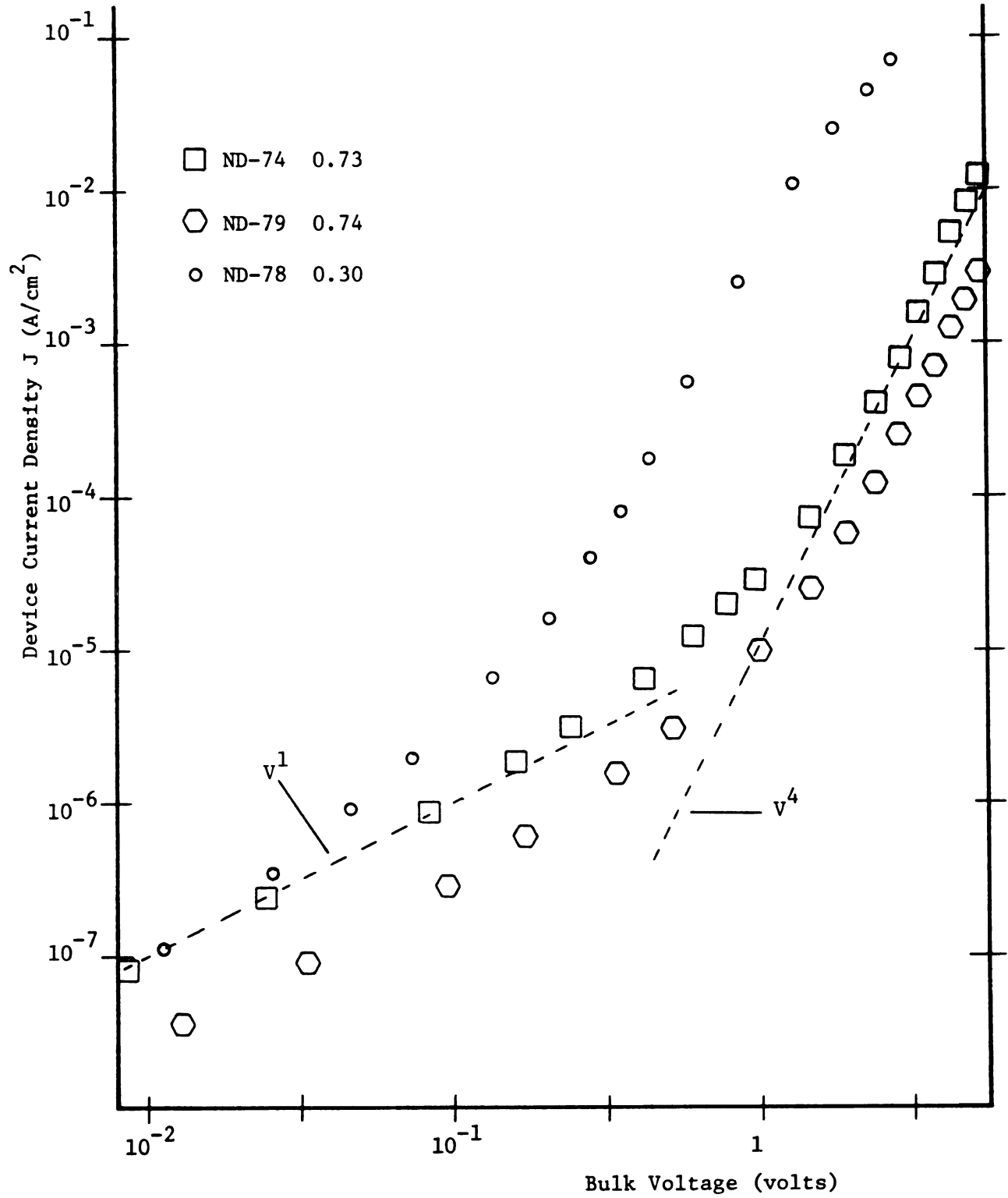


Figure 5.6 Bulk J-V characteristics.

its equilibrium value at low electric fields and decreasing due to electron injection from the  $n^+$  contact at higher voltages. Similar behavior of the intrinsic region has been reported by a group at the University of Dundee in  $n^+$  - intrinsic- $n^+$  structures.<sup>28</sup> Another group reports space charge limited forward currents in Schottky diodes of structure similar to ours.<sup>96</sup> These results are in substantial agreement with ours in that a linear region is seen followed at higher voltages by a region where the exponent in the relation  $I \propto V^\beta$  increases from one to about 5. Reference 28 describes the critical dependence of the I-V characteristic on the density of states in the gap, and uses that relationship to derive a density of states in good agreement with other measurements. The injection phenomenon observed in the current devices is in sharp contrast to the situation observed in Schottky barrier devices made in this laboratory, using an unhydrogenated rather than  $n^+$  contact layer, where injection effects were not seen.<sup>66,98</sup> For the unhydrogenated contact layer devices, the characteristics were well modeled by an exponential junction in series with a linear bulk resistance.

Assuming a depletion layer thickness of  $2000\text{\AA}$ , the bulk conductivity for ND-74, as derived from the linear part of the bulk characteristic is  $2.67 \times 10^{-8}$ ,

which is larger than a typical coplanar resistivity by a factor of 100 to 1000. This discrepancy is believed to be due to unintentional doping effects attributable to contamination from phosphorus dopants left in the system after deposition of the  $n^+$  layer. A similar phenomenon is described in references 28 and 60.

The increased conductivity corresponds to a shift in the Fermi level from its undoped position about 0.8 eV below the conduction band to a position about 0.67 eV below the conduction band, assuming otherwise constant material properties. This amount of shift is consistent with the postulated phosphorus doping.<sup>16</sup>

The rectification ratio, defined as the ratio of the forward current to the reverse current at a specified voltage is a figure of merit often used to compare the performance of diodes.

$$RR = I_F/I_R \text{ at } V_{RR}$$

Values of rectification ratio reported for amorphous silicon Schottky barriers and p-n junctions range greatly from 10 or less up to  $3 \times 10^7$  at  $V_{RR} = 0.5V$ .<sup>44,52,54,59,98,107</sup> The largest value reported in the literature is for a gold-amorphous silicon Schottky barrier on glow discharge material. Our best rectification ratio at 0.5 V was  $10^6$ , higher than most reports in the literature for either Schottky barrier or p-n

junction diodes. For an ideal diode, at voltages greater than a few  $kT$ , the rectification ratio is given by the ratio of the forward current to the reverse current.

$$\frac{I_F}{I_R} = \frac{I_o e^{(qV/kT)}}{I_o} = e^{qV/kT}$$

At 0.5 volts and  $300^\circ K$  the ideal RR is  $2.5 \times 10^8$ , considerably larger than the values normally observed.

A more realistic model for our diode describes the forward current at voltages greater than a few  $kT$  as

$$I_F = I_o e^{qV/nkT}$$

The ideality factor,  $n$ , takes into account the variation of barrier height with applied voltage due to image force lowering and interfacial oxide layer effects. Values of  $n$  derived from the straight portion of the I-V characteristic for our diodes range between 1.16 and 1.32. The value of  $n$  of 1.16 corresponds to the diode with the best rectification ratio, which is not surprising since these non-ideal effects tend to reduce the forward current and increase the reverse current.<sup>100</sup>

At negative applied voltages the effect of image force lowering and interfacial oxide effects is to reduce the barrier height as the field near the

metal-semiconductor interface,  $E_{\max}$ , increases. In addition  $E_{\max}$  appears in the expression for the current density predicted by the diffusion theory. These effects all lead to a current which does not saturate at some  $J_0$  in the reverse direction, but continues to increase at increasing reverse bias. In addition, tunneling through the barrier can be important, especially at the edge of the metal contact. The predominant voltage dependence of each mechanism is as follows.<sup>100</sup>

Image force	$J \propto e^{V^{3/4}/C}$
Interface Layer	$J \propto e^{V^{3/2}/C}$
Diffusion Theory	$J \propto V^{3/2}$
Tunneling	$J \propto e^{V/C}$

A plot of  $\log J$  vs  $V^{1/2}$  (Figure 5.7) gives a straight line at large ( $>1V$ ) reverse biases for a number of our diodes. To the extent that the functional dependences on voltage are correct for amorphous silicon with its continuous distribution of gap states, this suggests that the interface layer plays an important role in determining the I-V characteristics. Since the silicon film was exposed to air before the gold evaporation, an interfacial oxide layer is indeed expected.

A plot of the actual I-V characteristics of our highest rectification diode vs those for an ideal diode with the same saturation current are shown in Figure 5.8.

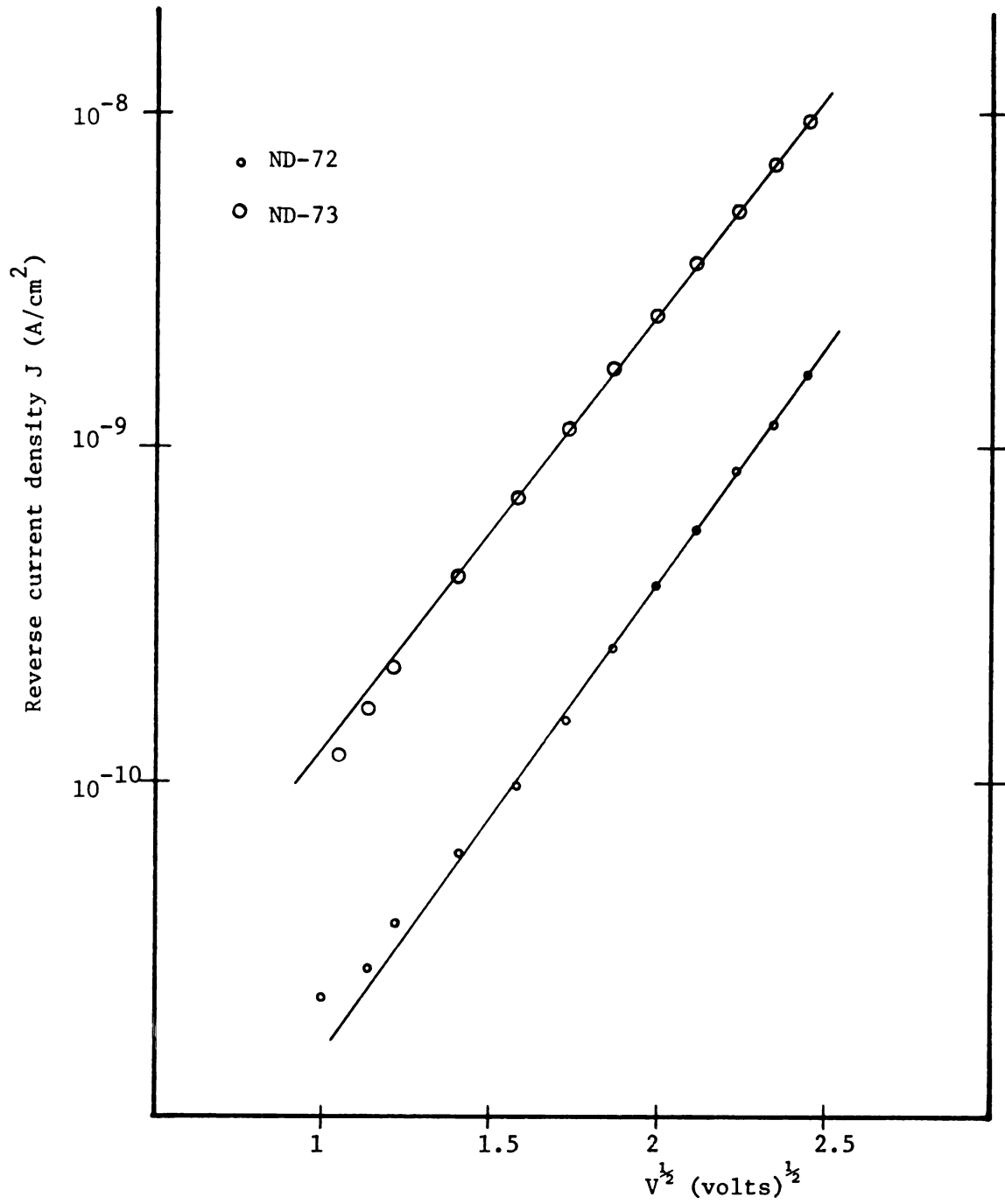


Figure 5.7 Reverse characteristics,  $\text{Log } J$  vs  $V^{1/2}$ .

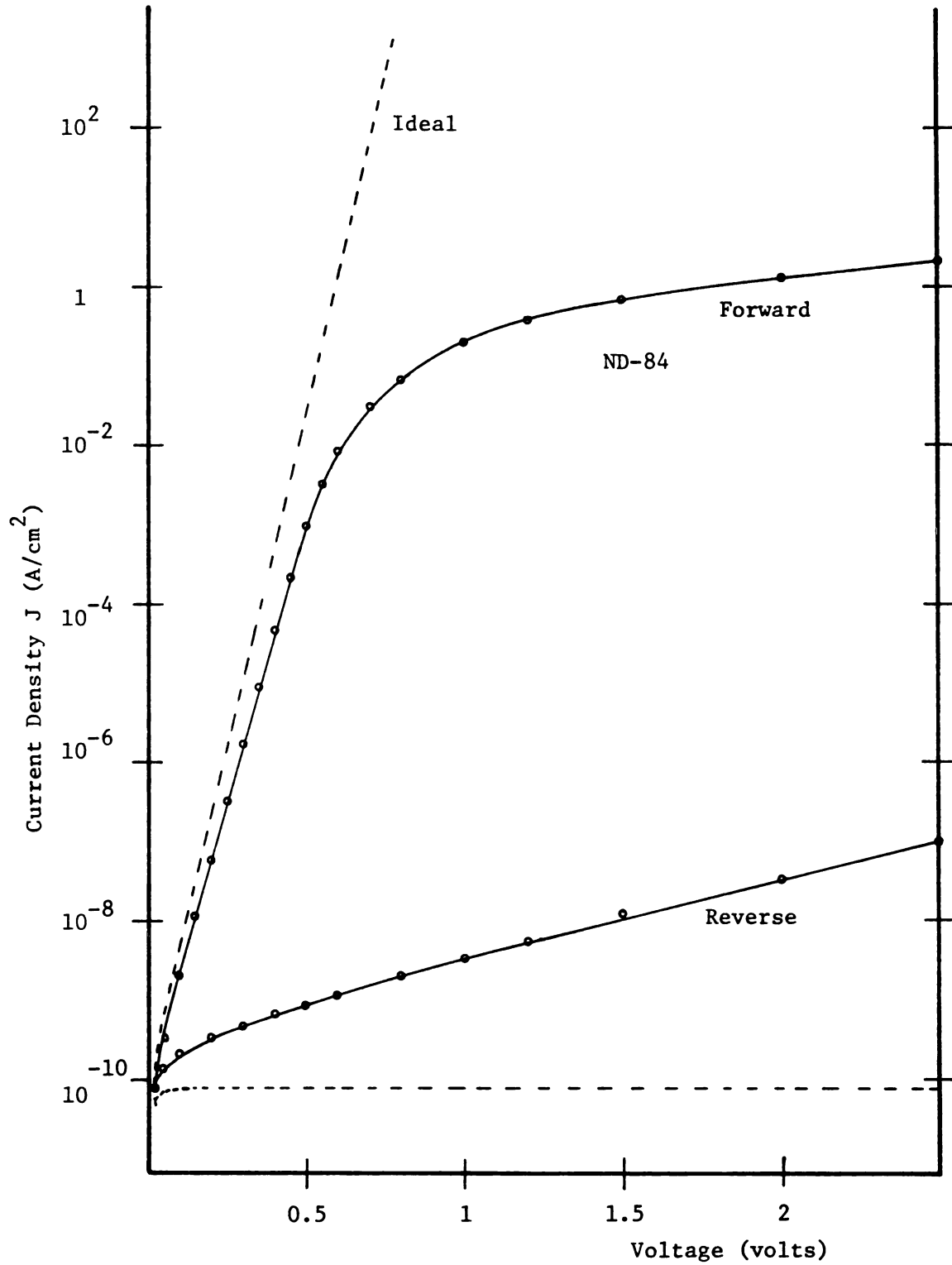


Figure 5.8 J-V plots for ND-84 and ideal with the same saturation current.

The forward current is seen to be reduced by the ideality factor effect at low voltages, and then even more by the bulk series resistance effect described earlier at higher voltages. Significantly, the devices exhibiting the highest rectification ratios were fairly thin, minimizing the bulk resistance effect. The reverse current is seen to greatly exceed the saturation current.

## 5.6 Conclusions

Schottky barrier measurements support the view that, although our material has not been optimized, we are working with device quality material, which is representative of recent sputtered material reported in the literature. Our films are deposited in a sputtering system which has a target size and a target voltage which are smaller and larger respectively than those used to fabricate the best reported sputtered material. Therefore substrate bombardment due to target voltage is relatively higher in our system, for a given deposition rate and apparently of some detriment from a photovoltaic point of view. Comparison of the measured photovoltaic performance of the material with theory leads to the conclusion that the photovoltaic performance in our Schottky barrier diodes is probably limited by recombination in the depletion layer. In addition

the overall collection width is fairly small,  $\lesssim 3,000\text{\AA}$  and the diffusion length for minority carriers is less than in the best glow discharge material. However, our gold Schottky barrier diodes do show excellent rectification characteristics, comparable to, but slightly less than for the best amorphous silicon based devices reported.

Both of these limitations point to an appreciable number of recombination centers, or states in the gap. The second bulk conduction path identified in Chapter IV is also due to states in the gap. A hypothesis is that in both cases, overly energetic substrate bombardment is the cause.

The forward current of the diodes for  $V \gtrsim .4$  V is limited by a bulk series resistance whose value is determined by injection effects at high forward biases. The injection effect takes place at lower voltages for thinner bulk regions and is dependant on the presence of an injecting bulk contact. The conductivity of the bulk layer at low forward biases suggests that the nominally intrinsic layer is actually lightly doped with phosphorus remaining in the sputtering chamber after the  $n^+$  layer deposition.

The barrier height measurement, in conjunction with the dark activation energy measurement, leads to a band diagram which is not consistent with the

observed open circuit voltages. A similar discrepancy has been observed by others.<sup>98,106</sup> A change in the position of the Fermi level with respect to the conduction band under illumination is possible due to the large number of photogenerated carriers.

## CHAPTER VI

### SUMMARY, CONCLUSIONS AND RECOMMENDATIONS

The main objective of this research has been to determine the effect of substrate bias on the properties of sputtered hydrogenated amorphous silicon. In addition, the effect of target voltage on film properties and the dependence of Schottky barrier device properties on undoped layer thickness have been investigated more briefly. In a more fundamental sense the motivation of this research has been to gain insights as to how to produce better amorphous silicon, due to its probable utility in large area photovoltaics. Specifically, a goal has been to add to the identification of deposition parameters which are important in determining the film properties, since if this can be done work toward producing better amorphous silicon will proceed with more direction and more quickly.

The deposition techniques used to produce the films in this study as well as the measurements used to characterize them are discussed in detail in Chapter III. The purity of the sputtering atmosphere, which is known to be an important factor in producing good amorphous silicon is estimated to be 99.99% and

other sources of impurities are indicated. The experimental procedures for determining the optical and electrical properties of the semiconductor film are analyzed in terms of the relevant background theory and experimental errors.

Chapter IV reports the primary results of this research. The electrical properties of hydrogenated amorphous silicon are found to be sensitive to substrate bias to a greater or lesser extent depending on the amount of substrate bombardment attributable to high energy particles from the vicinity of the target. Increasing substrate bias is seen to result in an increased conductivity activation energy and a decreased photoconductivity. The effect is strongest for samples sputtered at a low target voltage, where an increase in substrate bias from 31 to 106 volts results in a decrease in the photoconductivity by a factor of 1000. At a higher target voltage a substrate bias effect is seen only at substrate biases greater than 70V, where an order of magnitude decrease in photoconductivity is seen as the bias voltage increases to 130V. The decrease in photoconductivity is correlated with an increase in the conductivity activation energy at low substrate biases.

At high substrate bias the mechanism for the change in film properties is modeled as a two path conductivity

in the material. One path, which to a first approximation does not change with the deposition parameters, is conduction in extended states above the mobility edge. The other path, conduction by hopping in a band of localized states 0.38eV below the mobility edge, is enhanced at high bias levels. The optical properties of the amorphous silicon films do not change appreciably over the whole range of substrate bias, indicating that no major changes in void fraction or hydrogen content occur due to the increased level of bombardment.

Schottky barrier device properties are examined in Chapter V, at two bias levels and over a range of thicknesses. The results at high target voltage and low substrate bias are in agreement with the results in Chapter IV in that substrate bias effects are masked at high target voltages. The Schottky barrier properties as a function of thickness, along with measurements of the conversion efficiency of our cells, suggest that recombination of carriers in the space charge layer and the limited diffusion length of minority carriers limit the photovoltaic performance of our material. One may speculate that the gap states causing recombination and limited diffusion lengths are also the states causing hopping conduction and are due, therefore, to overly energetic substrate bombardment. Target voltages

greater than  $\sim 1,000\text{V}$  or substrate biases greater than  $\sim 100\text{V}$  appear to cause damaged material. A lower target voltage system is predicted to yield better sputtered amorphous silicon.

The actual damage mechanism, for example increased argon incorporation or an increased number of broken bonds, was not investigated. Neither was a quantitative assessment of the density of gap states attempted, both deemed beyond the scope of this study.

The dark characteristics of the Schottky barrier diodes yield rectification ratios of up to  $10^6$  at 0.5 volts and up to nearly  $10^8$  at higher voltages. The forward current is determined by the barrier characteristics at low forward currents and by bulk resistance effects at higher currents. The resistivity of the bulk decreases with increasing forward bias or decreasing thickness due to injection of carriers from the  $n^+$  back contact, an effect which is not seen in similar diodes constructed with an unhydrogenated layer contact. In addition, the resistivity of the device material indicates probable unintentional doping of the nominally intrinsic layer by phosphorus remaining in the sputtering chamber after deposition of the phosphorus doped  $n^+$  contact.

The principal conclusion of this research is that bombardment effects, both substrate bias induced

and target voltage controlled, appear to be important in determining the properties of hydrogenated sputtered amorphous silicon. Although, as indicated by this research, these are important deposition parameters, the optimum amount and type of bombardment to produce the best sputtered amorphous silicon has not yet been determined. More work on the subject is certainly needed and may be the most fruitful path toward improving the sputtered material. Specifically, the effect of target voltage on the properties of amorphous silicon sputtered under otherwise nearly optimum conditions appears to be an important experiment for future research. In addition the effect of substrate bias should be studied at much lower target voltages.

Ideally, to isolate target voltage effects in the proposed experiment, all other deposition variables would be held constant. These should include the deposition rate and the properties of the plasma in contact with the growing film. These conditions could perhaps be achieved either in a triode sputtering system, which decouples discharge current and voltage, or in a more standard sputtering system if the density of the plasma in the vicinity of the substrate could be independantly controlled. A possibility for this control is auxiliary microwave excitation of the plasma, the goal being that as the target voltage is varied,

the properties of the plasma in contact with the growing film are held constant. Low target voltages are achievable to a certain extent by increasing the target size, but a wider range of target voltages (especially low target voltages) becomes available with the use of either a triode system or a magnetron target.

Another question related to substrate bombardment is as to the effect of the plasma in contact with the growing film. Again the sputtering system with a microwave supported plasma would be useful. The characteristics of the plasma in contact with the new substrate could be varied independently of the other sputtering parameters. Another cruder method would be to simply surround the substrate with a grid which would pass the neutral sputtered atoms, but screen out the plasma.

Finally, it is noted that many of the bombardment effects investigated in this work are largely absent in glow discharge material. One may speculate that the absence of overly energetic substrate bombardment is a key to understanding the general superiority of glow discharge amorphous silicon over sputtered amorphous silicon.

## APPENDICES

## APPENDIX A

### Details of Film Deposition

To fabricate a coplanar sample, a clean substrate is mounted on the substrate holder, and the vacuum system is sealed. Following this the sputtering chamber is outgassed overnight (typically 15 hr) with the substrate heater on and the chamber heated to 100°C with an external resistance heater. Prior to sputtering, the chamber is allowed to cool and the leak/outgassing test discussed in section 3.2.2 is performed.

If the leak rate is found to be satisfactory, the sputtering gasses are admitted to the chamber through the flow system. The standard mixture for all hydrogenated amorphous silicon films was 1.25 sccm argon and .76 sccm hydrogen, resulting in partial pressures of 7.5 and .55 millitorr respectively.

Sputtering commences with the application of sufficient rf power to achieve the desired target voltage. This turns out to be about 43 watts for the large target and 75 watts for the small target. The target is sputter cleaned for 10 minutes to remove any oxide layer or adsorbed gasses before the substrate is unshuttered and deposition begins. At the end

of the run, the rf generator, substrate heater and gas valves are all shut off and the sample is allowed to cool.

Upon cooling, the chamber is brought up to atmospheric pressure with argon, then opened. The sample is mounted (in air) with the appropriate mask for the evaporation of contacts. The .1 micron thick contacts are deposited by thermal evaporation of aluminum from a tungsten coil after the pressure in the bell jar has fallen below  $3 \times 10^{-6}$  torr. After a period of cooling the sample is removed and tested.

The procedure for the deposition of the Schottky barrier samples involves a few additional steps. The substrate is first coated with molybdenum sputtered in argon at a flow rate of 2.1 sccm, giving a sputtering pressure of 12.5 millitorr. Outgassing before the molybdenum run is normally omitted, since film purity is not as important as for the silicon films. Most runs were preceded by an overnight pump down, however. After the molybdenum contact is deposited the system is pressurized with argon, opened, and the molybdenum target is exchanged for a silicon wafer. The outgassing and leak testing then proceed as for the coplanar sample.

The next layer deposited is the  $n^+$  contact layer. In this case 1.25 sccm argon and .78 sccm of a 2.82%

phosphine in hydrogen mixture are fed into the chamber, resulting in partial pressures of 7.5 millitorr argon, .55 millitorr hydrogen and .09 millitorr phosphine. The phosphine partial pressure is estimated from the observed dependence of pumping speed on molecular weight.

Once the flows have reached equilibrium, the target is sputter cleaned as before. After 10 minutes the substrate is unshuttered and sputtering is continued for 30 minutes resulting in a .12 micron  $n^+$  layer. Following 40 minutes of pumping to remove phosphine from the chamber and gas lines, the undoped layer is deposited to the desired thickness as described before. The sample is then allowed to cool, removed from the sputtering chamber, masked and transferred to the CVC evaporator. Gold is thermally evaporated from a tungsten boat to form Schottky barrier contacts and the devices are ready for testing.

## APPENDIX B

### MEASUREMENT OF INDEX OF REFRACTION AND THICKNESS

The index of refraction measurement described in chapter three depends on the film being transparent, uniform in thickness and on the light being monochromatic. In addition light reflected from the back surface of the substrate must be included in the calculations and while the thickness does not enter into the calculation, constraints on spectral purity are more stringent for thicker films. It is essential also, that the measurement be made at a maximum in the reflectance,  $R(\lambda) = (\text{reflected intensity/reference intensity})$  or at a minimum in transmittance,  $T(\lambda) = \text{transmitted intensity/reference intensity}$ .

From all indications, the film is locally uniform in thickness and transparent at wavelengths greater than about  $.8\mu$ . The measured thickness varies only in a slow, regular manner as the small measuring beam is moved and, as is indicative of smoothness on a microscopic scale, the film does not scatter light and appears featureless through optical and scanning electron microscopes. For wavelengths greater than  $.8\mu$ ,  $T(\lambda)$  and  $R(\lambda)$  add to 1 to within the accuracy

of the measurement indicating that the film is indeed transparent.

An important question to answer is: Is the light sufficiently monochromatic? The Bausch & Lomb High Intensity Grating Monochromater used in this research may be fitted with slits of various widths trading off intensity against spectral purity. Additionally, a certain amount of light is scattered by the grating, typically .1%. The grating-slit combination used in measuring the index of refraction and thickness passes a band of wavelengths 19.2 nm wide, centered about the desired wavelength. The intensity is greatest at the center wavelength and falls off linearly to zero at the cutoff wavelengths. See Figure B1.

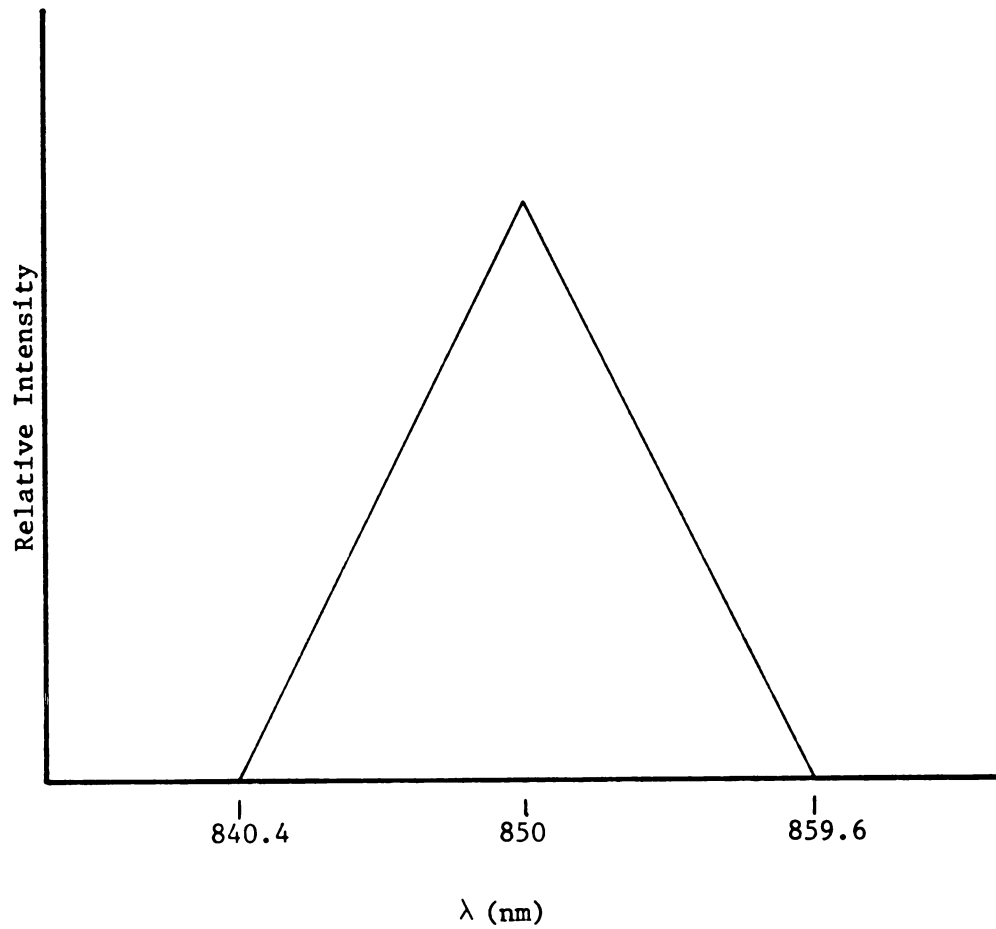
Ignoring the contribution from the back of the substrate for the moment, the reflectance from a film is given by

$$R(\delta) = \frac{r_1^2 + 2r_1r_2\cos 2\delta + r_2^2}{1 + 2r_1r_2\cos 2\delta + r_1^2 r_2^2}$$

where  $r_1$  and  $r_2$  are the Fresnel coefficients

$$r_1 = \frac{n_0 - n_1}{n_0 + n_1}, \quad r_2 = \frac{n_1 - n_2}{n_1 + n_2}$$

and  $n_0$ ,  $n_1$  and  $n_2$  are the indices of refraction of air, the film and the substrate respectively.<sup>63</sup>



(a)

air	n=1.003
amorphous silicon	n=3.48
glass	n=1.53

(b)

Figure B 1 (a) Monochromator output vs wavelength.  
(b) Optical sample.

Figure B2 shows the reflectance vs  $\delta$  for the 6th order maximum for a film of index 3.48 on a substrate of index 1.53. These numbers are typical of index measurements of  $.7\mu$  thick amorphous silicon films.  $\delta$  is the phase shift of light traversing the film and  $d_1$  is the thickness of the silicon layer.

$$\delta = \frac{2\pi}{\lambda} n_1 d_1$$

Also plotted in figure B2 is the intensity vs  $\delta$  corresponding to the 19.2 nm bandwidth of the monochromator. The intensity,  $I(\delta)$  is approximated as linear since although  $\delta \propto \frac{1}{\lambda}$  the bandwidth is quite small in comparison with the center wavelength.

To evaluate the effect of the finite range of wavelengths on the index of refraction measurement, the weighted average of the reflectance at each wavelength is compared with the reflectance expected at the maximum. First  $I(\lambda)$  is normalized, that is it is required that

$$1 = \int_{\delta_{\min}}^{\delta_{\max}} I(\delta) d\delta$$

Then this function is multiplied by  $R(\delta)$  and integrated with respect to  $\delta$ .



$$R' = \int_{\delta_{\min}}^{\delta_{\max}} I(\delta)R(\delta)d\delta$$

The result is the reflectance expected with the 19.2 nm bandwidth of the monochrometer. This reflectance turns out to be only slightly different than the reflectance computed for the center wavelength.

$R_{\text{center}}$	= .60141	index = 3.479
$R'_{19.2}$	= .59997	index = 3.471
	-0.24% change in R	-0.23% change in calculated index

A related error may be expected if the center wavelength is not set precisely. Ideally, determination of the proper wavelength setting would be merely a matter of turning the wavelength dial and observing a maximum in reflected light. However, the monochrometer output-cell sensitivity function varies with wavelength, so really a maximum in  $R(\lambda) =$  (reflected intensity/reference intensity) should be found. Practically, the reflectance maximum was found by bracketing it by the unnormalized maximum in reflected light and minimum in transmitted light, which appear on opposite sides of the true maximum. The center wavelength was then taken as the average of these two values.

The difference in wavelength between the apparent

minimum in transmitted light and the apparent maximum in reflected light is almost always less than 12 nm. Since approximately 40% of the incident light is transmitted and 60% is reflected, the true reflectance maximum should lie near the center of the range. Additionally, there is some uncertainty in locating the apparent maxima and minima, and a repeatability uncertainty in the grating of 1nm, leading to a total uncertainty of about  $\pm 6$ nm in setting the wavelength at the desired value. By the same process described earlier, using the intensity function centered 6nm from the true maximum in reflection, the reflectance is found to be underestimated by 0.82% leading to an error in the computed index of -0.79%. Thus in this measurement the finite bandwidth of the monochromator and center wavelength errors combine to underestimate the index by 0.23% to 0.79%.

In addition to these two errors the specifications for the monochromator state that the light output typically includes 0.25% scattered light. The average reflectivity for all wavelengths of light near the measurement wavelength is about 0.38, so if the reflectance for monochromatic light is 0.60, the observed reflectance will be somewhat less.

$$R_{\text{obs}} = 0.6(0.9975) + 0.38(0.0025) = 0.59945$$

leading to an insignificant 0.09% underestimation of the reflectance and index.

A somewhat more significant source of uncertainty is the finite accuracy of the reflectance and transmittance measurements. The accuracy of the lock-in amplifier (Model HR-8 Princeton Applied Research) is specified as 1%. In addition the light source may vary slightly between measurements and cell placement differences may contribute a small amount of error. Assuming a transparent film, reflectance measurements may be derived from transmission or reflection readings. In fact, both were used, and were averaged to obtain the reflectance used to calculate the index. The two values rarely differed by more than 2% corresponding to approximately a 2% uncertainty in the computed index.

The transmittance and reflectance measurements were made with the sample tilted 5-10° with respect to the incident light. This might be expected to change the reflectivity used to compute the index somewhat. In this case the equation for R in terms of the Fresnel coefficients is the same as for the case of normal incidence, but the expressions for the Fresnel coefficients themselves are more complex, depending on the angle of incidence and the plane of polarization.<sup>63</sup> The reflectance turns out to be 2% greater for light polarized with the electric vector perpendicular to

the plane of incidence than for light polarized with the electric vector parallel to the plane of incidence. When the two reflectances are averaged, however, an insignificant 0.009% decrease in R at a maximum is expected for a 10° sample tilt and an even smaller 0.005% decrease is calculated for a 5° tilt.

Light is also reflected from the back of the substrate after passing through the film. Some of this light is again transmitted by the film and results in an apparent increase in the reflectivity. The measured reflectivity is corrected for this effect based on several assumptions. First, that the light reflected from the back is not sufficiently monochromatic to produce interference effects over the width of the substrate, second, normal incidence which as before has only a small effect on the results and third, that the second reflection of light from the back of the substrate is insignificant. These assumptions are justified below.

Using the equation for R from a film given earlier, it can be seen that adjacent maxima in the reflected intensity are spaced  $\pi$  radians apart in  $\delta$ . The thickness of the substrate is 0.048" inches or 1219  $\mu$ . The spacing in wavelength of maxima due to .85 $\mu$  light reflected from the back of the substrate may be computed from the equation for  $\delta$ .

$$\delta = \frac{2\pi}{\lambda} n_1 d_1 \quad \text{or} \quad \lambda = \frac{2\pi}{\delta} n_1 d_1$$

$$\delta_1 = 13,786 \quad \lambda = 0.850035\mu$$

$$\delta_2 = 13,786 + \pi \quad \lambda = 0.849841\mu$$

The wavelength spacing of 0.19 nm implies that approximately 100 oscillations of the reflectance occur within the 19.2 nm bandwidth of the monochrometer and indeed no rapidly oscillating interference phenomenon is observed--the light indeed behaves incoherently. The observed reflectivity is predicted by

$$R_{\text{obs}} = R + R_g(1-R)^2$$

where  $R_g$  is the reflection of the glass at the back surface,  $R$  is the reflectance of the air-Si-glass structure and  $R_{\text{obs}}$  is the apparent (measured) reflectivity, including the contribution from the back of the substrate. See Figure B3. Starting with unit incident intensity, at a maximum in  $R$ , the film will pass an intensity of  $(1-R)$ , about 0.4, into the glass. After reflection from the back surface the intensity falls to  $R_g(1-R)$ , approximately 0.017. What light is transmitted through the film again, to add to the light reflected directly from the front film, has an intensity of  $R_g(1-R)^2$  or 0.0068, about 1.1% of the intensity of light reflected directly from the film. The second reflection of light

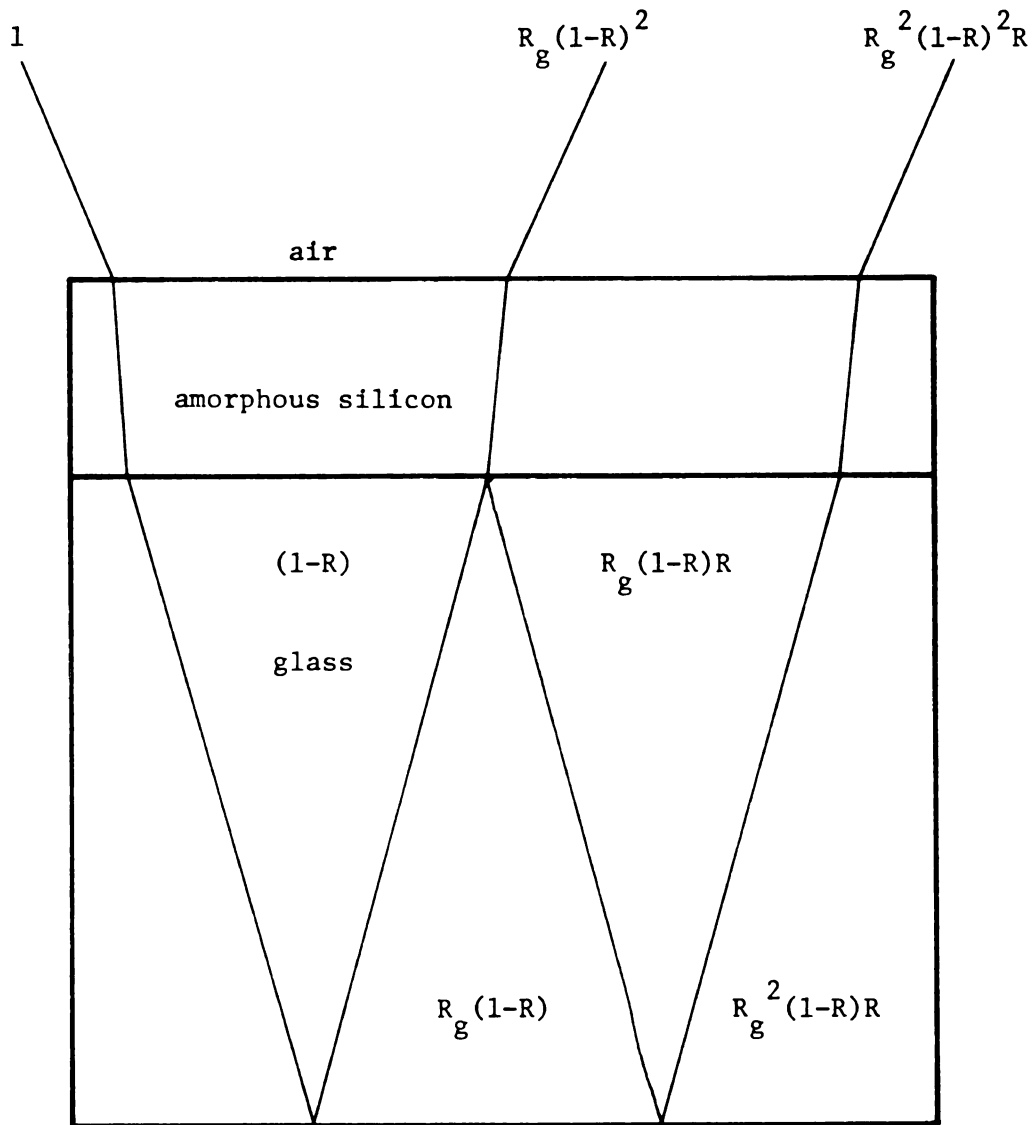


Figure B 3 Back reflection diagram.

will have an intensity of  $R_g^2(1-R)^2R$ , only 0.000176, entirely negligible in this measurement.

Thus the various deviations from the simplest theory may be summarized as follows:

Source	Index Error
Finite accuracy measuring R	±2%
Finite bandwidth/maximum location	-.23% to -.79%
Scattered light	-.04%
10° substrate tilt	-.009%
Back of substrate	1.1% <u>correction</u>

The contribution from the back of the substrate represents a correction rather than an error, so the total error in measuring the index is less than about ±3%.

It should be noted that this estimate is for a typical film deposited over the course of this research and, for example, finite bandwidth effects become much more important for thicker films (like the substrate!) or if one is measuring R at a minimum, where  $R(\delta)$  is smaller and has a larger curvature.

As with most materials, the index of hydrogenated amorphous silicon varies considerably with photon energy. The measured values of refractive index were fitted to the Wemple-Di Domenico dispersion equation.<sup>64</sup>

$$n^2(E) = 1 + E_0 E_d (E_0^2 - E^2)^{-1}$$

Values of 3.699 and 34.681 for  $E_o$  and  $E_d$  fit the measured index values for nearly all samples to within experimental error. These values are very close to those obtained in reference 64 for similar material.

Once the index is known, the thickness is determined by observation of minima in  $R(\lambda)$  as described in Chapter 3. The above equation is used to interpolate between measured indices, or for a substantial number of the samples, is used with the values of  $E_o$  and  $E_d$  above to predict the index without measurement, since no index variation is observed.

Uncertainty, in addition to the  $\pm 3\%$  index error, enters the thickness measurement in finding the wavelengths at which minima in  $R(\lambda)$  occur. The minima are considerably sharper than the maxima, so slowly changing light output-detector response problems are not as important. The minima can be located to within about 4 nm at 850 nm and the wavelength accuracy of the grating is  $\pm 4$  nm, giving a total uncertainty in the position of the minimum of  $\pm 8$  nm. Since the thickness is proportional to the wave length, the thickness inaccuracy from this source is about  $\pm 1\%$ .

The error in thickness due to the  $10^\circ$  substrate angle should also be considered. The phase shift for light crossing the film twice is  $2\delta$ . For light incident at an angle  $\phi_o$  with respect to the normal and

refracted at  $\phi_1$ ,  $\delta$  is given by

$$\delta = \frac{2\pi}{\lambda} n_1 d_1 \cos\phi_1$$

At a substrate angle of  $10^\circ$ ,  $\phi_1 = 2.86^\circ$ . Since the thickness is proportional to  $\delta$ , this results in an insignificant apparent thickness error of 0.12% due to the cosine term.

Thus the total uncertainty in this thickness measurement is  $\pm 4\%$ , mostly due to the 3% uncertainty in the index of refraction. Assuming the index to be uniform over a sample, relative thicknesses at various points may be measured to a 1% accuracy.

## APPENDIX C

### DETERMINATION OF THE OPTICAL ABSORPTION COEFFICIENT

It is desired to relate the intensities of light reflected from and transmitted through an amorphous silicon film to the optical absorption coefficient  $\alpha$ . As light passes through the film, the intensity decreases as  $I(x) = I_0 e^{-\alpha x}$ . In addition light is reflected at the film boundaries and at the back surface of the substrate. See Figure C1. For a normally incident field of unit amplitude, a development by Heavens<sup>63</sup> gives the amplitudes of the reflected and transmitted fields  $R_E$  and  $T_E$  respectively in terms of the Fresnel coefficients and  $\delta$ , which describes propagation in the film.

$$R_E = r_1 + \frac{t_1 t_1' r_2 e^{-2i\delta}}{1 + r_1 r_2 e^{-2i\delta}}$$

$$T_E = \frac{t_1 t_2 e^{-i\delta}}{1 + r_1 r_2 e^{-2i\delta}}$$

where

$$t_1 = \frac{2n_o}{n_o + n_1} \quad \text{air to film} \qquad r_1 = \frac{n_o - n_1}{n_o + n_1} \quad \text{air to film}$$

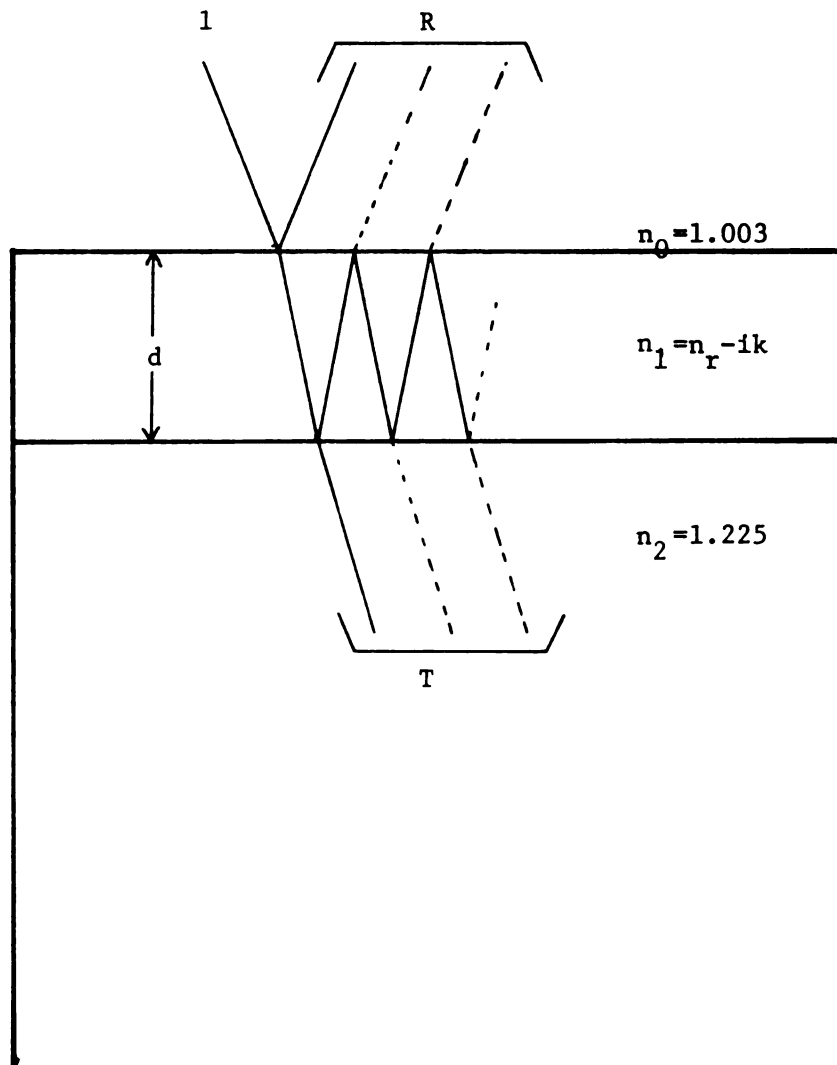


Figure C 1  $\alpha$  measurement sample.

$$\begin{aligned}
 t_1' &= \frac{2n_1}{n_0 - n_1} \quad \text{film to air} & r_2 &= \frac{n_1 - n_2}{n_1 + n_2} \quad \text{film to substrate} \\
 t_2 &= \frac{2n_1}{n_1 + n_2} \quad \text{film to substrate} & n_0 &= 1.003 \\
 & & n_2 &= 1.225 \quad \alpha = \frac{4\pi k}{\lambda} \\
 & & n_1 &= n_r - ik \\
 & & & \delta = \frac{2\pi}{\lambda} n_1 d
 \end{aligned}$$

$n_r$  and  $k$  are the real and imaginary parts of the amorphous silicon refractive index.

The reflectance and transmittance, the ratios of reflected and transmitted intensity to incident intensity, are then given by

$$\begin{aligned}
 R &= R_E R_E^* \\
 T &= \frac{n_2}{n_0} T_E T_E^*.
 \end{aligned}$$

$R$  and  $T$  are the measured quantities. For sufficiently absorbing films  $R_E$  and  $T_E$  may be approximated as follows since very little light will pass through the film twice and contribute to interference terms.

$$\begin{aligned}
 R_E' &= r_1 & , & & R &= r_1^2 \\
 T_E' &= t_1 t_2 e^{-\delta} & , & & T &= \frac{n_2}{n_0} |t_1 t_2|^2 e^{-\alpha d}
 \end{aligned}$$

The transmittance obtained using the expression for  $T_E$  differs from that derived from  $T_E'$  by the interference term.

$$\text{I.T.} = \left| \frac{1}{1+r_1 r_2 e^{-2i\delta}} \right|^2$$

which may be greater or less than one, depending on the phase shift  $\delta$ . For sample #48, which is typical in that the maximum transmittance (T) used in a quantitative way is 0.035, this interference term has a maximum value of 1.0073, a 0.73% correction. The correction in the optical absorption coefficient is only .28%. Assuming the worst case for the phase of  $\delta$ , that is using

$$\text{I.T.}_{\text{max}} = \left| \frac{1}{1+|r_1 r_2 e^{-2i\delta}|} \right|^2$$

for the interference term, the correction in  $\alpha$  is still only 0.63%, leading to the conclusion that  $T_E'$  is sufficiently accurate. The correction term for  $R_E'$  is of approximately the same magnitude since the transmission and reflection coefficients have magnitudes near unity and  $e^{-2i\delta}$  is again small.

For films in this research R depends strongly on the real part of  $n_1$  and weakly on the imaginary part of  $n_1$ . T depends strongly on the imaginary part of  $n_1$ . The index  $n_1$  (and thus the optical absorption coefficient  $\alpha$ ) is found by first estimating k, the complex part, then finding the real part  $n_r$ , consistent with the observed reflectivity. The imaginary part

is then computed more exactly using the observed value of  $T$ . When the values of  $T$  and  $R$  calculated using  $n_1 = n_r - ik$  match the observed  $T$  and  $R$  values,  $n_1$ , and consequently  $\alpha$ , has been determined.

Specifications for the grating used at these wavelengths indicate that about .1% scattered light may be expected. This seems insignificant until it is realized that at 487 nm only  $7 \times 10^{-4}\%$  of the light is transmitted. Since the scattered light occurs at all wavelengths, the longer wavelength portion of the scattered light will be passed by the silicon, interfering with measurement of the strongly absorbed light. In fact at 487 nm (blue) the transmitted light appears red to the eye. To minimize the spectral extent of scattered light a narrow bandwidth (40 nm) "Monopass" filter made by Optics Technology Inc. filtered the light entering the monochrometer, eliminating light at those wavelengths where the transmittance of the film is large. Since the amount of transmitted light at short wavelengths is so small, it is important to shield the measuring system from stray light, and especially important to ensure that no long wavelength light passes through the chopper to be detected by the phase locked amplifier. The measurements were made in a darkened room with the light path shielded.

In this measurement, as in the index measurement,

the monochromator supplies a finite bandwidth of light. Since a high incident intensity is needed at the short wave lengths to allow detection of the transmitted light, fairly wide entrance and exit slits are employed. The slit-grating combination used passes a band of wavelengths 38.4 nm wide, centered about the set wavelength. The transmittance  $T(\lambda)$  of the film varies rapidly at the short wavelengths, causing the center wavelength of the transmitted light to be shifted somewhat. This is shown in Figure C2. The shape of the resultant transmission-detection function  $O(\lambda)$  depends on the details of the transmittance of the film and the monopass filter, as well as on the spectral shape of the incident light intensity and sensitivity function of the silicon cell.

From the known transmittance of the filter and the characteristics of the measuring system, one may show that this effect causes the transmission of the film to be overestimated. The magnitude of the error be found for a typical film as shown in Figure C3.

From these considerations the measured transmittance is predicted to be about 9% larger than it would be for a perfectly monochromatic beam at the set wavelength for the measurement at 512 nm. Alternatively the difference in  $T$  may be attributed to a wavelength shift since  $T$  changes rapidly with wavelength.

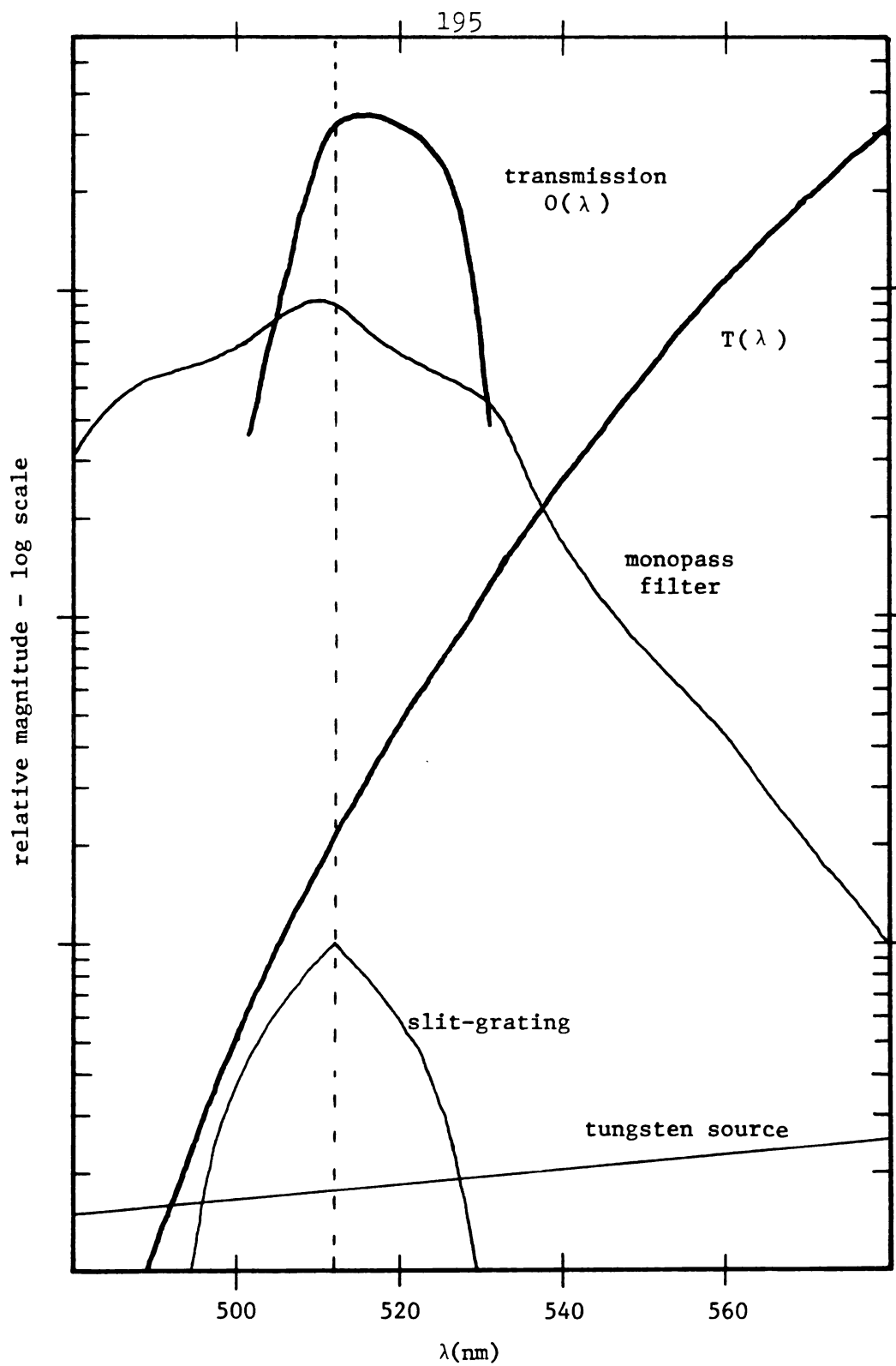
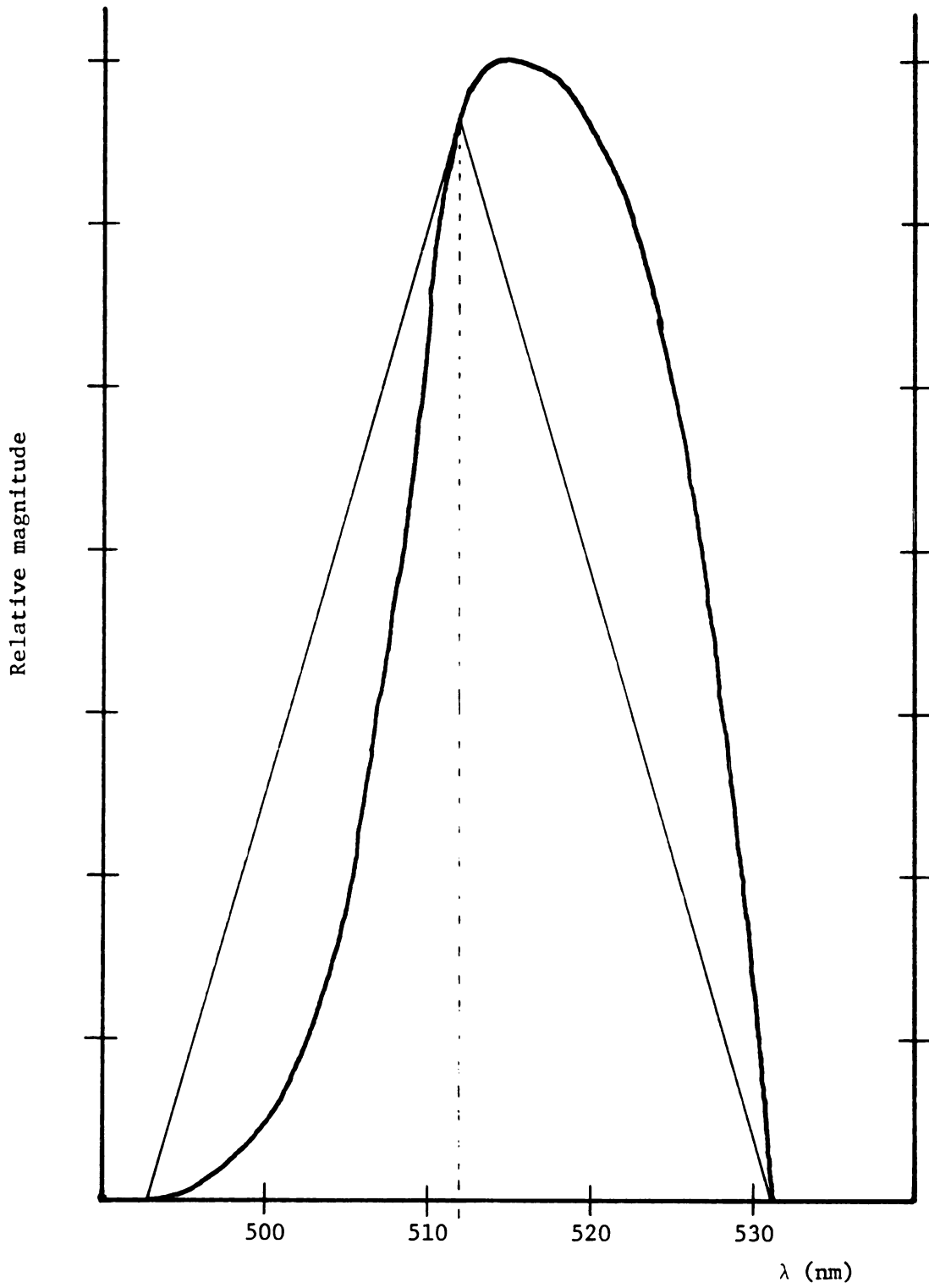


Figure C 2 Functions for computing error in  $\alpha$  .

Figure C 3 Real and simple  $O(\lambda)$ .

The wavelength shift turns out to be only about  $\ln m$ , which is less than the monochrometer's stated accuracy of  $\pm 2\text{nm}$ .

Since  $\alpha$  appears in the exponent, errors in  $T$  correspond to much smaller percentage errors in  $\alpha$ , especially for the larger values of  $\alpha$ . For example, the 9% transmittance error just described results in a 1.1% underestimation of  $\alpha$ .

Approximating  $\alpha$  by

$$T = (1-R)e^{-\alpha d} \quad \text{eq A1}$$

ignores the reflections at the film substrate interface and the internal reflection at the substrate air interface resulting in a 9% overestimation in  $\alpha$  for the most sensitive case (smallest  $\alpha$ ). The substrate-air reflection alone accounts for an error in  $T$  of about 3% or an overestimation of  $\alpha$  by 1.1% in the most sensitive case.

By replacing eq A1 by a more exact relationship  $\alpha$  may be found to approximately a  $\pm 7\%$  accuracy. Four percent of this is due to the uncertainty in thickness, 2% to the wavelength accuracy of the monochrometer and 1% to measurement error in  $R$  and  $T$ .

Since  $\alpha$  is used only for computation of the optical gap in this research, and the optical gap computed using equation A1 for  $\alpha$  differs from that computed

by the more exact theory by approximately 1%, the simpler approximation is used throughout.

## APPENDIX D

## GOLD TRANSMISSION MEASUREMENTS

Again, as in Appendix C, the transmission of light by a thin film is desired. In this case the film is a very thin layer of gold ( $\sim 250\text{\AA}$ ) deposited on either a transparent substrate (glass) or an absorbing one (amorphous silicon). The equations describing the transmittance of light are again from Heavens.<sup>63</sup> The reflected and transmitted field amplitudes are given by

$$R_E = r_1 + \frac{t_1 t_1' r_2 e^{-2i\delta}}{1 + r_1 r_2 e^{-2i\delta}}$$

$$T_E = \frac{t_1 t_2 e^{-i\delta}}{1 + r_1 r_2 e^{-2i\delta}}$$

$t_1 = \frac{2n_0}{n_0 + n_1}$	air to film	$r_1 = \frac{n_0 - n_1}{n_0 + n_1}$	air to film
$t_1' = \frac{2n_1}{n_0 + n_1}$	film to air	$r_2 = \frac{n_1 - n_2}{n_1 + n_2}$	film to substrate
$t_2 = \frac{2n_1}{n_1 + n_2}$	film to substrate	$n_0 = 1.00$	air
		$n_1 = .65 - i2.8$	gold
		$n_2 = 1.53$	glass

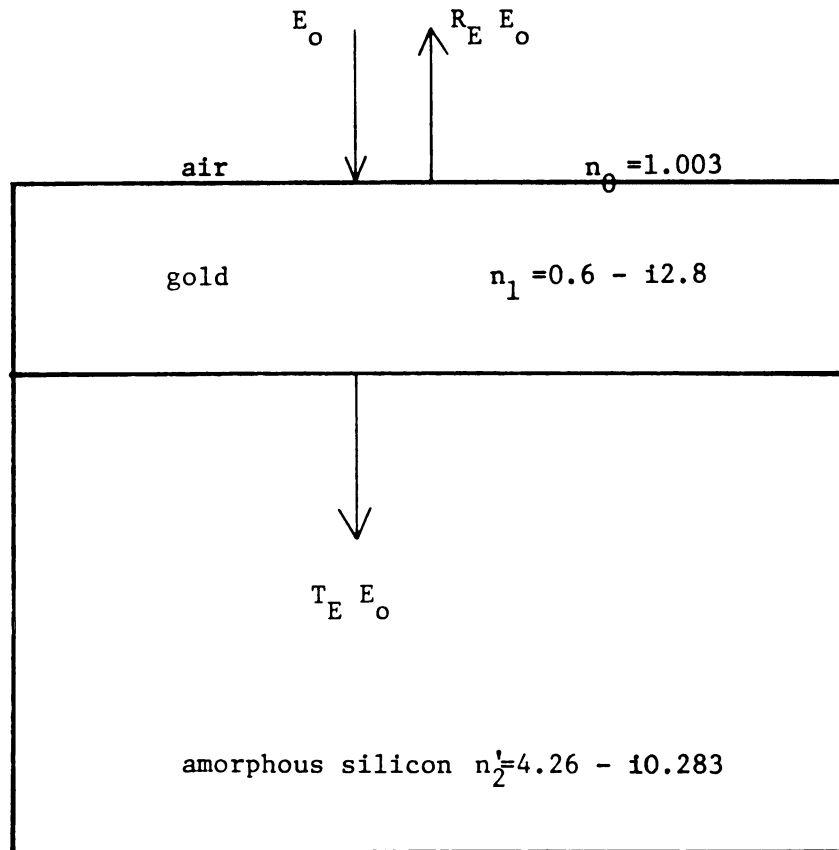


Figure D 1 Gold transmission schematic.

$$n_2' = 4.261 - i.283 \text{ amorphous silicon}$$

The index of gold is from Heavens<sup>63</sup> and that of amorphous silicon has been determined for the films in this research as described in Appendix C, both for  $\lambda = 550\text{nm}$ . The reflectance, R, and transmittance T are given by

$$R = R_E R_E^*$$

$$T = \frac{\text{Re}(n_2)}{n_0} T_E T_E^*, \text{ where } \text{Re}(n_2) \text{ denotes the real}$$

part of  $n_2$ . R and T for glass and amorphous silicon substrates are plotted in Figure D2. This model predicts fairly accurately the difference in reflectance of gold films deposited on glass and amorphous silicon as well as the transmittance of the gold films on glass given their reflectance.

The information contained in Figure D2 is used in 2 ways. When the transmittance of a particular gold film on glass is known, its transmittance on amorphous silicon may be accurately predicted; the difference is on the order of 10-20%. If only the reflectance of the gold film as deposited on the silicon is known, the plot may be used to find the thickness, and from the thickness the transmittance may be found. The accuracy of this second method is probably somewhat lower since the transmittance prediction relies heavily

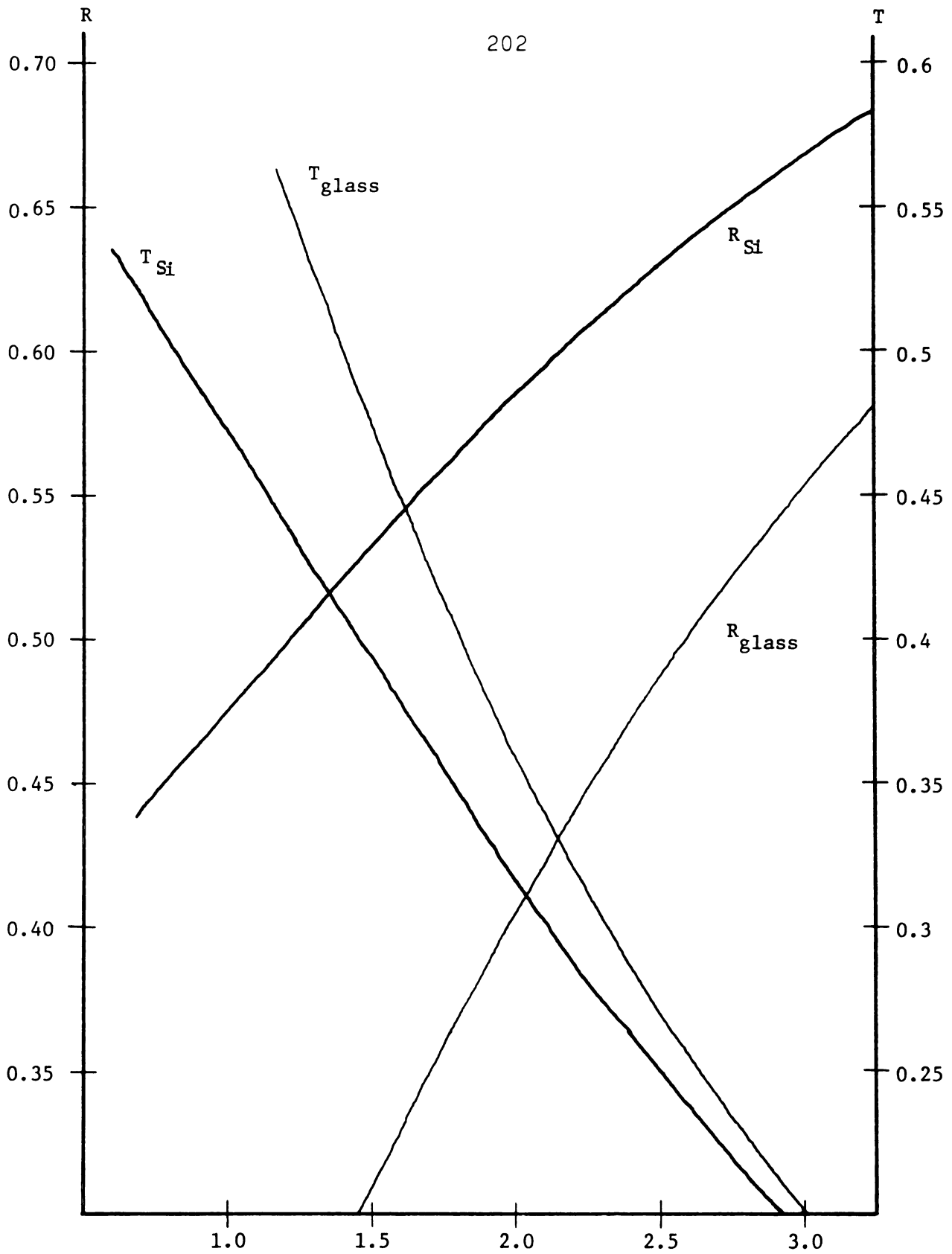


Figure D 2 Gold reflectance and transmittance.

on the theory accurately predicting the real results  
and the procedure is somewhat indirect.

LIST OF REFERENCES

## LIST OF REFERENCES

1. D. E. Carlson, IEEE Spectrum, 17, 291 (1980)
2. K. Kuwano, T. Imai, M. Ohnishi and S. Nakano, 14th IEEE Photovoltaic Specialists Conference, 800 (1980)
3. J. G. Posa, Electronics, July 3, (1980)
4. R. A. Gibson, P. G. Lecomber and W. E. Spear, Appl. Phys. Lett., 36, 66 (1980)
5. D. H. Auston, D. Lavallard, N. Sol and D. Kaplan, Appl. Phys. Lett., 36, 66 (1980)
6. J. Yomoto, H. Yajima, Y. Sehi and J. Shimada, Appl. Phys. Lett., 40, 632 (1982)
7. R. H. Lemons, Appl. Phys. Lett., 36, 919 (1980)
8. I. Shimizu, S. Oda, K. Saito and E. Inoue, J. Appl. Phys., 51, 6422 (1980)
9. A. Catalano, R. D'Aello, J. Dresner, B. Faughnan, A. Firester, J. Kane, H. Schade, Z. Smith, G. Swartz, A. Triano, 16th IEEE Photovoltaic Specialists Conference, 1421 (1982)
10. Electronic Newsletter, Electronics, May 5, 34 (1982)
11. Y. Tawada, M. Kondo, H. Akamoto and Y. Hamahawa, IEEE Spectrum, 245 (1981)
12. T. D. Moustakas, J. of Electronic Materials, 8, 391 (1979)
13. W. Paul and D. A. Anderson, Solar Energy Materials, 5, 229 (1981)
14. W. E. Spear, P. G. Lecomber, Solid State Comm., 17, 1193 (1975)
15. R. C. Chittick, J. H. Alexander, H. F. Sterling, J. Electrochem. Soc., 116, 77 (1969)
16. W. E. Spear, P. G. Lecomber, Phil. Mag., 33, 935 (1976)

17. W. E. Spear, P. G. Lecomber, 7th Inter. Conf. on Amorphous and Liquid Semiconductors, ed. by W. E. Spear, 309 (1977)
18. R. A. Gibson, W. E. Spear, P. G. Lecomber and A. J. Snell, J. Non Cryst. Solids, 35 & 36, 725 (1980)
19. D. E. Carlson, J. Non Cryst. Solids, 35 & 36, 707 (1980)
20. W. Paul, A. J. Lewis, G. A. N. Connell and T. D. Moustakas, Solid State Comm., 20, 969 (1976)
21. M. H. Brodsky, J. Vac. Sci. and Tech., 8, 125 (1971)
22. G. A. N. Connell and J. R. Pawlik, Phys. Rev. B., 13, 787 (1976)
23. W. Paul and D. A. Anderson, Solar Energy Materials, 5, 299 (1981)
24. N. F. Mott and E. A. Davis, Electronic Processes Non-Crystalline Materials, 362-375, Oxford University Press, 1979
25. N. B. Goodman and H. Fritzsche, Phil. Mag. B, 42, 149 (1980)
26. G. H. Dohler, M. Hirose, 7th Inter. Conf. on Amorphous and Liquid Semiconductors, ed. by W. E. Spear, 372 (1977)
27. D. V. Lang, J. D. Harbison, Phys. Rev. B, 25, 5285 (1982)
28. K. D. Makenzie, P. G. Lecomber and W. E. Spear, Phil Mag. B, 46, 377 (1982)
29. P. D. Persans, Phil. Mag. B, 46, 435 (1982)
30. H. Oheda, S. Yamaski, T. Yoshida, A. Matsuda, H. Okuski and K. Tanaka, J. J. Appl. Phys., 29, L440 (1982)
31. J. C. Anderson, Phil. Mag. B, 46, 151 (1982)
32. B. A. Scott, M. H. Brodsky, D. C. Green, R. M. Plecenik, E. E. Simonri and R. Serino, AIP Conference Proceedings No. 73, 6 (1981)

33. P. M. Martin and W. T. Palewicz, AIP Conf. Proc. No. 73, 52 (1981)
34. P. Hey, N. Raouf, D. C. Booth and B. O. Serephin, AIP Conference Proc. No. 73, 58 (1981)
35. S. C. Gar, B. R. Weinberger, M. Akhtar, Z. Kiss and A. G. MacDiarmid, AIP Conf. Proc. No. 73, 63 (1981)
36. N. Szydlo, D. Kaplan and R. Poirier, Third E. C. Photovoltaic Solar Energy Conference, 317 (1980)
37. A. K. Malhotra, G. W. Neudeck, Appl. Phys. Lett., 28, 47 (1976)
38. T. D. Moustakas and R. Friedman, Appl. Phys. Lett., 40, 515 (1982)
39. N. Szydlo, E. Chartier, N. Proust, J. Magarino and D. Kaplan, Appl. Phys. Lett., 40, 988 (1982)
40. G. Muller, S. Kalbitzer, W. E. Spear, P. G. Lecomber, 7th Inter. Conf. On Amorphous and Liquid Semiconductors, Ed. by W. E. Spear, 442 (1977)
41. M. G. Thompson and D. K. Reinhard, 14th IEEE Photovoltaic Specialists Conference, 1218 (1980)
42. A. Madan and S. R. Ovshinsky, J. of N. Cryst. Solids, 35 & 36, 171 (1980)
43. A. Madan, W. Czubytyj, D. Adler and M. Silver, Phil. Mag. B, 42, 257 (1980)
44. A. Madan, J. McGill, W. Czubytyj, J. Yang and S. R. Ovshinsky, Appl. Phys. Lett., 37, 826 (1980)
45. B. Chapman, Glow Discharge Processes, 205-231, John Wiley & Sons (1980)
46. G. Moddel, J. Blake, R. W. Collins, P. Viktorovitch, D. K. Paul, B von Raedern and W. Paul, AIP Conf. Proc. No. 73, 25 (1981)
47. D. A. Anderson, G. Moddel, R. W. Collins and W. Paul, Solid State Comm. 31, 677 (1979)
48. D. A. Anderson, W. Paul, Phil. Mag. B, 44, 187 (1982)

49. T. D. Moustakas and T. Tiedje, American Inst. of Physics Conf. No. 73, 20 (1981)
50. L. I. Maissel and R. Glang, Handbook of Thin Film Technology, Chapters 3 & 4, McGraw-Hill, Inc. 1970
51. B. Chapman, Glow Discharge Processes, Chapter 1, John Wiley & Sons (1980)
52. D. E. Carlson and C. R. Wronski, J. of Electronic Mat., 6, 95 (1977)
53. L. Vieux-Rochaz and A. Chenevas-Paule, J. of Non Cryst. Solids, 35 & 36, 737 (1980)
54. C. C. Tsai, R. J. Nemanick and M. J. Thompson, J. Vac. Sci Technol., 21, 632 (1982)
55. M. J. Thompson, N. M. Johnson, R. J. Nemanick and C. C. Tsai, Appl. Phys. Lett., 39, 274 (1981)
56. J. D. Cohen and D. V. Lang, Phys. Rev. B, 25, 5321 (1982)
57. J. Beizhler, W. Fuhg, H. Mell and H. M. Welsch J. Non Cryst. Solids, 35 & 36, 587 (1980)
58. A. R. Moore, J. Appl. Phys., 54, 222 (1983)
59. A. Madan, W. Czubytyj and J. Yang, Appl. Phys. Lett., 40, 234 (1982)
60. T. D. Moustakas, R. Friedman and B. R. Weinberger, Appl. Phys. Lett., 40, 587 (1982)
61. J. L. Vossen, J. Vac. Sci. and Tech., 8, 512 (1971)
62. O. Christensen, P. Jensen, J. Physics E., 5, 86 (1972)
63. O. S. Heavens, Optical Properties of Thin Solid Films, Chapters 5 & 6, Academic Press, Inc., 1955
64. J. P. deNuefville, T. D. Moustakas, A. F. Ruppert, J. Non Cryst. Solids, 35 & 36, 481 (1980)
65. N. F. Mott and E. A. Davis, Electronic Processes in Non-Crystalline Materials, 272-300, Oxford University Press (1979)

66. M. G. Thompson, Ph.D. Thesis, Michigan State University (1980)
67. R. A. Smith, Semiconductors, 201-210, Cambridge University Press (1959)
68. R. C. Ross, I. S. T. Tsong, R. Messier, W. A. Lanford and C. Buman, J. Vac. Sci. Tech. 20, 406 (1982)
69. M. H. Brodsky, M. A. Frisch, J. F. Ziegler, and W. A. Lanford, Appl. Phys. Lett., 30, 561 (1977)
70. F. R. Jeffrey, H. R. Shanhsand, G. C. Danielson, J. Non-Cryst. Solids, 35 & 36, 261 (1980)
71. I. Chen and J. Mort, Appl. Phys. Lett., 37, 952 (1980)
72. J. Mort, A. Troup, M. Morgan, J. Knights, R. Lujan and S. Grammatica, Appl. Phys. Lett., 38, 277 (1981)
73. D. L. Staebler, J of Non-Cryst. Solids, 35 & 36, 387 (1980)
74. A. R. Moore, J. Appl. Phys., 54, 222 (1983)
75. N. F. Mott and E. A. Davis, Electronic Processes in Non-Crystalline Materials, Chapter 2, Oxford University Press (1979)
76. M. Tanielian, Phil. Mag. B. 45, 435 (1982)
77. D. L. Staebler and C. R. Wronski, Appl. Phys. Lett., 31, 292 (1977)
78. D. A. Anderson and W. E. Spear, Phil. Mag., 36, 695 (1977)
79. S. Ovshinsky and A. Madan, Nature, 276, 482 (1978)
80. J. Baixeras, D. Mencaraglia and P. Andro., Phil. Mag. B, 37, 403 (1978)
81. B. Chapman, Glow Discharge Processes, 181-195, John Wiley & Sons (1980)
82. T. Moustakas and T. Tiedje, AIP Conference Proceedings No. 73, 20 (1981)
83. P. Vanier, Appl. Phys. Lett., 41, 986 (1982)

84. R. Street, *App. Phys. Lett.*, 42, 507 (1983)
85. T. Moustakas, C. Wronski and T. Tiedje, *Appl. Phys. Lett.*, 39, 721 (1981)
86. H. Overhoff, *Phil. Mag.*, 44, 317 (1981)
87. P. Viktorovitch, G. Moddel and W. Paul, *AIP Conference Proceedings No. 73*, 186 (1981)
88. H. Fritzsche and M. Tanielian, *AIP Conference Proceedings No. 73*, 318 (1981)
89. M. Suzuki, T. Maekawa, S. Okano and T. Bandow, *J. J. Appl. Phys.*, 20, L485 (1981)
90. P. Martin and W. Pawlewicz, *J. Non-Cryst. Solids*, 45, 15 (1981)
91. D. Turner, I. Thomas, J. Allison, M. Thompson, A. Rhodes, I. Austin and T. Searle, *AIP Conference Proceedings No. 73*, 47 (1981)
92. J. Allison, M. Thompson, D. Turner and I. Thomas, *Third E. C. Photovoltaic Solar Energy Conference*, 820 (1980)
93. R. Ross and R. Messier, *AIP Conference Proceedings No. 73*, 53 (1981)
94. P. Martin and W. Pawlewicz, *AIP Conference Proceedings No. 73*, 52 (1981)
95. A. Jonath, J. Thornton, W. Anderson, J. Crowley, H. MacMillan and G. McCauly, *Third E. C. Photovoltaic Solar Energy Conference*, 840 (1980)
96. S. Ashok, A. Lester and S. Fonash, *IEEE Electron Device Letters*, EDL-1, 200 (1980)
97. A. Bagget and P. Viktorovitch, *Phys. State Sol. (a)*, 56, 495 (1979)
98. Xu Le, D. K. Reinhard and M. G. Thompson, *IEEE Trans. Electron Devices*, ED-29, 1004 (1982)
99. C. Wronski, D. Carlson and R. Daniel, *Appl. Phys. Lett.*, 29, 602 (1976)
100. E. Rhoderick, *Metal-Semiconductor Contacts*, Oxford University Press (1978)

101. M. Silver, N. Giles and E. Snow, *App. Phys. Lett.*, 41, 935 (1982)
102. W. Spear, D. Allan, P. LeComber and A. Gaith, *Phil. Mag. B.*, 41, 419 (1980)
103. S. M. Sze, Physics of Semiconductor Devices, Chapter 5, John Wiley & Sons (1981)
104. H. Hovel, Semiconductors and Semimetals, Volume 11, Academic Press (1975)
105. M. K. Han, W. Anderson, Y. Onuma, P. Sung, R. Lahri and J. Coleman, *IEEE Electron Device Letters*, EDL-2 (1981)
106. D. Jousse, P. Viktorovitch, L. Vieux-Rochaz and A. Chenevas-Paule, *J. Non-Cryst. Solids*, 35 & 36, 767 (1980)
107. M. J. Thompson, J. Allison, M. Al-Karsi and I. Thomas, *Revue de Physique Appl.*, 13, 625 (1978)